

# **MAGNETOELECTRIC DEVICE AND THE MEASUREMENT UNIT**

**Zengping Xing**

Dissertation submitted to the faculty of the  
Virginia Polytechnic Institute and State University  
in partial fulfillment of the requirement for the degree of  
Doctor of Philosophy  
in  
Materials Science and Engineering

Dwight D. Viehland, Advisor, Chair  
Willem G. Odendaal, Co-Advisor  
Jie-Fang Li  
Yu Wang

April 10 2009

Blacksburg, Virginia

Keywords: Magnetolectric, Sensors, Actuators, Modeling  
Optimization, Noise Spectrum, Low noise circuitry, Spice Simulation

**©Copyright 2009, Zengping Xing**

# **MAGNETOELECTRIC DEVICE AND THE MEASUREMENT UNIT**

Zengping Xing

## **Abstract**

Magnetic sensors are widely used in the field of mineral, navigational, automotive, medical, industrial, military, and consumer electronics. Many magnetic sensors have been developed that are generated by specific laws or phenomena: such as search-coil, fluxgate, Hall Effect, anisotropic magnetoresistance (AMR), giant magnetoresistance (GMR), magnetoelectric (ME), magnetodiode, magnetotransistor, fiber-optic, optical pump, superconducting quantum interference device (SQUID), etc. Each of these magnetic field sensors has their merits and application areas. For low power consumption ( $<10\mu\text{W}$ ), quasi-static frequency ( $<10\text{Hz}$ ) and high sensitivity ( $<n\text{T}$ ) application, magnetoelectric laminate sensors offer the best potential capability and thus are the topic of my dissertation.

Here, in this thesis, I have focused on designs and optimizations of magnetoelectric sensor units (i.e., sensors and circuit). To achieve my goals, I have developed some useful rules for ME sensor and detection circuit design.

For ME sensor optimization, designs should consider both frequencies far away from resonance and at resonance. For the former one, both internal and external noise

contribution must be considered, as one of them will limit practical applications. With regards to the internal noise sources, I have developed two design optimization methods, designated as “scale effect” and “ME array”. I showed that they have the ability to increase the magnetic field detection sensitivity, which was verified by experiments. With regard to external noise consideration, I have investigated how the fundamental extrinsic noise sources (temperature fluctuation, vibration, etc) affect ME laminate sensors. A concept of separating signal and noise modes into difference is put forward. Optimization with this concept in mind required us to redesign the internal structure of ME laminate sensors. At the resonant frequency, the ME voltage coefficient  $\alpha_{ME}$  is the most important parameter. To enhance resonant gain in  $\alpha_{ME}$ , I have developed a three phase laminate concept, which is based on increasing the effective mechanical factor Q while reducing the resonant frequency. A ME voltage coefficient of  $\alpha_{ME} \sim 40V/cm.Oe$  has been achieved at resonance, which is about 2× higher than that of a conventional bending mode.

Investigations of detection circuit optimization were also performed. Component selection strategies and a new charge topology were considered. Proper component values were required to optimize the charge detection scheme. It was also found, under some specific conditions to satisfy the circuit stability, that if the lowest required measurement frequency of the charge source was  $f_1$ , then that it was not necessary to make the high corner frequency ( $f_p$ ) of the charge amplifier lower than  $f_1$ : as doing so would decrease the system’s signal-to-noise ratio (SNR). A high pass, high order filter placed behind the charge amplifier was found to increase the charge

sensitivity, as it narrows the intrinsic noise bandwidth and decreases the output noise contribution, while only slightly affecting the signal's output amplitude.

Prototype ME unit were also constructed, and their noise level simulated by Pspice. Experimental results showed that prototypes ME unit can reach their detection limit. In addition, a new magneto-electric coupling mechanism was also found, which had a giant ME effect.

*To my family*

## Acknowledgements

I would like to express my sincere gratitude to my advisor Prof. Dwight Viehland for giving me this opportunity to work on this challenging and exciting project and for his faith, guidance and support throughout the course of my Ph.D study and research. The same gratitude goes to Prof. Willem G. Odendaal in Center for Power Electronics Systems (CPES, ECE), who served as my co-advisor during the time.

I have tremendous respect to Prof. Dwight Viehland for his knowledge, wisdom and passion for research. I benefit a lot from his guidance during my Ph.D study including his “Structure Properties Materials” class, the discussion we held, the intelligent suggestions he made on my research, his patience on correcting my papers, and his helpful instruction on my presentations and seminars. His high enthusiasms on research affect me much and will be very helpful in my future career. He believes we can do it and we just do it. I deeply appreciate all his invaluable help and affection.

Also, I would like to express my gratitude to my co-advisor Prof. Williem G. Odendaal, he gave me lot of guidance and helps in practical low noise electronic system design, his sparking idea and profound knowledge make the tough thing go easier, I benefit a lot from many of our meeting and discussion.

Equally important, Prof. Jiefang Li has given me great help and guidance in almost all the equipments’ and facilities’ set up. She generously shared with me all her senior experience in experimental techniques. I would not success in many of my research areas without her help.

I would also like to thank Prof. Yu Wang; I learned from him many useful theories and analysis methods in materials science. I always acquired new knowledge each time I discussed with him. His strong theory convinced me in many ideas.

I would like thank my cooperators, Dr. Junyi Zhai, we shared a lot of good ideas in this project and I learned a lot from him in the ME measurement. We cooperated together happily and made many research things go much easier.

I would like to thank Prof. Shuxiang Dong, He shared with me many of his smart

device design ideas and testing methods. I benefit a lot from the discussion and experiments we did together.

I would like to thank David berry for the help on the experiment equipments and many insightful discussion in experiments.

I would like to thank Prof. Chris Fuller (ME). I learned from him many useful analysis methods for sensors and actuators.

Prof. Inman and his students (ME): Steve Anton and Pablo Tarazaga helped me much on the vibration testing experiments; special thanks must be given to them.

I would like to thank Prof. Ali H. Nayfeh and his student Giancarlo Giuseppe Bordonaro (ESM), they helped me much on the FFT spectrum analysis experiments.

I would also like to thank Yan Li, Feiming Bai, Hu Cao, Naigang Wang, Yaodong Yang, Chris DeVreugd, Junqi Gao, Zhiguang Wang, Wenwei Ge, Liang luo and Jianjun Yao, who are the members in Prof. Dwight Viehland's group. It will always be a good memory to work with them.

Finally, but the most important acknowledgement, to my parent: Kongxiang Xing and Dao'ai Cai, for their wholehearted love, unconditional support, understanding, patience and encouragement when I am sad and depressed, your son will never disappoint you.

# Table of contents

<b>ABSTRACT.....</b>	<b>ii</b>
<b>DEDICATION.....</b>	<b>v</b>
<b>ACKNOWLEDGEMENTS.....</b>	<b>vi</b>
<b>TABLE OF CONTENTS.....</b>	<b>viii</b>
<b>LIST OF TABLES.....</b>	<b>x</b>
<b>LIST OF FIGURES.....</b>	<b>xi</b>
<b>1. INTRODUCTION.....</b>	<b>1</b>
1.1 Development of magnetoelectric materials.....	1
1.1.1 Magnetoelectric effect and magnetoelectric materials.....	1
1.1.2 Different mode ME laminates.....	7
1.2 The potential of ME laminates as magnetic field sensors.....	15
1.3 Noise sources and their mitigation.....	17
1.3.1 External noise.....	19
1.3.2 Internal noise.....	28
<b>2. PURPOSE OF THIS THESIS.....</b>	<b>33</b>
<b>3. MODELING OF THE ME LAMINATES.....</b>	<b>37</b>
3.1 Introduction.....	37
3.2 Modeling of ME laminates at low frequencies.....	39
3.3 Summary.....	53
<b>4. ME LAMINATES DESIGN OPTIMIZATION.....</b>	<b>54</b>
4.1 Introduction.....	54
4.2 ME sensitivity optimization on considering internal noise.....	59
4.2.1 ME sensitivity and the scale effect.....	59
4.2.2 ME array to enhance sensitivity.....	66
4.3 ME sensitivity optimization on considering external noise.....	79
4.3.1 External noise on ME sensors.....	82
4.3.2 Analysis of external noise in different modes of ME laminates.....	85
4.3.3 Investigations of vibrational noise rejection.....	98

4.4 Low resonant frequency Giant ME effect.....	102
4.5 Discussion and Summary.....	112
<b>5. ME DETECTION CIRCUIT OPTIMIZATION.....</b>	<b>115</b>
5.1 Introduction.....	115
5.2 SNR on feedback components.....	117
5.2.1 Charge scheme and SNR calculation.....	117
5.2.2 Special case considerations.....	120
5.2.3 Spice simulation result.....	122
5.3 New charge topology for SNR improvement.....	123
5.3.1 High SNR charge measurement topology: Theory.....	123
5.3.2 Spice Simulation.....	131
5.4 Summary.....	135
<b>6. ME UNIT SIMULATION.....</b>	<b>139</b>
6.1 Conclusion.....	139
6.2 ME sensor Simulation in Time domain.....	140
6.3 ME Unit noise level simulation.....	142
<b>7. GIANT MAGNETOELECTRIC MECHANISM IN MAGNET/PIEZOELECTRIC DEVICE.....</b>	<b>148</b>
7.1 Conclusion.....	148
7.2 Working principle and Experiment.....	149
7.4 Summary.....	154
<b>REFERENCE.....</b>	<b>155</b>

## LIST OF TABLES

Table I-I Different modes ME laminate.....	9
Table I-II Various magnetic sensor technologies.....	18
Table IV-I ME laminate sensors.....	64
Table IV-II ME laminate sensors.....	83
Table IV-III ME laminate sensors.....	101
Table IV-IV Typical material parameters for the laminate layers.....	108
Table V-I Impedance and noise features of the sensor for simulation.....	124
Table V-II Properties of the source sensor for simulation.....	132

## LIST OF FIGURES

Fig.1-1. Schematic representation of the particulate Terfenol-D/PZT/polymer composites.....	3
Fig.1-2. Disc ME laminate constructed by Terfenol-D and PZT.....	6
Fig.1-3. Fundamental ME structure.....	10
Fig.1-4. ME voltage coefficient DC bias dependence for L-mode and T-mode.....	11
Fig.1-5. Structure of (a) L-L push-pull and (b) Multi push-pull.....	13
Fig.1-6. Structure of (a) unimorph and (b) Bimorph.....	14
Fig.1-7. ME laminate works in ring mode and the equivalent circuitry.....	16
Fig.1-8. Direct coupling by common ground impedance.....	20
Fig.1-9. Electric circuit analysis for (a) electric coupling and (b)magnetic coupling.....	22
Fig.1-10. Triboelectric effect in coaxial cable.....	24
Fig.1-11. Triboelectric effect in coaxial cable.....	25
Fig.1-12. Electrochemical effect on sensor.....	27
Fig.1-13. (a) Thevenin noise model of resistor. (b) Norton noise model of resistor.....	30
Fig.3-1. Fundamental ME equivalent model.....	41
Fig.3-2. ME laminate signal model.....	43
Fig.3-3. (a)An equivalent circuitry for ME laminate with direct measurement method; (b)voltage as a function of frequency in ME direct measurement, illustrating a cut-off frequency below which shows significant roll-off occurs with decreasing frequency.....	44
Fig.3-4. ME laminate model with noise consideration.....	46
Fig.3-5. The magnetoelectric charge coefficient as a function of frequency, which shows a near constant value at low frequencies.....	48
Fig.3-6. ME laminate with noise spectra and current amplifier.....	49
Fig.3-7. Linearity of the ME sensor system at 1Hz, 10Hz and 100Hz.....	51
Fig.3-8. SNR and lowest detective signal for LT ME laminate.....	52
Fig.4-1. (a) Longitudinal and Transverse ME voltage coefficient on volume fraction $v$ for a	

perfectly bonded ( $k=1$ ) two-layer structure consisting of CFO and BTO; (b) Longitudinal ME voltage coefficient on interface coupling  $k$  and volume fraction  $v$  for the CFO-PZT bilayer; Calculation values of ME voltage response on thickness ratio  $n$  for (c) Terfenol-D/PZT-8 laminate; and (d) Terfenol-D/PZT-5 laminate.....56

Fig.4-2. Equivalent circuit model for low frequency ME laminate sensor, including noise spectra considerations.....62

Fig.4-3. (a) Dependence of the output noise level ( $E_{no}$ ) on sensor capacitance ( $C$ ) for the various laminate composites given in Table IV-I; and (b) The signal-to-noise ratio (SNR) on , where  $V$  is the volume of the piezoelectric phase and  $\alpha_{ME}$  is the magnetoelectric voltage coefficient; Each point corresponds to one of the ME laminate sensors enumerated in Table IV-I.....65

Fig.4-4. (a) Waveforms in real time of the output noise level ( $E_{no}$ ) of a small LT mode ME laminate (sensor No.2 in Table IV-I) and of a large one (sensor No.5); and (b) The lowest magnetic field ( $f=1\text{Hz}$ ) detectable with a 95% confidence level. The small ME sensor had a sensitivity limit of  $\sim 3\text{nT}$ , whereas the large ME sensor of  $\sim 1\text{nT}$ .....67

Fig.4-5. The lowest magnetic field signal ( $f=1\text{Hz}$ ) detectable with a 95% confidence level on  $\frac{1}{\sqrt{V}} \cdot \alpha_{ME}$  .....68

Fig.4-6. Equivalent circuit model for the ME laminate sensor, including noise spectra considerations: voltage source model.....69

Fig.4-7. (a) Equivalent circuit for the ME array in parallel model; and (b) the simplification.....71

Fig.4-8. (a) Equivalent circuit for the ME array in serial model; (b) simplification of (a); and (c) equivalent circuit of (b).....73

Fig.4-9. Prototype of the ME array and the low noise low power detection circuit.....75

Fig.4-10. Signal response, noise level and SNR for parallel mode ME array.....77

Fig.4-11. Signal response, noise level and SNR for serial mode ME array.....78

Fig.4-12. Waveforms in real time for a L-T ME unit corresponding to  $3\text{nT}$ , and L-T ME array corresponding to  $1\text{nT}$  sinusoid magnetic signal at  $1\text{Hz}$ .....80

Fig.4-13. Noise spectrum of the ME array in serial and parallel mode.....81

Fig.4-14. (a) A force free rectangular plate, and (b) influence of vibrations on the shape

deformation of the rectangular plate.....	84
Fig.4-15. External thermal noise on the plate in a (a) symmetrical structure; (b) unsymmetrical structure.....	86
Fig.4-16. Effect of vibrational and thermal noise on a unimorph.....	88
Fig.4-17. Effect of environmental noise on bimorph ME laminate (a) vibrational noise which excites bending mode; (b) thermal noise which excites a longitudinal mode; and (c) thermal noise which excites a bending mode.....	89
Fig.4-18. Effect of vibration bending noise on the PZT layer in (a) L-T, T-T modes ME laminate; and (b) L-L, T-L modes ME laminate.....	91
Fig.4-19. Vibration bending noise in (a) the L-L push-pull structure; (b) the L-T push-pull structure, where the inset shows the cancelation of vibration effects; (c) in a multi push-pull configuration, each individual push-pull unit works in the L-L mode.....	93
Fig.4-20. Bending on US-SN structure 1 (a); and noise analysis of piezoelectric layer for the structure 1: (b) vibration bending noise, and (c) thermal noise.....	96
Fig.4-21. Bending on US-SN structure 2 (a); and noise analysis of piezoelectric layer for the structure 2: (b) vibration bending noise, and (c) thermal noise.....	97
Fig.4-22. US-SN mode 3.....	99
Fig.4-23. vibrating damping experiment setup for ME laminate sensor.....	100
Fig.4-24. (a) Vibrating damping experimental result for different ME sensor; (b) ME voltage for different ME sensor.....	103
Fig.4-25. SNR for different ME sensor.....	104
Fig.4-26. Illustration of ME laminate configurations (a) Terfenol-D/Steel/PZT three-phase bending-mode unimorph; and (b) Terfenol-D/PZT unimorph.....	105
Fig.4-27. Illustration of the 1st bending-mode vibrations, calculated using FEA method.....	109
Fig.4-28. Magnetolectric voltage coefficient (VME) for both our Terfenol-D/Steel/PZT and Terfenol-D/PZT laminates: (a) as a function of DC magnetic bias taken at a measurement frequency of $f=100\text{Hz}$ ; and (b) as a function of frequency taken under a DC magnetic bias of $H_{dc}=300\text{Oe}$ .....	111
Fig.5-1. Fundamental topology for a charge amplifier.....	116

Fig.5-2. ME charge measurement scheme.....	118
Fig.5-3. Simulation as a function of feedback capacitance ( $10^{-12}<C_f<10^{-9}F$ ) at various frequencies for (a) output noise level $V_{no}$ , and (b) signal to noise ratio SNR. The simulations were performed using a fixed feedback resistance of $R_f=1G$ .....	125
Fig.5-4. Simulation as a function of feedback capacitance ( $10^{-12}<C_f<10^{-9}F$ ) for (a) output noise level $V_{no}$ , and (b) signal to noise ratio SNR. The simulations were performed using a fixed frequency of $f_p=f_1=10Hz$ .....	126
Fig.5-5. Simulation as a function of feedback resistance ( $10^8<R_f<10^{10}$ ) at various frequencies for (a) output noise level $V_{no}$ , and (b) signal to noise ratio SNR. The simulations were performed using a fixed feedback capacitance of $C_f=100pF$ .....	127
Fig.5-6. Transfer function of the (a) signal response $H_s(s)$ and (b) current noise gain $Z_n(s)$ .....	129
Fig.5-7. (a) The high SNR topology; (b) transfer function of the signal response $H_{s1}(s)$ ; and (c) transfer function of current noise gain of $Z_{n1}(s)$ .....	130
Fig.5-8. Source spectral current noise density.....	133
Fig.5-9. Charge amplifier with high pass filter simulation circuitry.....	134
Fig.5-10. (a) Signal response with and without the high pass filter; and (b) Output noise level with and without High pass (HP) filter.....	136
Fig.5-11. SNR comparison before and after add the HP filter.....	137
Fig.6-1. (a) Pspice model in time domain for the ME laminate sensor; and (b) The comparison of experimental results and simulation results (Top of each figures: the input, bottom of each figures: the corresponding output).....	141
Fig.6-2. The noise spectrum of the ME laminate sensor.....	143
Fig.6-3. Noise model of (a) the ME laminate sensor; and (b) ME unit.....	146
Fig.6-4. (a) Output noise simulation result of the ME Unit; (b) prototype of the ME unit; and (c) practical output noise measurement result of the ME prototype unit.....	147
Fig.7-1. (a) Structure of NdFeb/PZT-Bimorph/NdFeb; (b) photo of prototype device and testing.....	150
Fig.7-2. Illustration of the working principle.....	152
Fig.7-3. Frequency dependence of the ME voltage coefficient and charge coefficient.....	153

# CHAPTER 1

## INTRODUCTION

### 1.1 Development of magnetoelectric materials

#### 1.1.1 Magnetoelectric effect and magnetoelectric materials

The magnetoelectric (ME) effect is characterized by an induced dielectric polarization in response to an applied magnetic field (H), or by an induced magnetization in response to an applied electric field (E).<sup>1</sup> Magnetoelectric materials possess a coupling between dipole and spin, and exhibit the ME effect. The ME performance of a ME material can be evaluated by a parameter designated as the ME voltage coefficient  $\alpha_{ME}$ , which can be defined by the electric field  $\delta E$  induced by an applied magnetic field  $\delta H$  ( $\alpha_{ME} = \delta E / \delta H = \delta V / t \delta H$ , where  $t$  is the thickness); or conversely, the magnetic field induced by an applied electric one.<sup>2</sup>

The discovery of the ME effect can be traced back to a prediction based on crystal symmetry considerations by Curie in 1894.<sup>3</sup> However, many decades passed until it was realized that the ME effect can only appear in a time-asymmetric media.<sup>4</sup> Dzyaloshinskii was the first to suggest that the ME effect could appear in antiferromagnetic  $\text{Cr}_2\text{O}_3$ ,<sup>5</sup> which was soon followed by Astrov's experimental confirmation in 1960.<sup>6,7</sup> This was a milestone in the research of ME materials. Later, numerous single phase ME materials were reported.<sup>8-14</sup> These single phase materials have a linear ME effect, caused by a direct coupling between dipole and spin moments on the atomic scale. Unfortunately, the electronic configurations which

favor polarization are antagonistic to those that favor magnetization, and vice versa. This is simple to conceptualize: the  $d^5$  electronic configuration is favorable to spin alignment, but is not very distortable; whereas  $d^0$  is very distortable, but has no spin. The value of  $\alpha_{ME}$  for single phase materials has always been found to be very small, on the order of several mV/cm.Oe. This small ME effect makes it hard for them to be useful for devices.<sup>15</sup>

More recent investigations have reported improved multi-ferroic and ME properties in epitaxial layers of ME thin films such as  $\text{BiFeO}_3$  grown on  $\text{SrTiO}_3$ ,<sup>16</sup> and in self-assembled multiferroic nanostructures such as  $\text{CoFe}_2\text{O}_4$  nanopillars embedded in a  $\text{BaTiO}_3$  matrix on  $\text{SrTiO}_3$  substrates.<sup>17</sup> These are potentially useful for integrated microelectronic materials that have the promise of reading a spin state as a direct voltage. However, significant exchange between polarization and magnetization sublattices has not yet been reported in ME films. This may be due to the limited dielectric insulation, although it is not yet certain.

The “logical” thing to do when a materials property can not be obtained or optimized in a single phase system is to turn to a composite one! This has been done, or at least attempted, in the field of magnetoelectrics since early investigation at Philips research lab in Holland in the mid-1970’s.<sup>18</sup> This composite approach combines magnetostrictive and piezoelectric phases, which interact via elastic forces. Fig.1-1 illustrates one type of this composite:  $\text{Pb}(\text{Zr}_{1-x}\text{Ti}_x)\text{O}_3$  (PZT, piezoelectric phase) and the  $\text{Tb}_{1-x}\text{Dy}_x\text{Fe}_2$  (Terfenol-D, magnetostrictive phase) particles mixed together in a polymer matrix.<sup>19</sup> PZT has a giant piezoelectric effect. When a force is applied on it,

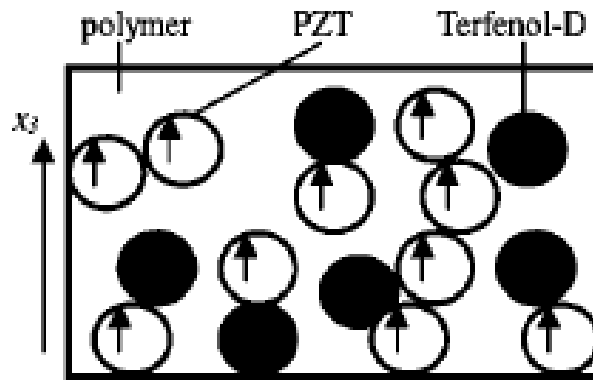


**Fig.1-1.** Schematic representation of the particulate Terfenol-D/PZT/polymer composites.<sup>19</sup>

Reprinted Fig.1-1 with permission from Ref [19] as follows: Zhan Shi, C.-W. Nan, J.M. Liu, D. A. Filippov and M. I. Bichurin, Phys. Rev. B, 70, 134417 (2004). Copyright (2004) by the American Physical Society.

a charge will be generated; or conversely, when we apply an electric field on it, an elastic deformation will occur. Terfenol-D is a giant magnetostrictive material, which changes shape under an ac magnetic field. However, to achieve an optimum performance, a preload mechanical force or a magnetic DC bias is required. In Fig.1-1; the Terfenol-D particles are illustrated to change their shapes under applied magnetic field, passing the elastic force through the polymer matrix to the PZT particles and inducing a charge. However, investigations performed between the mid-1970's and late 1990's revealed only modestly encouraging results, although theoretically the ME coefficient could be as high as  $\sim 100\text{mV/cm.Oe}$ .<sup>1</sup> There are several factors that have limited the progress: i) chemical reactions between the constituent phases or during sintering; ii) low resistivity of the magnetostrictive phase, which will make it difficult to pole the piezoelectric phase due to leakage currents; iii) mechanical defects that make stress transfer inefficient; iv) energy loss in the matrix; v) poor alignment of the piezoelectric dipoles in the poling process, which lowers the piezoelectric response; and vi) non-optimum alignment of the magnetization of the magnetostrictive phase on applying DC bias.<sup>20-26</sup> The magnetoelectric voltage coefficient of ME particle composite materials has been reported to be  $\sim 10\text{mV/cm.Oe}$ , which is much smaller than that predicted based on continuum mechanical theories.

Since 2000, there has been a “Renaissance” in the field of magnetoelectricity with the achievement of “Giant ME voltage coefficients” of up to ten thousand – yes  $10^4$  – that of previously known materials.<sup>27-30</sup> These giant ME effects were reported in laminated composites consisting of piezoelectric and magnetostrictive layers.

Laminated composites have been constructed by co-sintering and by epoxy methods.

Co-sintered ME laminates have been made from perovskite ferroelectric and ferrite magnetostrictive layers, such as:  $\text{Pb}(\text{Zr}_{1-x}\text{Ti}_x)\text{O}_3$  (PZT) and  $\text{CoFe}_2\text{O}_4$  (CFO), PZT and  $\text{NiFe}_2\text{O}_4$  (NFO), and PZT and  $\text{Co}_{1-x}\text{Zn}_x\text{Fe}_2\text{O}_4$  (CZFO).<sup>28,31,32</sup> The drawback of these composites is that co-sintering limits the choice of materials couples, and also the control of the electrical boundary conditions between layers.

Epoxyed laminated composites offer much more versatility in choice of material systems, as entirely dissimilar materials can be bonded together and the electrical boundary conditions between layers controlled by thin dielectric insulation barriers. Epoxyed laminated composites have been developed by using piezoelectric PZT or  $\text{Pb}(\text{Mg}_{1/3}\text{Nb}_{2/3})\text{O}_3\text{-PbTiO}_3$  (PMN-PT) and magnetostrictive Terfenol-D, Galfenol, or Metglass layers.<sup>33-35</sup> Fig.1-2 shows a photo of some ME laminates constructed from Terfenol-D and PZT layers epoxyed together. The shortcoming of bonding is that the epoxy will become soft at high temperature; and this will reduce the mechanical coupling between the piezoelectric and magnetostrictive layers. To date, values for the ME voltage coefficient of laminate composites have been reported to be as high as 20V/cm.Oe at quasi-static frequencies and up to 500V/cm.Oe at the electromechanical resonance drive conditions.<sup>36</sup>

The giant ME effect in the ME laminate composites has a very simple working principle. Application of magnetic field results in a shape change in the magnetostrictive layer; the magnetostrictive layer is elastically bonded to a piezoelectric one; the elastic-elastic coupling between layers then results in an

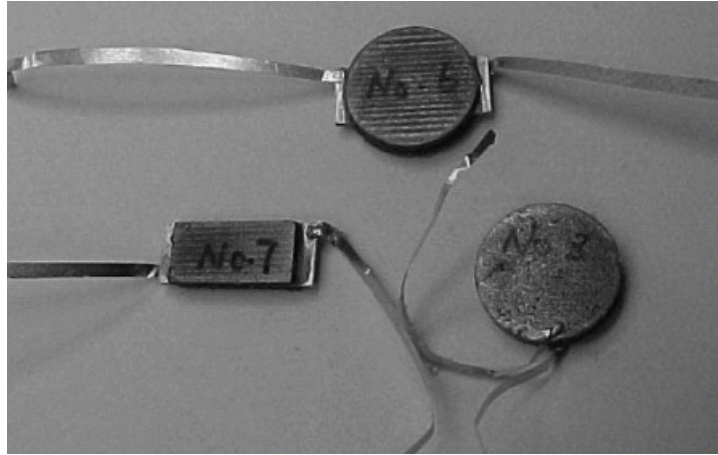


**Fig.1-2.** Disc ME laminate constructed by Terfenol-D and PZT.<sup>33</sup>

Reprinted Fig.1-2 with permission from Ref [33] as follows: S. X. Dong, J. F. Li and D. Viehland, IEEE Trans. Ultrason. Ferroelectr. Freq. Control, 51, 793 (2004). Copyright (2004) by the IEEE.

induced shape change transmitted to the piezoelectric layer; in turn, charge is generated across the piezoelectric layer by an applied magnetic field. This simple working principle has been manifested in notably more complex theories, in particular (i) continuum mechanical, and (ii) equivalent circuit ones.<sup>2, 37</sup> The elastic-elastic coupling between layers is very important. An interfacial coupling parameter ( $k$ ) has been introduced by Bichurin where the maximum ideal value is  $k=1$ , and where real interfaces have values of  $k<1$ . The higher the coupling parameter, the higher the ME effect is. In this regard, many coupling methods have been studied, including sintering, hot moulding, sputtering, and epoxy. Each method has its merit and working conditions, proper choice from these coupling methods can enhance the  $k$  factor.<sup>37-39</sup>

To achieve an optimum ME coefficient for a ME laminate, it is necessary to put the ME laminate under a critical or required DC magnetic bias.<sup>27-39</sup> This is because the magnetic phase is magnetostrictive, rather than piezomagnetic. Demagnetizing field then result in a loss of magnetic remanence on removal of the field. Rather, these composite materials must be DC biased to the maximum point of slope on the  $\epsilon$ - $H$  (magnetostrictive strain-magnetic field) and the  $M$ - $H$  curves. Because the demagnetization factor depends on geometry, the required DC bias to achieve the maximum value of  $\alpha_{ME}$  strongly depends on the construction and geometry of the composite. It is thus equally important to talk about the composites mode of operation, as well as the materials it is constructed from.

### **1.1.2 Different mode ME laminates**

As was mentioned previously, ME laminate composites need an optimized DC

magnetic bias to achieve their best ME performance, and different constructions and geometries of the composite might require different optimized DC bias levels. Since the first ME laminate was reported, many different laminate constructions have been investigated. We can classify these different structures into four basic types, by identifying the direction of the magnetization and polarization, as summarized in Table I-I. In a composite consisting of two or more layers with two different order parameters, we can specify four basic ME configurations where the magnetization is along the longitudinal (L) or transverse (T) directions of the long axis of the composite, and likewise for the polarization direction of the piezoelectric layer(s).<sup>40</sup>

The fundamental structures of these four basic modes are shown for tri-layer composites in Fig.1-3.<sup>33</sup> The ME voltage coefficient - DC bias dependence curves for these modes are illustrated in Fig.1-4. We can see that the optimized DC bias for the L-modes (L-L, L-T) are lower than that of T-modes (T-L, T-T), and the largest ME response for ME laminates in the L-mode is larger than that in T-mode. This indicates us that the L-modes should be the first choice in ME device designs.

Theoretically, the L-L mode has a higher ME voltage coefficient than the other three, due to the fact that L-L mode makes full use of the  $d_{33}$  of the piezoelectric phase while the others prefer  $d_{31}$ ; and  $d_{33}$  is larger than  $d_{31}$  for the giant piezoelectric materials, such as PZT, PMN-PT and PZM-PT. However, the ME laminates in L-L mode have a low capacitance which makes it easily to be affected by the stray capacitance of the measurement system. The problem becomes even more severe as we use Metglass as the magnetostrictive phase. Since the Metglass is very thin, a high

*Table I-I. Different modes ME lamiante.*

	Polarization	Longitudinal	Transverse
Magnetization			
Longitudinal		<b>L-L Mode</b>	<b>L-T mode</b>
Transverse		<b>T-L mode</b>	<b>T-T mode</b>

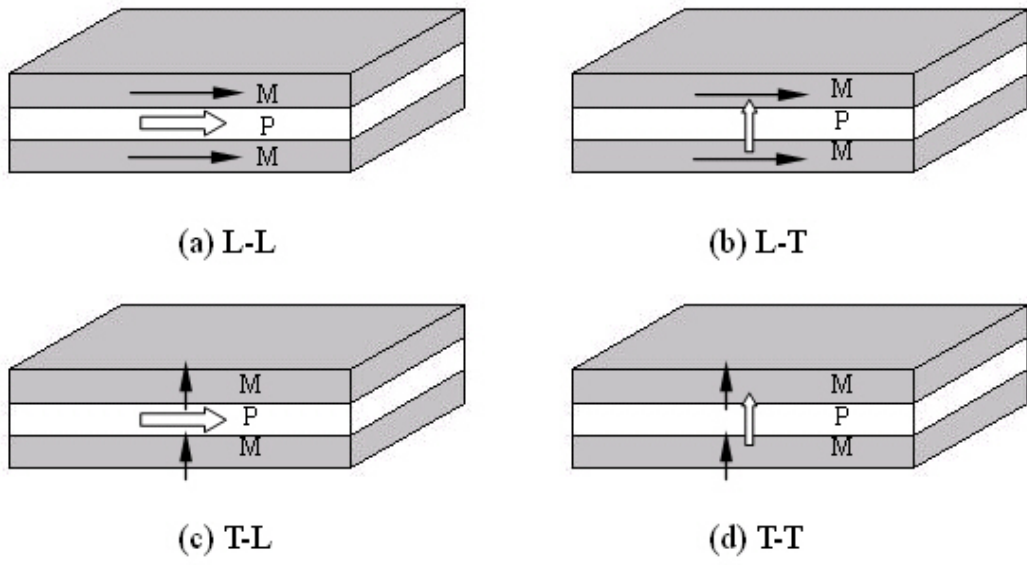


**Fig.1-3.** Fundamental ME structure.

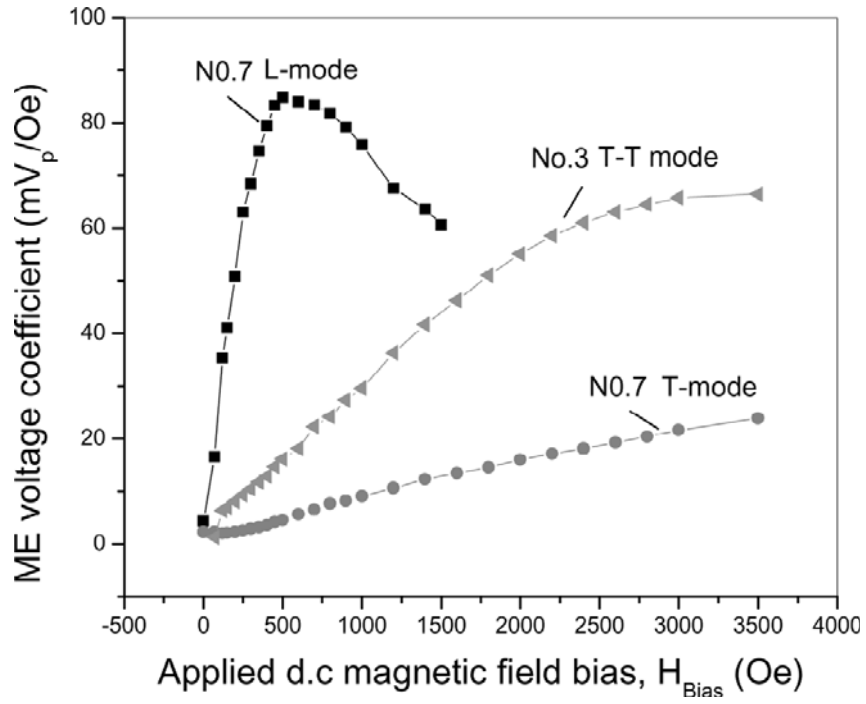
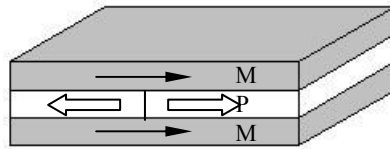


**Fig.1-4.** ME voltage coefficient DC bias dependence for L-mode and T-mode.<sup>33</sup>

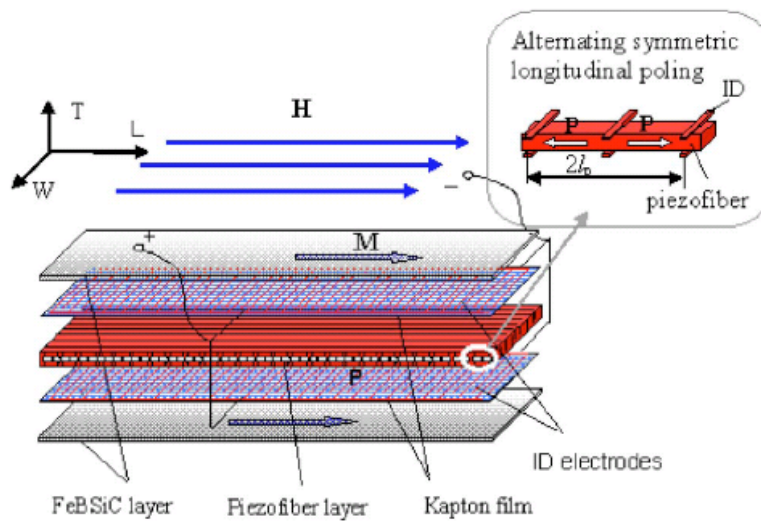
Reprinted Fig.1-4 with permission from Ref [33] as follows: S. X. Dong, J. F. Li and D. Viehland, IEEE Trans. Ultrason. Ferroelectr. Freq. Control, 51, 793 (2004). Copyright (2004) by the IEEE.

ME voltage coefficient requires the design of the piezoelectric phase needs to be very thin also (optimized design requirement). This makes the electrodes effective surface area of the piezoelectric phase small; and accordingly, the capacitance is reduced. To solve this problem, ME laminates in a L-L push-pull mode were developed, as illustrated in Fig.1-5(a).<sup>41</sup> The capacitance of the ME laminates in the L-L push-pull mode is about four times larger than that of the ME laminates in the L-L mode with the same size. If a larger capacitance is required, a multi-push-pull structure, which is illustrated in Fig.1-5(b), can help.<sup>36</sup>

The four basic modes/configurations and the L-L push-pull mode are symmetric in construction: resulting in a symmetric response distribution to applied magnetic, electric, and stress fields. However, more complex non-symmetric configurations are possible. Unimorph and bimorph structures, illustrated in Fig.1-6, are two typical asymmetric structures which have a longitudinal magnetization and a transverse polarization.<sup>42, 43</sup> A unimorph is constructed using a single magnetostrictive layer and one piezoelectric layer. Fabrication of a unimorph is easy; however, it has been shown to possess substantial environmental noise contribution. In fact, this is a common theme to a number of ME modes: this is because the polarization is also coupled to temperature. Pyroelectric current induced by thermal fluctuations in the environment can result in significant background noises. This difficulty with pyroelectric noise can be overcome by use of a bimorph structure, where the piezoelectric layer in fact consists of two layers epoxied together that are poled in opposite directions, which are then epoxied to a magnetostrictive layer. Such bimorph constructions are useful for



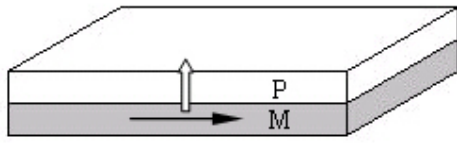
(a)



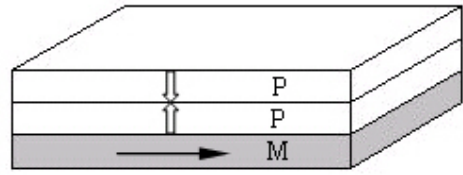
(b)

**Fig.1-5.** Structure of (a) L-L push-pull and (b) Multi push-pull.<sup>36</sup>

Reprinted with permission from Ref [44]. Copyright [2006], American Institute of Physics. Full citation format is as follows: S. X. Dong, J. Y. Zhai, J. F. Li and D. Viehland, Appl. Phys. Lett., 89, 252904 (2006).



(a) Unimorph



(b) Bimorph

**Fig.1-6.** Structure of (a) unimorph and (b) Bimorph.

canceling pyroelectric noise, but not for rejecting bending mode noise from acoustic sources.

The Ring mode is also a very useful ME structure, which was illustrated in Fig.1-7.<sup>44</sup> ME laminates constructed in a ring mode can be used to detect vortex magnetic fields which can be excited by a wire carrying a current  $I$ . ME laminates working in a ring mode can provide much higher sensitivity than reluctance coils in the frequency range from sub-Hz to several kHz. However, due to the low resistivity of the magnetostrictive phase used in the ME laminate, Eddy current losses limit its application at high frequencies.

## **1.2 The potential of ME laminates as magnetic field sensors**

Recent investigations of ME laminates sensors have shown that they have remarkable potential to detect minute changes in magnetic fields. Using a lock-in amplifier method, Dong et al. have shown the feasibility of detecting magnetic field changes on the order of  $10^{-12}$  Tesla at near quasi-static frequencies of  $f > 1\text{Hz}$ .

This is an important achievement because the ME sensor does not itself require powering; rather it can harvest magnetic energy from inductances as a stored charge across a capacitor. Thus, ME laminates are small, passive magnetic field sensors with the potential of pico-Tesla sensitivity at low frequencies while operated at room temperature. The potential for ME sensors resides with the fact that there are no other present generations of magnetic sensors having the following key requirements for surveillance devices: (i) extreme sensitivity ( $\sim \text{pT/Hz}^{1/2}$ ), allowing for better magnetic

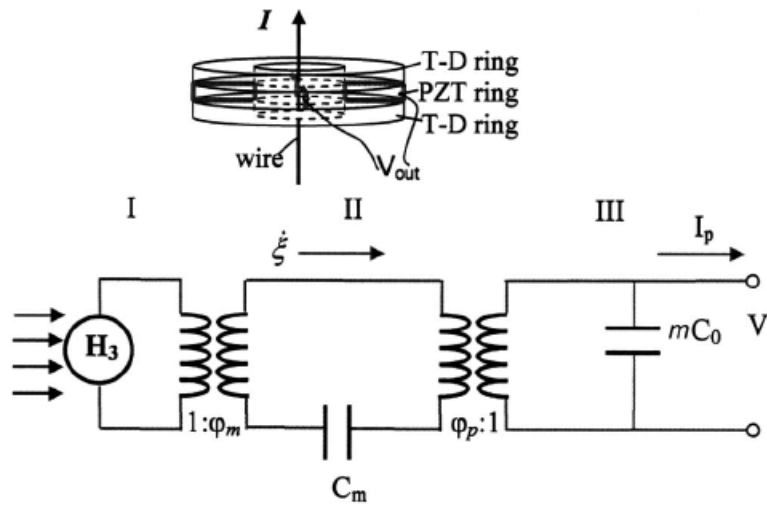


**Fig.1-7.** ME laminate works in ring mode and the equivalent circuitry.<sup>44</sup>

Reprinted with permission from Ref [44]. Copyright [2004], American Institute of Physics. Full citation format is as follows: S. X. Dong, J. F. Li and D. Viehland, Appl. Phys. Lett., 85, 2307 (2004).

anomaly detection; (ii) zero power consumption to foster long-term operation; (iii) operation at low frequencies,  $f \sim 1\text{Hz}$ ; (iv) miniaturize size, enabling deployment of arrays; (v) passive; and (vi) low cost. A comparison of various magnetic sensor technologies is given in Table I-II.<sup>45-48</sup> Inspection of this table will reveal that ME laminate sensors are the only ones with the potential to achieve all key requirements (i)~(vi).

However, in spite of this potential, actual ME sensor units have not yet been constructed. It is obvious that lock-in amplifier detection schemes will offer no net benefit to highly sensitive passive magnetometers: as the lock-in needs a reference signal, and also it is large and consumes significant power. The integration of ME laminates into an appropriate detection scheme has yet to be achieved. This detection scheme must be simple and capable of detecting anomalies in the time domain capture mode without either signal averaging or phase referencing.

### **1.3 Noise sources and their mitigation**

Generally, noise is referred to any unwanted disturbance that obscures the signal of interest.<sup>49-51</sup> It plays a very important role in the measurement of minute signals. The sensitivity of a sensor is often limited by noise, so to reduce the noise effect on the detection unit is quite important. Noise can be classified as external noise and internal noise. We will review the fundamental noise sources, how noise might affect our ME detection unit, and some proper ways by which noise can be mitigated.



### 1.3.1. External noise

External noise comes from the interaction between the detection unit and the environment. It is also named as interference or environmental noise. The interference can be electrical, magnetic, vibrational, thermal, humidity, chemical, etc.<sup>50, 52, 53</sup> To identify how the external noise affects the detection unit, it is necessary to determine three main elements that produce the noise problem. These three elements are the noise source, the noise receptor, and the coupling between them.

Conductive coupling, also known as direct coupling, is a very common, but an often overlooked coupling type. The noise receptor is affected by the noise source through a direct conductor, not only in AC but also in DC. Conductive coupling can always be seen in the design of common impedance and common power supply.<sup>50</sup> Fig.1-8 illustrates how noise couples through common impedance. Several circuits share a common return path; this common path has common ground impedance. When there is a ground current change in the circuit, the voltage drop in this common ground impedance will change. As a result, all circuit “ground” levels connected to this common path will change. This coupling becomes severe when low level circuits and high level circuits share the same ground return path. Separate ground systems are the best way to solve this kind of problem.

Electric and magnetic field coupling, or electromagnetic interference (EMI), is also a very common noise coupling type. With the development of electricity, communications, computer and automation, the electromagnetic field is almost everywhere on earth. To exactly answer how the EMI noise affects a detection system,

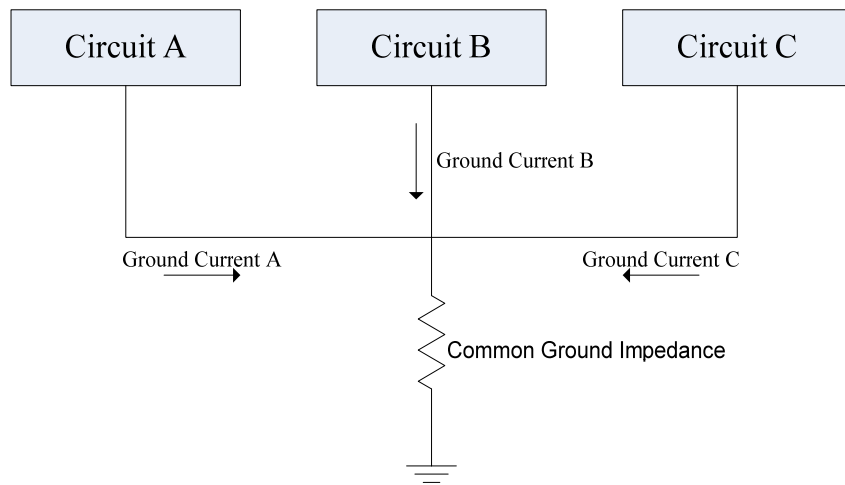
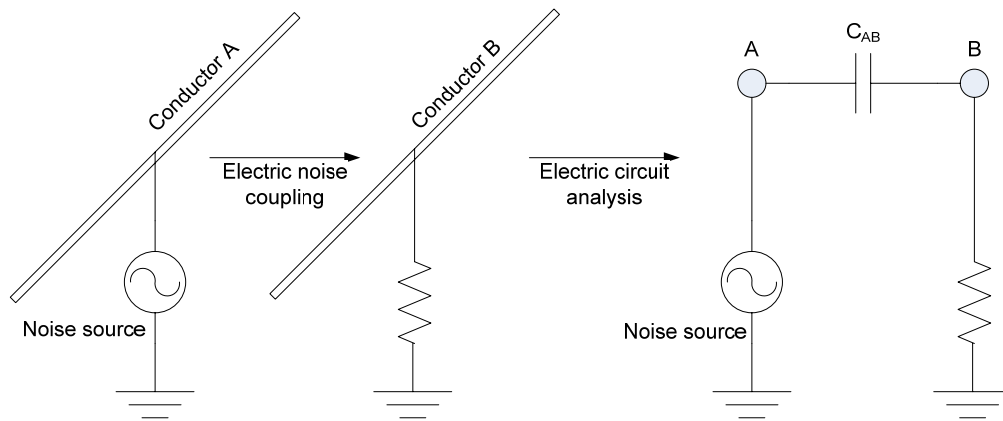


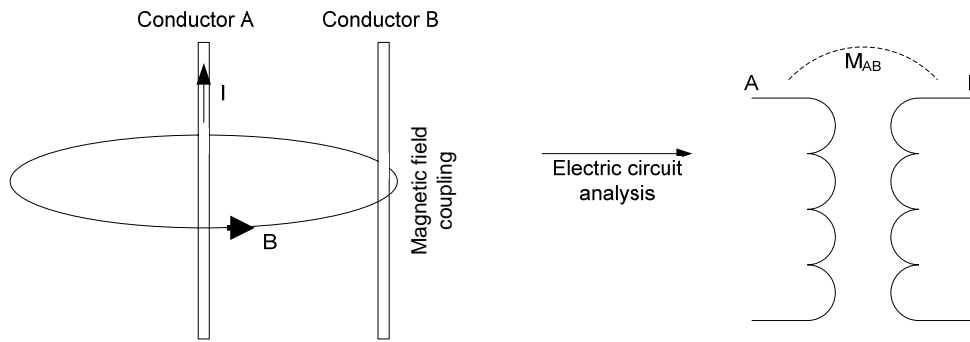
**Fig.1-8.** Direct coupling by common ground impedance.

Maxwell's equations should be solved. However, the solution is pretty complex even if the system is a simple one. As an alternative, an "electric circuit analysis" method can be used to understand how EMI noise couples into a detector without solving Maxwell's equations.<sup>50, 52</sup> In this method, coupling between the noise sources and the receptors can be represented by capacitors for the electric field, or inductors for the magnetic field. Fig.1-9 illustrated two examples of this approach. Note that this method is limited to the condition that the physical sizes of the circuits are small compared to the noise wavelength. Although the "electric circuit analysis" method can not give exact numerical results, it can show us clearly how the noise is related to the system parameters. EMI can be suppressed by proper grounding, shielding, and filtering techniques. However, at low frequencies, magnetic flux can penetrate deeply into a shield box. A high  $\mu$  metal multi-chamber is a required for the low frequency low noise measurement.

Vibration noise affects the detection unit via the piezoelectric or tribo-electric effects.<sup>53</sup> For sensors constructed using piezoelectric materials (such as PZT, PMN-PT, etc), the piezoelectric effect has the potential to contribute quite significantly to noise. Accordingly, the sensor should incorporate some means to cancel or isolate part, if not most, of this noise contribution. The triboelectric effect refers to the charge generated by friction between two different certain materials. This effect can often be seen when we sweep dry hair by combs, rub glasses by silk, or friction between human skin and cloth, etc. The accumulated charge in human skin can often induce a permanent damage to integrated circuits by electrostatic discharge (ESD). In measurements, the



(a)



(b)

**Fig.1-9.** Electric circuit analysis for (a) electric coupling and (b) magnetic coupling.

triboelectric effect occurs in coaxial cables. As illustrated in Fig.1-10, the noise charge is generated by the frictional motion of the coaxial cable.<sup>53</sup> So, to reduce the noise effect of the piezoelectricity and triboelectricity, it is necessary to isolate the measurement system from the vibration source. The vibration noise source can be building vibrations, motor rotations, human motion, fluids flowing in the pipe, for examples. For good vibration noise isolation, a floating table is highly recommended; and if possible, an isolating base needs to be constructed especially in the low frequency low noise measurement case. Traditional coaxial cable should be replaced by low noise cables in the connection of the sensor to the front end of the circuitry.

Temperature fluctuation noise, sometimes also referred to (external) thermal noise, affects a sensor detection unit via the pyroelectric effect or the thermoelectric effects. The pyroelectric effect refers to the fact that certain materials of lower crystal symmetry generate an electrical potential when they are heated or cooled.<sup>54</sup> All piezoelectric materials have pyroelectricity. Thus, ME laminates, which all use piezoelectric layers in their construction, have a built-in sensitivity to temperature fluctuations. However, a differential structure can be designed to be thermally symmetric. In this case, the ME sensor will work well even in a temperature fluctuating environment, since the thermal symmetric structure will automatically cancel the external thermal noise. The thermoelectric effect, also called the Seebeck effect, refers to the voltage that is generated by joining dissimilar materials together at temperatures above absolute zero.<sup>55</sup> Fig.1-11 illustrates how the thermoelectric effect works: when two dissimilar materials (A and B) are jointed at two points which are at

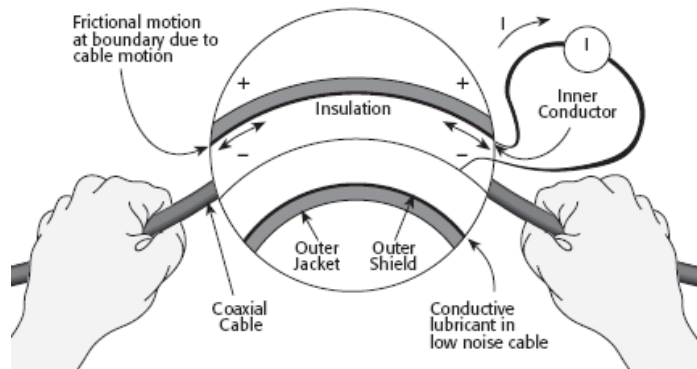


**Fig.1-10.** Triboelectric effect in coaxial cable.<sup>53</sup>

*(Image has been provided courtesy of Keithley Instruments)*

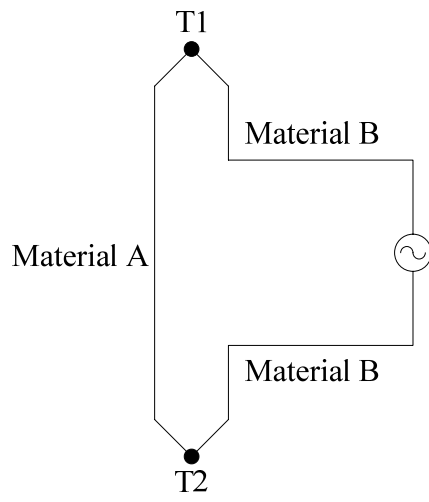


**Fig.1-11.** Seebeck effect.

different temperatures (T1 and T2), we can acquire a voltage at the output. By using this effect, thermocouples have been constructed for over a century. However, this effect also introduces noise in sensor units constructed of dissimilar materials such as ME composites. To reduce the effect of temperature fluctuations on the sensor units, one should keep a detection unit as far as possible from a thermal source, build thermal buffers for the detection unit, and allow the system to achieve thermal stability before performing measurements.

Electrochemical noise refers to the fluctuation in corrosion potential or corrosion current flow.<sup>50, 53</sup> This effect takes place when a chemical reaction occurs between two different inductors, forming weak batteries or electrochemical cells. When the humidity of the environment is high, the sensor or the front end of the amplifier is contaminated, this electrochemical noise always appears. Fig.1-12 illustrates a typical example of this effect which occurs on a sensor. Electrochemical noise is a low frequency noise and is always a problem for low frequency low noise measurements, To reduce this effect, it is very important to keep the system clean and dry. Pure solvent (acetone, alcohol, etc) is highly recommended for dissolving the oil and other contaminates from the sensitive parts (the surface of the sensors, the front ends of the amplifier) of the measurement system, and if possible an ultrasonic cleaning can help. Drying the detection unit for several hours and then allowing to stand for several hours to reach thermal equilibrium also can be help. In lab environments should be kept in low humidity (<30% is recommended), and if not desiccants should be used to reduce the humidity of the measurement area. Vacuum tubes are highly recommended

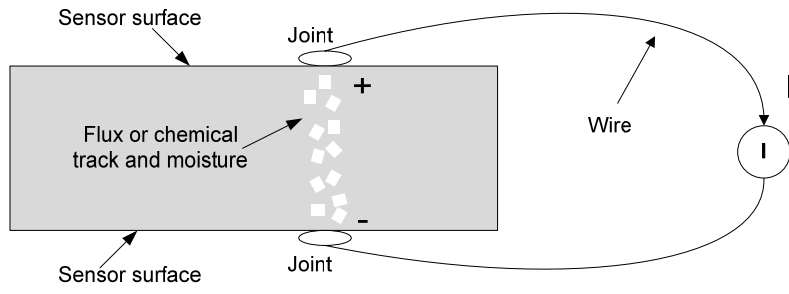


**Fig.1-12.** Electrochemical effect on sensor.

for copulating the sensor and the front end of the amplifier.

### 1.3.2 Internal noise

We have introduced some fundamental external noise effects and the techniques by which to reduce them above. However, even if we remove all the external noise effects, the sensor itself and the measurement circuitry will still contribute some inherent noise. This kind of noise can not be removed; it comes from random phenomenon of nature: such as thermal agitation of electrons in resistors, radiation fluctuations between sensor and environment, generation and recombination of electron-hole pair in semiconductors, and current flows across a potential barrier in materials. This inherent noise is also named as intrinsic noise or internal noise. There are five general types of intrinsic noise, these are:<sup>51, 56-60</sup>

- (1) Thermal noise
- (2) Shot noise
- (3) Flicker noise
- (4) Burst noise
- (5) Avalanche noise

Thermal noise is caused by the thermal agitation of electrons in a conductor. It is present in all passive resistive elements. The thermal noise was earlier predicted by Schottky based on the Brownian motion, and later experimentally confirmed by Johnson and theoretically analyzed by Nyquist in 1928.<sup>61, 62</sup> Thermal noise is also called Johnson or Nyquist noise. The thermal noise across a resistor can be given as:<sup>56</sup>

$$V_n = \sqrt{4 \cdot k \cdot T \cdot R \cdot \Delta f} ; \quad (1.1)$$

where  $k = 1.38 \times 10^{-23} \text{ J/K}$  is the Boltzmann's constant,  $T$  the absolute temperature,  $R$  the resistance and  $\Delta f$  the noise bandwidth. Noise power of the thermal noise is proportional to the noise bandwidth, and the power spectrum density does not change with frequency. So, thermal noise is a “white noise”, in comparison to those noise spectrums with frequency dependence. We can model the thermal noise of a resistor by using two simple noise models: Which are the Thevenin noise model and the Norton noise model, both illustrated in Fig.1-13, where  $I_n = \sqrt{\frac{4 \cdot k \cdot T}{R} \cdot \Delta f}$  is the noise equivalent current.

Shot noise was also earlier predicted by Schottky. It arises whenever charge crosses a potential barrier. When electrons encounter a potential barrier, energy will accumulate until they have enough energy to pass the barrier: it is a little bit like the energy release of an earthquake. The rms value of the shot noise can be given by<sup>56</sup>

$$I_{sh} = \sqrt{2 \cdot q \cdot I_{DC} \cdot \Delta f} ; \quad (1.2)$$

where  $q = 1.6 \times 10^{-19} \text{ C}$  is the electron charge and  $I_{DC}$  the DC current through the barrier. From equation (1.2), we can see that the noise spectrum density is also frequency independent. It is a kind of white noise. Note that shot noise is temperature independent and will stop whenever the current flow stops.

Flicker noise, also called  $1/f$  noise, is present in all active and many passive devices. The physical explanation of its origin is still unsolved, but it was believed that this noise is related to the contact between the particles of two different materials. Flicker noise is only accompanied with a DC current, and the rms value can be estimated as:<sup>56</sup>

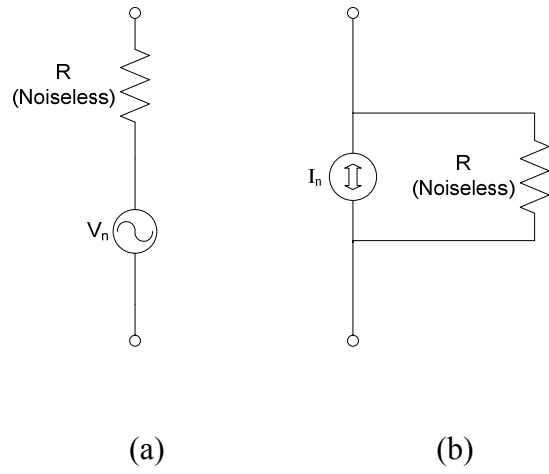


**Fig.1-13.** (a) Thevenin noise model of resistor. (b) Norton noise model of resistor.

$$I_f = \sqrt{\frac{K_f I^m \cdot \Delta f}{f^n}}; \quad (1.3)$$

where  $K_f$  is the flicker noise coefficient,  $I$  the DC current,  $m$  the flicker noise exponent,  $f$  frequency in Hz and  $n \approx 1$ . From equation (1.3), we can see that the current noise spectrum density of  $1/f$  noise is frequency dependence, and will increase as the frequency decreasing. This noise will be a severe problem when the measurement is carried out at low frequency. In resistors,  $1/f$  noise is also called excess noise. I introduce the fundamental thermal noise in passive resistors previously, where we could see that resistors with the same resistance always had identical thermal noise spectra. However, there is also an excess noise in addition to this fundamental thermal noise, which will become the main noise contribution at low frequencies. This is where the “excess” name comes from. Different types of resistors have different excess noises, and the choice of proper resistors with low excess noise can be referred to the excess noise behaviors in different types of resistors. Wirewound resistors generate the least excess noise, however they are expensive, limited to low values, and have poor frequency response due to their inductive nature. Evaporated-film, sputtered-film, metal-film and oxide-film resistors all contribute to low excess noises; thick-film and cermet resistors are noisier; while carbon film and carbon composite resistors are the noisiest.<sup>51</sup>

Burst noise is also called popcorn noise. It is caused by metallic imperfections in semiconductor devices. Modern processing techniques can significantly reduce their presence.<sup>51, 63</sup>

Avalanche noise appears only when a p-n junction is operated in a reverse break

down mode. Under a strong reverse electric field in a p-n junction, electrons that have enough kinetic energy will collide against the atom of the crystal lattice, creating additional electron-hole pairs. These pairs, in turn, create other pairs; which make multiplied pairs leading to an avalanche of pairs.<sup>63</sup>

However, in spite of the fact that one of the most promising areas for application of ME laminates is as magnetic sensors, there have been no investigations of the effect of self and environmental noise sources. This is a most important aspect of this investigation because for the application of sensors the signal is not as important as the signal-to-noise ratio (SNR). Important goals for my thesis will include such an investigation of noise source, both that of the ME laminate and the detection circuitry required to operate it.

## **CHAPTER 2**

### **PURPOSE OF THE THESIS**

The purpose of this dissertation was to develop optimized magnetoelectric (ME) sensor detection units. It is to make those first critical steps of turning ME laminate composites from a “materials dream” into an engineering reality. This is a goal that can not be perfect by one PHD thesis in Material science and engineering, as technological advancement in detection is on going world wide. However, I have chosen several key aspects of this larger goal as my thesis tasks. An attempt will be given to the optimization of the design.

Previous Investigations of ME laminates using the continuum mechanics and equivalent circuit modeling have provided the optimized ratio of the magnetostrictive and piezoelectric phases for the ME voltage coefficient at fixed ME laminate thicknesses. However, in sensor applications, the lowest detectable signal, or the sensitivity, is much more important. Clearly, it is necessary to increase the sensitivity of the ME detection unit. But how? To address the question, investigations on these passive ME sensors, and their detection circuits, must be carried out. Chapter 3-7 will attempt to provide answers to the following specific question:

- (1) How can we relate a practical ME device to an equivalent circuit model?

Equivalent circuit models are the best methods by which to analyze a device, especially when measurement is brought into consideration. Accordingly, I have set up an equivalent circuit model, by which I then analyze the ME sensitivity.

To setup such a model, we should know the internal relations between the

physical material parameters of the phases inside the ME laminates. However, the ME laminates are not physically independent units, rather they are fixed or clamped to a base. This insures that they are mechanically static without an input signal. These clamped or fixed conditions can be assumed to be the linear boundary conditions. We also need to know the relation between the sensor and the outside world. However, the outside boundary conditions are quite complicated, which makes analysis complex. In section 3.2, I will use another method which lumps the complex linear boundary condition into effective ME system parameters, which make ME analysis simple. Based on these “ME system equations”, my ME modeling will also include noise considerations (Please see section 3.2).

- (2) How can we estimate the ME laminate sensitivity? It is impossible to measure the ME sensitivity at all frequency points, rather, we can estimate the functional form of the sensitivity from points that we have measured. But how? In section 3.2, we will introduce the signal-to-noise ratio (SNR) of ME laminate sensors. By using my model, we can estimate the ME sensitivity at any frequency over a range from ones that have been experimentally acquired.
- (3) How can we increase the ME laminate sensitivity? This is a most important question, and an integral part of my PHD thesis. In section 1.3, I’ve shown that the noise level affects the sensitivity notably, but, low noise is not the only necessary requirement for a high sensitivity, as we also need to have a large signal: it is the signal-to-noise ratio (SNR) that matters for high sensitivity. Also

in section 1.3, I've shown for ME laminate that there are two kind of noise: internal and external. With regard to internal noise, I will induce an equation for the SNR of a ME laminate, from which we can identify the parameters that notably affect the ME sensitivity (See section 4.2.1). Two methods are identified by which the sensitivity can be significantly enhanced: "Scale effect" and "ME array" (See section 4.2). With regard to external noise, I have analyzed how thermal and vibrational noises affect the ME laminate sensitivity. Different ME laminate modes were studied (See section 4.3.2), where I have introduce two methods to reduce the vibration and the temperature fluctuation noise contribution (separately), which I designated as the symmetrical-signal unsymmetrical-noise (SS-UN) and unsymmetrical-signal symmetrical-noise (US-SN) modes (See section 4.3.2).

- (4) How to increase the ME voltage coefficient, by taking advantage of resonant frequency enhancement? In section 4.4, I will introduce a bending mode vibration approach by which to affect the resonance gain and thus enhance the low frequency ME coefficient.
- (5) How to increase the detection sensitivity in the ME circuit design? ME detection unit is not simply a ME laminate itself, but rather includes a detection circuit. This circuit must be designed to be optimized. But how? I will introduce a way by which to optimize the SNR via component value choices (See section 5.2) A new charge topology for SNR enhancement will also be discussed. (See section 5.3).

(6) How to simulate the ME detection unit in Pspice? Pspice is a very useful tool for electronics simulation. As an electronic device, ME laminates sensors should be analyzed by Spice models, including responses in time and frequency domain. Such models will be set up in section 6. Using a time domain in Pspice, I will then simulate the output signal from the input. From the frequency domain model (with noise included), I will also estimate the output noise level (See section 6.2). I will finally show that practical circuit designs can be made to approach this theory limit.

(7) Can giant ME effects appear in structures other than the magnetostrictive-piezoelectric composite? I will introduce a new ME device, with a unique coupling mechanism that does not have magnetostrictive layers. The new ME device is constructed by PZT and NbFeB magnet. (See section 7.2)

## CHAPTER 3

### MODELING OF THE ME LAMINATES

#### 3.1 Introduction

To easily understand how the magnetoelectric (ME) laminates perform in practical electrical design, it is necessary to understand how ME laminates function as electrical elements. An equivalent circuit model is the best method by which to approach this. In an equivalent circuit model, the ME laminate can be represented by a set of resistors, capacitors, inductors and transformers under some specific relations (connections). In previous research, some ME equivalent circuit models have been developed basing on the magnetostrictive constitutive equation, piezoelectric constitutive equation, and a motion equation to link them.<sup>2,37</sup> However, these models, correct in their ME voltage coefficient predictions, they did not solve the following problems:

- 1) What will the ME laminate model look like under practical linear boundary conditions? As we know, ME laminates are not physically independent units, they should be fixed or clamped to the base, or somewhere; this insures that they are mechanically static without an input signal. These clamped or fixed conditions can be assumed to be the linear boundary conditions in practice. Current ME equivalent circuit models use free-free boundary conditions, which assume that the ME laminates are free at both ends of the laminate. Although good in relating material parameters to the ME voltage coefficient, they are not

that accurate: it's an ideal case that is a little divorced from reality.

- 2) Why does the output voltage roll-off at low frequencies in direct measurements?

This is an interesting phenomenon in practical measurements. As we measure the output voltage of the ME laminate by using the direct measurement method, such as the connection of the sensor output directly to the oscilloscope or other voltage meters, the output voltage will roll-off at frequencies below several hertz. This roll-off frequency is far away from the Maxwell-Wagner relaxation region.

- 3) What will the noise be in the model? Previous models only considered the ME output signal. However, as we know what affects the sensors' sensitivity is the noise level. So, it is absolutely necessary to include noise effects in the equivalent circuit model.

In the following sections, I will present an equivalent circuit model for practical ME laminate sensor units. Practical linear boundary conditions will be included into the model. I will use this model to explain an output voltage roll-off phenomenon in the direct measurement method. Also, I will use this model to evaluate the sensitivity of the ME laminate sensors.

### 3.2 Modeling of ME laminates at low frequencies

At low frequencies, where the wavelength is much longer than that of the composites dimensions, the ME laminate composite can be considered as a homogeneous body with effective parameters. Prior studies have solved for transverse and longitudinal modes in the free and clamped conditions.<sup>2, 37</sup> However, real-world boundary conditions can be very complicated, and the exact form of the solution might not be necessary. Thus, we approximate real-world conditions by using a quasi-constitutive linear equation that considers a ‘ME sensor system’, given as

$${}^s D_k = {}^s d_{ki} {}^s T_i + {}^s \varepsilon_{kj} {}^s E_j + {}^s m_{kn} {}^s H_n ; \quad (3.1)$$

where  ${}^s D_k$ ,  ${}^s T_i$ ,  ${}^s E_j$ ,  ${}^s H_n$ ,  ${}^s d_{ki}$ ,  ${}^s \varepsilon_{kj}$ ,  ${}^s m_{kn}$  are the dielectric displacement, effective stress, electric field, magnetic field, piezoelectric coefficient, permittivity and permeability of the ME laminate sensor system.

To understand real-word ME sensor detection units with (3.1), a simple equivalent model might be helpful, as we can then model the electrical parameters of sensor and detection circuitry lumped together. If we consider such an approximation, then in the absence of mechanical stress and magnetic field, equation (3.1) simplifies to

$${}^s D_k = {}^s \varepsilon_{kn} {}^s E_n . \quad (3.2)$$

The effective permittivity of the ME laminate is a complex matrix, whose real and imaginary components are both frequency dependent. The complex permittivity is given by

$${}^s \varepsilon_{kn}^* (\omega) = {}^s \varepsilon_{kn}^1 (\omega) - j {}^s \varepsilon_{kn}^2 (\omega) = {}^s \varepsilon_{kn}^o (\omega) e^{-j\theta} ; \quad (3.3)$$

where  $\omega$  is the angular frequency in rad/s,  ${}^s\varepsilon_{kn}^1(\omega)$  and  ${}^s\varepsilon_{kn}^2(\omega)$  are the real and imaginary parts of the  ${}^s\varepsilon_{kn}^*(\omega)$  matrix. Since  ${}^s\varepsilon_{kn}^o(\omega)$  is the modulus of  ${}^s\varepsilon_{kn}^*(\omega)$  and  $\tan\theta = {}^s\varepsilon_{kn}^2(\omega)/{}^s\varepsilon_{kn}^1(\omega)$ , we can see that phase angle  $\theta$  between the E and D vectors is also frequency dependent.

Since D and the output charge Q are related by  $Q=D\cdot A$  (where A is the electrode's effective surface area), the current I(t) produced by the piezoelectric phase can be acquired by the differential of the charge Q in the time domain

$$I(t) = \frac{dQ(t)}{dt}. \quad (3.4)$$

We can use the Laplace operation  $L(\sim)$  to transform this into an equation in terms of the complex frequency  $s=\sigma+j\omega$  (where,  $\sigma$  is the neper frequency, and  $\omega$  the angular frequency) as follows

$$I(s) = L(I(t)) = L\left(\frac{dQ(t)}{dt}\right) = sQ(s) - Q_0; \quad (3.5a)$$

where  $Q_0$  is a constant. Assuming a sinusoidal excitation, we can replace s with  $j\omega$  and set the initial condition to make  $Q_0=0$ . Thus, (2.5a) can be rewritten as

$$I(j\omega) = j\omega \cdot Q(j\omega). \quad (3.5b)$$

We can then acquire the admittance G of the ME sensor system by using (3.2), (3.3) and (3.5b), as follows

$$G = \frac{I}{V} = \frac{I}{E \cdot t} = \frac{I \cdot \varepsilon_0 \cdot e^{-j\theta}}{D \cdot t} = \frac{I \cdot A \cdot \varepsilon_0 \cdot e^{-j\theta}}{Q \cdot t} = \frac{A \cdot \omega \cdot \varepsilon_0}{t} (\sin \theta + j \cos \theta); \quad (3.6)$$

where A is the effective electrode area of the ME sensor. A parallel equivalent model can then be set-up following (3.6), as illustrated in Fig.3-1, where  $R = \frac{t}{A \cdot \omega \cdot \varepsilon_0 \cdot \sin \theta}$  and

$$C = \frac{A \cdot \varepsilon_0 \cdot \cos \theta}{t}.$$

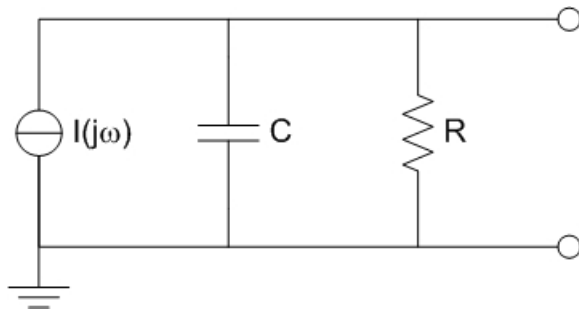


**Fig.3-1.** Fundamental ME equivalent model.

Next we can define a fundamental parameter, named the ME charge coefficient  $\alpha_{me}$ , as  $\alpha_{me}^* = \delta Q / \delta H$ . This fundamental parameter is also complex:

$$\alpha_{me}^*(\omega) = \alpha_1(\omega) - j\alpha_2(\omega) = \alpha_0(\omega)e^{-j\phi}; \quad (3.7)$$

where  $\alpha_1(\omega)$  and  $-\alpha_2(\omega)$  are the real and imaginary parts;  $\alpha_0(\omega)$  is the modulus of  $\alpha_{me}^*(\omega)$  and  $\tan\phi = \alpha_2(\omega)/\alpha_1(\omega)$ . The angle  $\phi$  is the phase delay of Q in response to H, which is also frequency dependent. Since

$$Q(t) = \alpha_{me}^*(\omega)H(t) = \alpha_0(\omega)e^{-j\phi}H(t), \quad (3.8)$$

we can then rewrite (2.5b) as

$$I(j\omega) = \alpha_0(\omega) \cdot e^{-j\phi} \cdot j\omega \cdot H(j\omega) = j\omega \cdot \alpha' \cdot H(j\omega). \quad (3.9)$$

By combining (3.9) with Fig.3-1, we can now set up a modified model for the ME sensor, as given in Fig.3-2. This is a simple ME sensor signal model. Since at high frequency the stray capacitor, resistor and inductor become important, significant error will be introduced by the model: thus, it is only suitable for the case of low frequencies.

The model shown in Fig.3-2 can be used to explain the experimental data for the case of ME direct measurements, where the output voltage rolls off with decreasing frequency at low frequencies. In this case, the equivalent model is shown in Fig.3-3(a), and the detected voltage is given by

$$V_0 = I(j\omega) \cdot Z = \frac{j\omega \cdot \alpha' \cdot R'}{1 + j\omega \cdot R' C'} \cdot H(j\omega); \quad (3.10)$$

where  $R' = R/R_0$  and  $C' = C/C_0$ ;  $R_0$  and  $C_0$  are the input resistance and input capacitance (including stray contributions) of the detection instrument (such as, an oscilloscope, multi-meter, etc).

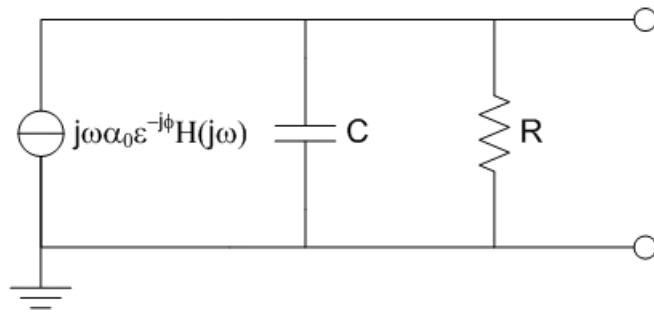
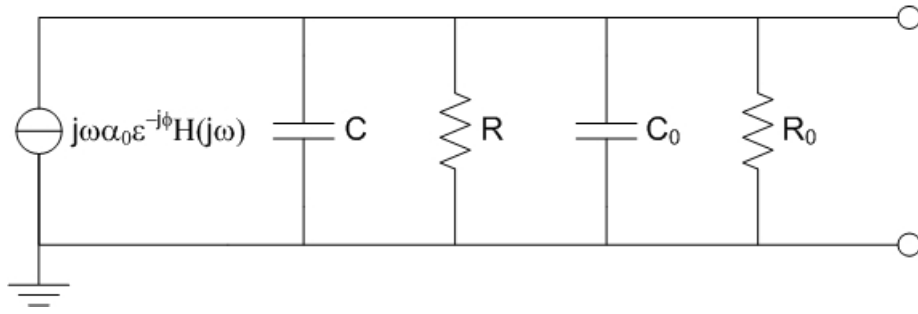
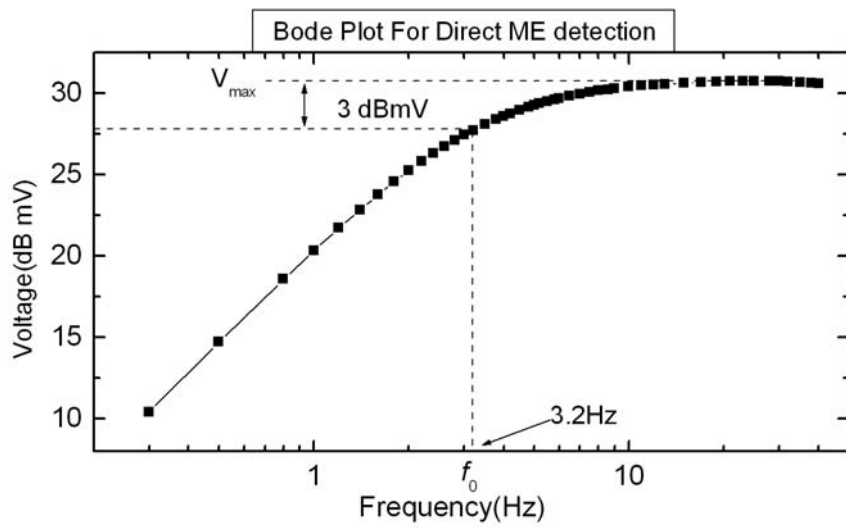


**Fig.3-2.** ME laminate signal model.



(a)



(b)

**Fig.3-3.** (a)An equivalent circuitry for ME laminate with direct measurement method; (b)voltage as a function of frequency in ME direct measurement, illustrating a cut-off frequency below which shows significant roll-off occurs with decreasing frequency.

Following (3.10), there is a zero point at  $\omega=0$  and a pole at  $\omega=1/(R'C')$ : thus, there is a high cut-off frequency which can be determined to be  $1/(2\pi R'C')$ . Generally,  $R' \approx R_0$  and  $C' \approx C$  simply because  $R \gg R_0$  and  $C \gg C_0$ . The voltage meter we used had an input impedance of 10M/15pF, and a stray capacitance of  $\sim 10$ pF; and the ME laminate we used here had a capacitance of  $C_1=4.86$ nF. Thus, the cut-off frequency can be calculated as 3.2Hz, which coincides well with the experimental results shown in Fig.3-3(b).

In practical ME sensor measurements, noise will always limit sensitivity. In a ME detection unit, we must consider two types of noise: intrinsic noise (Johnson, contact, etc) and external noise (vibration, pyroelectric, etc). We can refer all these noise sources to the input as  $i_n(\omega)$ , and redraw the equivalent circuit to include them as given Fig.3-4. In this case, the SNR can be expressed as

$$SNR = \frac{I(j\omega)}{i_n(\omega)} = \frac{\alpha_0(\omega) \cdot e^{-j\phi} \cdot j\omega \cdot H(j\omega)}{i_n(\omega)}. \quad (3.11)$$

From (3.11), we can see if  $i_n(\omega)$  is less frequency dependent than the term  $\alpha_0(\omega) \cdot e^{-j\phi} \cdot \omega$ , that then the SNR will increase with increasing frequency. Generally, at low frequencies and over short bandwidths, we can make an assumption that  $|\alpha_0(\omega) \cdot e^{-j\phi}|$  is a constant. Experiments were carried out to determine the  $|\alpha_0(\omega) \cdot e^{-j\phi}|$  term. The ME laminate sample was constructed to be a L-T mode by two pieces of Terfenol-D of size  $14 \times 6 \times 1.1$ mm<sup>3</sup> and one piece of PZT of size  $15 \times 6 \times 0.5$ mm<sup>3</sup>. The applied AC Magnetic field was provided by a Helmholtz coil that oscillated under a DC bias provided by a pair of NbFeB magnets. The sensor's output was then amplified by a charge amplifier (Kistler 5015) before it was fed into the

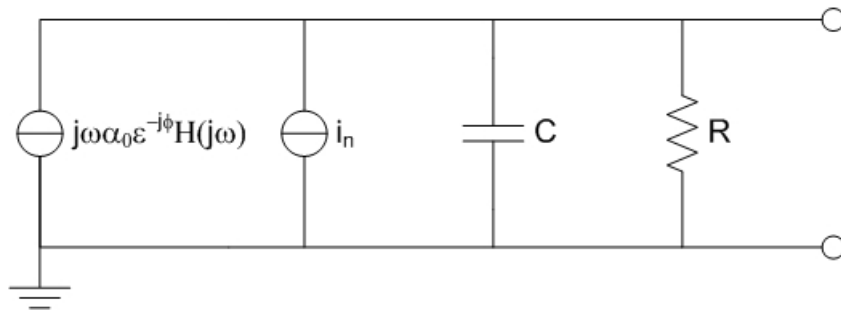


**Fig.3-4.** ME laminate model with noise consideration.

oscilloscope.

Fig.3-5 shows  $|\alpha_{me}^*|$  for this ME sensor as a function of frequency over the range of  $0.1\text{Hz} < f < 1000\text{Hz}$ . We can see in the range of  $0.1\text{Hz} < f < 100\text{Hz}$  that  $|\alpha_{me}^*|$  was nearly constant with a value of about  $130\text{pC/Oe}$ . However, for  $f > 100\text{Hz}$ ,  $|\alpha_{me}^*|$  decreased dramatically with increasing frequency. In our subsequent experiments, we focused on the frequency independent range, which is an appropriate range for detection of low frequency magnetic fields.

We also performed experiments to determine the signal linearity, the SNR and the sensitivity limit (lowest signal detectable) for this L-T mode ME sensor. An ac magnetic field was generated by Helmholtz coils, which served as the source signal to be detected, and the output of the ME sensor was measured by a Keithly 428 low noise current amplifier. The equivalent model for the ME laminate and current amplifier is illustrated in Fig.3-6. We can acquire the current gain  $Z(\omega)$  of the circuit as

$$Z(\omega) = \frac{R_f}{1 + j\omega \frac{R_f}{1+a} C} \cdot H_{LP}(j\omega); \quad (3.12)$$

where  $R_f$  is the feedback resistance,  $a$  the open loop gain of the amplifier, and  $H_{LP}(j\omega)$  the transfer function of the low pass filter.

The signal output voltage  $V_s$  and the output noise level  $V_n$  are:

$$V_s = \alpha_0(\omega) \cdot e^{-j\phi} \cdot j\omega \cdot H(j\omega) \cdot Z(\omega); \quad (3.13a)$$

$$V_n = \left( \int_{f_L}^{f_H} i_n^2 \cdot |Z(\omega)|^2 df \right)^{\frac{1}{2}}; \quad (3.13b)$$

where  $Z(\omega)$  is the current gain of the amplifier,  $f_L$  and  $f_H$  are the lower and upper frequency limits of the noise bandwidth. Over the measurement bandwidth, (3.13a) can

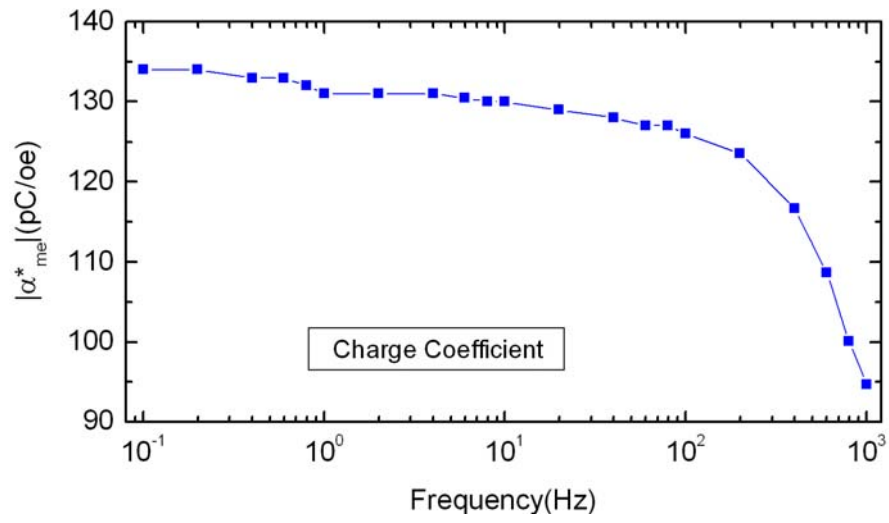


**Fig.3-5.** The magnetoelectric charge coefficient as a function of frequency, which shows a near constant value at low frequencies

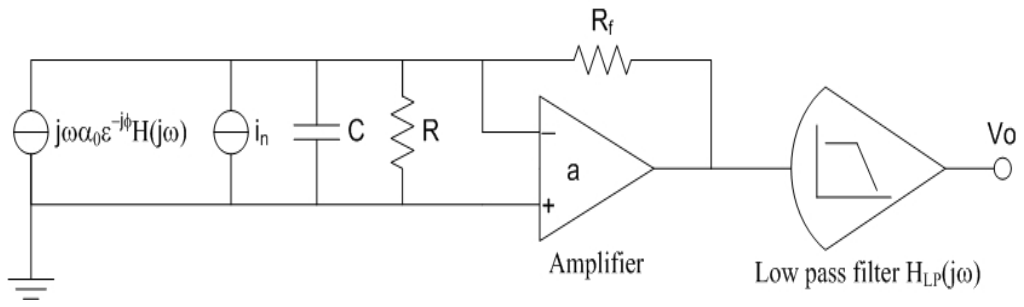


**Fig.3-6.** ME laminate with noise spectra and current amplifier.

be simplified to

$$V_s = \alpha_0(\omega) \cdot e^{-j\phi} \cdot j\omega \cdot H(j\omega) \cdot R_f \cdot H_{LP0}; \quad (3.14)$$

where  $H_{LP0}$  is the DC gain of the low pass filter. The SNR then becomes

$$SNR = \frac{V_s}{V_n} = \alpha_0(\omega) \cdot e^{-j\phi} \cdot j\omega \cdot H(j\omega) \cdot \frac{R_f \cdot H_{LP0}}{\int_{f_L}^{f_H} i_n^2 \cdot |Z|^2 df}. \quad (3.15)$$

Experiments on the ME linearity are illustrated in Fig.3-7. We can see that the ME laminate sensor unit has good linearity at 1Hz, 10Hz and 100Hz. These results agree with (3.14). It shows that  $|\alpha_0(\omega) \cdot e^{-j\phi}|$  is (i) constant at low frequencies, and (ii) independent of magnetic field in the low field range for low frequencies.

Experiments on the SNR and the sensitivity (i.e., lowest detectable magnetic field) were also carried out. To evaluate how the intrinsic noise affects the measurement unit, proper set up is required to reduce the external noise to a negligible value. The experimental results are given in Fig.3-8. In this figure, we can see with increasing frequency that the SNR increases and that the lowest detectable signal decreases. These results agree with the predictions of (3.15): that the SNR decreases near linearly with decreasing frequency over the frequency range of  $10^{-1} < f < 10^2$  Hz.

This result provide us a helpful method of ME sensitivity estimation in the low frequency range. For example, if we know a ME laminte sensor has 1nT sensitivity at 1Hz, we can then estimate that the sensitivity of the ME sensor will become 0.1nT at 10Hz and 10nT at 0.1Hz.

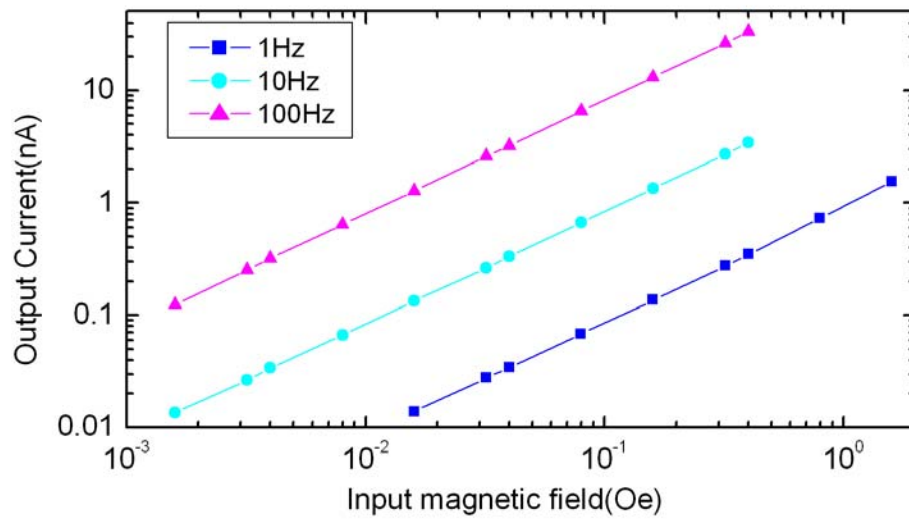


**Fig.3-7.** Linearity of the ME sensor system at 1Hz, 10Hz and 100Hz.

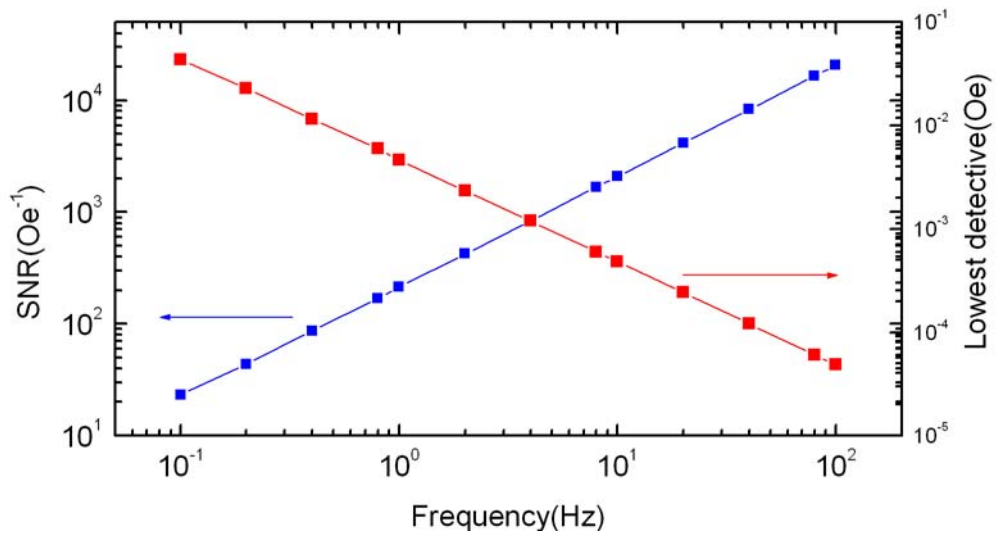


**Fig.3-8.** SNR and lowest detectable signal for LT ME laminate.

### 3.3 Summary

A ME laminate sensor model for the low frequency application was constructed based on the “ME sensor system equation”. The linear boundary conditions were lumped into the system parameters which makes the analysis easier. An output voltage roll off phenomenon in the direct measurement was successfully explained from this model and confirmed by experiment. Noise was also included in this ME system model. The SNR or sensitivity was predicted and confirmed to increase with increasing measurement frequency. This result provides insight into how to estimate the ME sensitivity in the frequency range through measurement of one at a specific frequency, and into how to enhance the sensitivity of real ME sensor units for the detection of minute variation in quasi-static magnetic fields.

*Partially Reprinted from Reference<sup>64</sup>*

# CHAPTER 4

## ME LAMINATES DESIGN OPTIMIZATION

### 4.1 Introduction

A parameter defined as  $\alpha_{ME} = \delta E / \delta H = \delta(V/t) / \delta H$  (where H is an applied magnetic field, E and V are the electric field and voltage induced across the piezoelectric layer, and t is the thickness or more accurate the effective distance between the electrodes of the piezoelectric phase)<sup>2</sup> has been widely used as a figure of merit for ME laminate composite. It is an important parameter, which can relate the ME response of various types of ME laminate configurations. However, this parameter might be a little misleading in the guidance of designing a ME sensor with a high ME response. For the laminate construction, if one increases the thickness of the active layers (which are coupled to an applied magnetic field, here referred to as the magnetostrictive layers), the energy transferred to the passive layers (which are mechanically coupled to the active layer, here referred to as the piezoelectric layers) will be increased. As a result,  $\alpha_{ME}$  will increase. This provides us insight into designing ME laminates by using magnetostrictive layers as large as possible, in order to achieve a high ME voltage coefficient: although is true in theory, difficult in practice.

In the definition of  $\alpha_{ME}$ , it would appear reasonable to use the total thickness (T) of the ME laminate, instead of simply the thickness of the piezoelectric phase. However, there are some difficulties with ME response optimization for the longitudinal polarization modes: such as L-L, T-L and push-pull. As the length of these

longitudinal polarization modes is increased, the energy (E) transferred from the magnetostrictive to the piezoelectric layers is also increased, but the capacitance C of the piezoelectric layers is decrease. As a consequence, the induced voltage V from these ME modes is increased following the relation  $E=0.5 \cdot C \cdot V^2$ .

A practical optimized design for the ME voltage coefficient requires one to fix the thickness and the length of the ME laminate, and to change the ratio of the magnetostrictive phase and piezoelectric phase. The largest ME voltage coefficient is found at a specific ratio which is designated the optimized ratio or  $\nu$ . which has been investigated by Bichurin et al. and Dong et al. using different methods: continuum mechanical method and equivalent circuit, respectively.<sup>2, 37</sup> Fig.4-1 shows typical results from these investigations of the effect of  $\nu$ . One can see that the optimized ratios for various ME constructions are different: not only with respect to changes in materials, but also with changes in operational modes. The coupling factor k will also affect this optimized ratio.

These prior investigations, although good for optimization of the ME voltage coefficient, did not reveal how they affect the sensitivity to small variations in magnetic field. Optimization of the sensor design by considering the lowest detectable signal (i.e. sensitivity) remains to be done, which must include noise considerations. To evaluate noise effects and optimize ME sensors for high sensitivity, an equivalent model that includes noise sources must be set up: which was done in Chapter three of this thesis. Here, we will use this model to study optimization methods for ME laminate sensor design. Optimization of the ME laminate sensors' sensitivity should

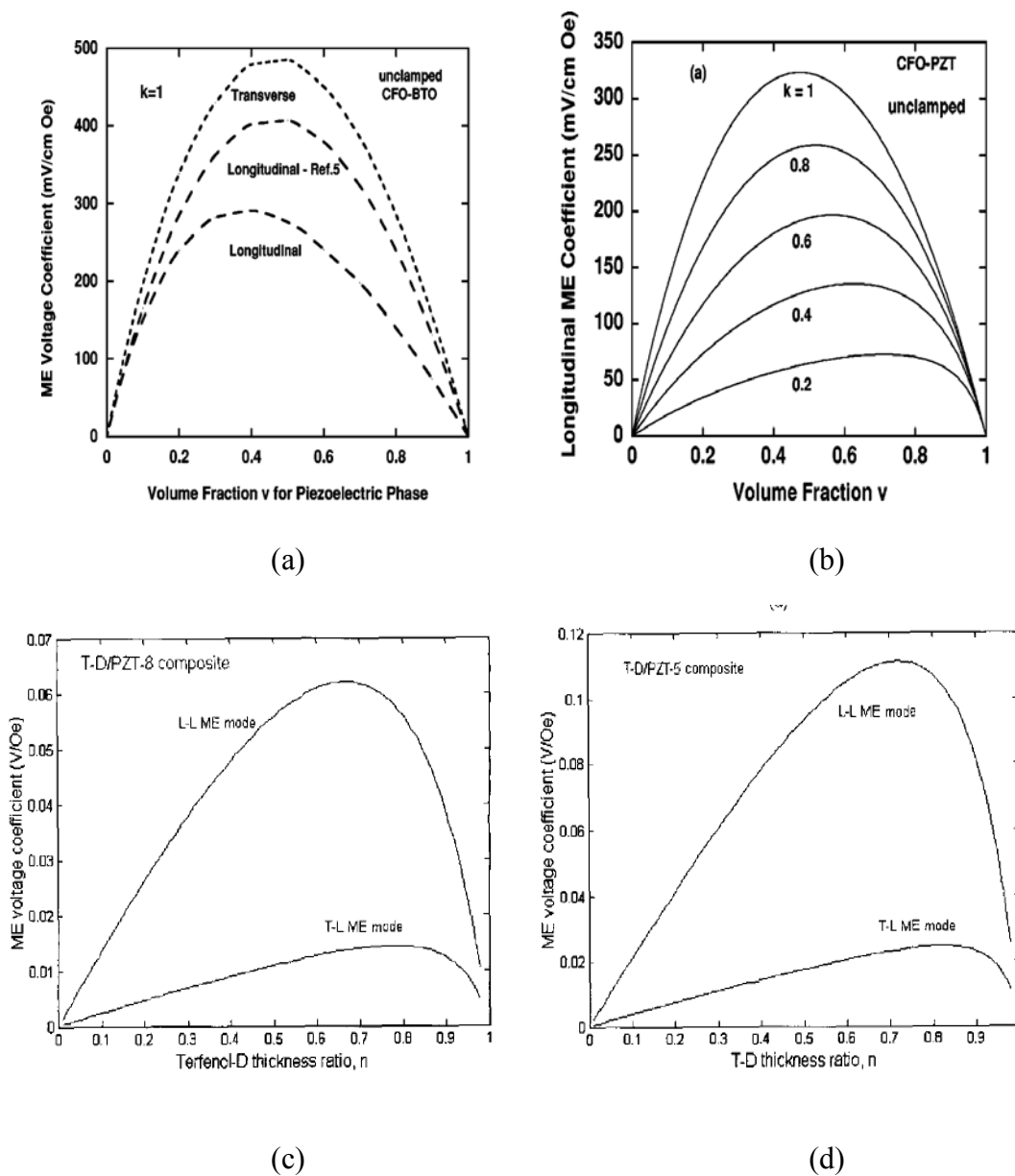


**Fig.4-1.** (a) Longitudinal and Transverse ME voltage coefficient on volume fraction  $v$  for a perfectly bonded ( $k=1$ ) two-layer structure consisting of CFO and BTO; (b) Longitudinal ME voltage coefficient on interface coupling  $k$  and volume fraction  $v$  for the CFO-PZT bilayer; Calculation values of ME voltage response on thickness ratio  $n$  for (c) Terfenol-D/PZT-8 laminate; and (d) Terfenol-D/PZT-5 laminate.<sup>2, 37</sup>

Reprinted Fig.4-1(a), (b) with permission from Ref [2] as follows: M. I. Bichurin, V. M. Petrov and G. Srinivasan, Phys. Rev. B, 68, 054402 (2003).. Copyright (2003) by the American Physical Society.

Reprinted Fig.4-1(c), (d) with permission from Ref [37] as follows: S. X. Dong, J. F. Li and D. Viehland, IEEE Trans. Ultrason. Ferroelectr. Freq. Control, 50, 1253 (2003). Copyright (2003) by the IEEE.

consider both intrinsic and external noise source. Such optimization strategies, although good for ME sensor design, has a limitation at low frequencies (far below the 1<sup>st</sup> resonant frequency).

Earlier in 1982, Tilley and Scott pointed out that the ME response could be enhanced when the applied magnetic fields is coincident with the Eigen modes of the system.<sup>65</sup> After that, Bichurin and Cai studied the frequency dependence of ME laminates, which revealed a dramatic increase of the ME voltage coefficient in the vicinity of the electromechanical resonant (RMR) frequency.<sup>38, 66, 67</sup>

Terfenol-D is often used as the magnetostrictive layer in ME laminates, due to its huge magnetostriction. However, the resistivity of Terfenol-D is quite low: being a metallic conductor. When operating at a higher frequency of >10 kHz, Eddy current losses within the Terfenol-D layer will become quite serious. This limits the efficiency of ME energy conversion at high frequency. Increasing the size of Terfenol-D can lower the resonant frequency, but this also comes at increasing cost, since rare earth Terfenol-D is expensive. An alternative method to overcome Eddy current loss might be to cut Terfenol-D into thin pieces, and then bond these pieces into stacked layers with high resistant epoxy. Unfortunately, Terfenol-D is very brittle, making it difficult to cut Terfenol-D into layers thinner than 0.5mm. A unimorph type ME Terfenol-D/PZT laminate operating in bending mode has a notably relative lower resonance frequency. However, compared with longitudinal (L-L or L-T) modes, the ME coefficient for this unimorph bending mode is also relatively low: ~15 V/cm-Oe at the 1<sup>st</sup> bending mode.<sup>42</sup> Clearly, it is an important task to design new operational

modes with decreased the resonant frequencies, while at the same time sustaining a high ME voltage coefficient.

In this chapter of my thesis, I have investigated the following aspects with respect to the above discussion:

- (i) ME sensor sensitivity optimization, including the internal noise;
- (ii) ME sensor sensitivity optimization, including the external noise; and
- (iii) Low resonant frequency ME laminate design optimization.

## 4.2 ME sensitivity optimization on considering internal noise

### 4.2.1 ME sensitivity and the scale effect

To optimize a ME laminate sensor on considering the internal noise, we need to know the main internal noise sources that affect the sensitivity. We introduced some internal noise sources in Chapter 1 of this thesis. For ME laminate sensor, we should consider three dominant internal noise sources. These internal noise sources are: (i) radiation noise  $i_G$ ; (ii) dielectric loss noise  $i_D$ ; and (iii) Johnson noise  $i_R$ .<sup>54, 68-71</sup>

Radiation noise comes from the thermal fluctuations between the sensors and the environment. In a system containing sensors, the thermal energy of the sensors will be coupled to a heat sink via thermal conductance  $G$ . The system on average may be new thermal equilibrium at a temperature  $T$ . However, even in the thermal equilibrium, thermal fluctuations occur between the sensor and the environment. This power fluctuation can be evaluated by the following relation:<sup>68</sup>

$$\Delta W_T = (4kT^2G)^{1/2}. \quad (4.1)$$

where  $k = 1.38 \times 10^{-23} \text{J/K}$  is Boltzmann constant and  $T$  the absolute temperate. From equation (4.1) we can see that the radiation noise is proportional to the thermal conductance  $G$  between the sensors and enviroment. Its minimization can be achieved by reducing the thermal conductance  $G$ . Air, wood, and foam all have low thermal conductance and should be considered in the construction of a thermal-isolated sensor system. In my experiments, I used double-stick foam bars to fix the sensor in the

middle of a base. As a result, radiation noise can be neglected, compared to that introduced by dielectric loss and Johnson noise.

The spectral current density of dielectric loss noise can be estimated as:<sup>69, 70</sup>

$$i_d = \sqrt{4 \cdot k \cdot T \cdot \omega \cdot C \cdot \tan \delta} ; \quad (4.2)$$

where  $\omega$  the angular frequency, C the ME sensor capacitance, and  $\tan \delta$  the loss tangent of the piezoelectric layer. The spectral current density of Johnson noise, which comes from the thermal agitation of electrons in a conductor, can be estimated by Nyquist's relation:<sup>56</sup>

$$i_r = \sqrt{\frac{4 \cdot k \cdot T}{R}} = \sqrt{\frac{4 \cdot k \cdot T}{\rho \cdot \varepsilon}} C ; \quad (4.3)$$

where R is the resistance,  $\rho$  the volume resistance, and  $\varepsilon$  the dielectric constant.

Assuming that the dielectric loss and Johnson noises are uncorrelated, the total intrinsic spectral current noise density  $i_t$  can be obtained by

$$i_t(\omega) = \sqrt{i_d^2 + i_r^2} = \sqrt{4 \cdot k \cdot T \cdot C \left( \frac{1}{\rho \cdot \varepsilon} + \omega \tan \delta \right)} = A(\omega) \cdot \sqrt{C} ; \quad (4.4)$$

$$A(\omega) = \sqrt{4 \cdot k \cdot T \left( \frac{1}{\rho \cdot \varepsilon} + \omega \tan \delta \right)} .$$

If we assume that the noise gain of the detection circuitry is  $Z_n(j\omega)$  and that the noise bandwidth is  $f_H - f_L$  (where  $f_H$  and  $f_L$  are the upper and lower limits of the noise band), then the total output RMS voltage noise ( $E_{no}$ ) is

$$E_{no} = \left( \int_{f_L}^{f_H} i_t^2(\omega) |Z_n(j\omega)|^2 \right)^{0.5} = \sqrt{C} \cdot \left( \int_{f_L}^{f_H} A^2(\omega) |Z_n(j\omega)|^2 \right)^{0.5} = B(\omega) \cdot \sqrt{C} ; \quad (4.5)$$

$$B(\omega) = \left( \int_{f_L}^{f_H} A^2(\omega) |Z_n(j\omega)|^2 \right)^{0.5} .$$

From equation (4.5), we can see that  $E_{no}$  is proportional to  $\sqrt{C}$ . This suggests to minimize the total voltage noise that we simply need to decrease the capacitance of the sensor. However, this is slightly misleading, as we also need to have a large ME signal – it is the signal-to-noise ratio (SNR) that matters for high sensor sensitivity. The ME signal response to the applied magnetic field can be evaluated by the model we've introduced in Chapter 3 of this thesis, as illustrated in Fig.4-2.

Now, assume that the signal gain at a specific frequency  $\omega_0$  is  $G(\omega_0)$ . From the equivalent circuit in Fig.4-2, we can estimate the ME signal output voltage as  $V_o = j\omega_0\alpha_{me}H \cdot G(\omega_0)$ . The ME charge coefficient ( $\alpha_{me}$ ) can be obtained from the ME voltage coefficient ( $\alpha_{ME}$ ) as  $\alpha_{ME} = \frac{\alpha_{me}}{C \cdot t}$ , where  $t$  is the thickness of the piezoelectric layer (or the effective distance between the electrodes of the piezoelectric phase). So we can acquire the SNR at the specific frequency  $\omega_0$  as

$$\begin{aligned} SNR_{\omega_0} &= \frac{V_o}{E_{no}} = \frac{j\omega_0 H(\omega_0) \cdot G(\omega_0)}{B(\omega)} \cdot \sqrt{C} \cdot t \cdot \alpha_{ME} \\ &= \frac{j\omega_0 H(\omega_0) \cdot G(\omega_0)}{B(\omega)} \cdot \sqrt{\varepsilon \cdot V} \cdot \alpha_{ME}; \end{aligned} \quad (4.6)$$

where  $V$  is the volume of the piezoelectric phase. From equation (4.6), we can see that there are three parameters directly related to the ME laminate sensor's sensitivity. These are the dielectric constant  $\varepsilon$ , the volume  $V$ , and the ME voltage coefficient  $\alpha_{ME}$ . Highly sensitive ME laminate sensor design requires us to increase these three parameters as much as possible!

For a ME laminate sensor with a fixed mode and a fixed ratio of magnetostrictive and piezoelectric phases, the ME voltage coefficient  $\alpha_{ME}$  will remain constant no

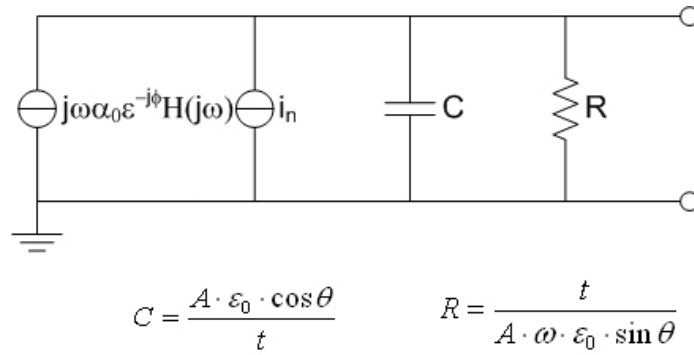


**Fig.4-2.** Equivalent circuit model for low frequency ME laminate sensor, including noise spectra considerations.

matter how large the total volume is.<sup>2, 37</sup> From (4.6), we can also see that if we keep the ME voltage coefficient unchanged while changing the total volume by a factor of  $m$ , then the SNR will be increased by a factor of  $\sqrt{m}$ . Here I designate this as the “SNR scale effect” or “Sensitivity scale effect”. This provides us insight into how to increase the ME sensitivity by increasing the volume.

To verify equation (4.6), we constructed a number of ME laminate sensors made from Tefenol-D/PZT that were operated in different coupled modes (unimorph, longitudinal-transverse or L-T, and push-pull or P-P), and that had different volumes of piezoelectric phase ( $V_{\text{piezo}}$ ). Table IV-I is a list that summarizes each of these ME sensors which were constructed including corresponding values of  $V_{\text{piezo}}$ ,  $C$ , and  $\alpha_{\text{ME}}$ . Measurements of the output noise and sensitivity limit were carried out by placing the ME laminates in a Helmholtz coil, and by applying a DC magnetic bias ( $H_{\text{dc}}$ ) and a small low frequency ac magnetic field ( $H_{\text{ac}}$ ) along the longitudinal direction of the laminates. To measure the output noise and sensitivity limit, a low noise low power charge amplifier detection circuit was constructed, which had a gain of  $\sim 1\text{V/pC}$  over the frequency range of 0.16 to 10Hz. The noise level of the amplifier was  $< 4\text{fA}_{\text{p-p}}$  referenced to the input, or  $< 4\text{mV}$  referenced to the output. The circuitry noise effect is much smaller than that of the sensors’, which guarantee that our measurement results are correct.

I next measured the output noise level ( $E_{\text{no}}$ ) from each of the sensors listed in Table IV-I, using this detection circuit. In Fig.4-3 (a), I plot  $E_{\text{no}}$  for the various sensors as a function of their respective values of  $\sqrt{C}$ . In this figure, one can see that there is

Table IV-I. ME laminate sensor.

No.	Material	Mode*	C (nF)	V <sub>eff</sub> (cm <sup>3</sup> )	α <sub>ME</sub> (V/cm.oe)
0	Terfermol-D/PZT-5	Unimorph	2.43	0.045	0.5
1	Terfermol-D/PZT-5	Unimorph	2.04	0.216	0.56
2	Terfermol-D/PZT-5	L-T	1.9	0.047	2
3	Terfermol-D/PZT-5	L-T	3.81	0.094	2
4	Terfermol-D/PZT-5	L-T	1.95	0.216	2.17
5	Terfermol-D/PZT-5	L-T	3.7	0.4	2.1
6	Terfermol-D/PZT-5	L-T P-P**	7.3	0.79	2.2

\* Longitudinal (L), Transverse (T), Push-pull (P-P)

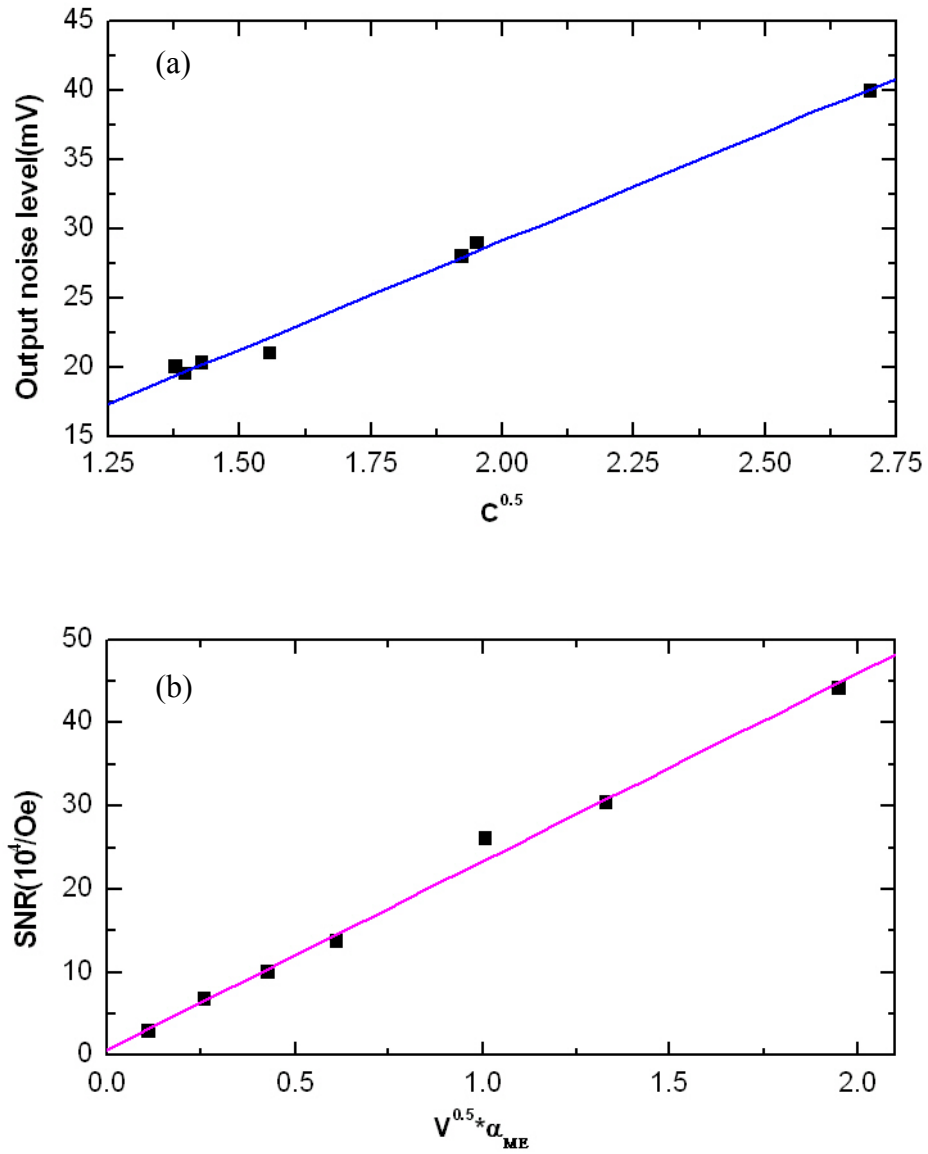


**Fig.4-3.** (a) Dependence of the output noise level ( $E_{no}$ ) on sensor capacitance ( $C$ ) for the various laminate composites given in Table IV-I; and (b) The signal-to-noise ratio (SNR) on  $\sqrt{V} \cdot \alpha_{ME}$ , where  $V$  is the volume of the piezoelectric phase and  $\alpha_{ME}$  is the magnetoelectric voltage coefficient; Each point corresponds to one of the ME laminate sensors enumerated in Table IV-I.

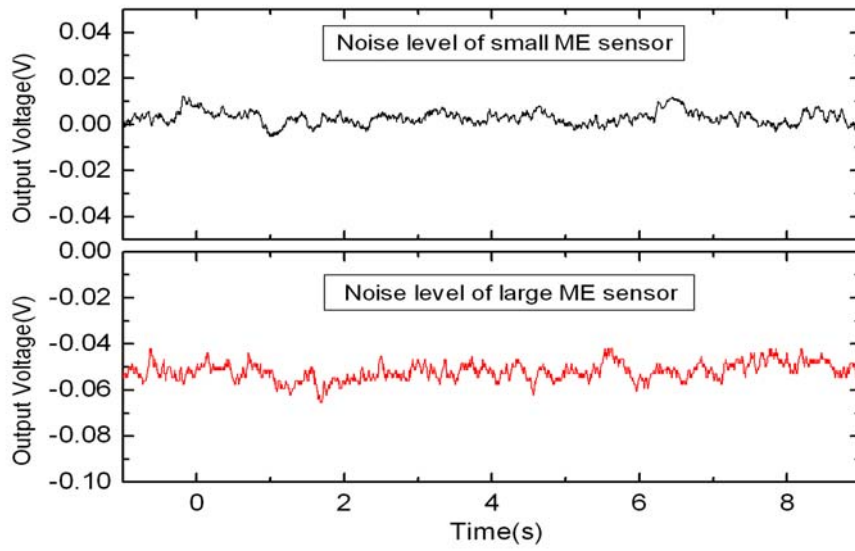
a near linear relationship between  $E_{no}$  and  $\sqrt{C}$ , as predicted above by eq. (4.5). In Fig.4-3(b), I show the SNR as a function of  $\sqrt{V}\alpha_{ME}$ , where a linear relationship can again be seen, consistent with the predictions of eq. (4.6). These results show (i) that the output noise level and SNR are nearly independent on the operational mode; (ii) that practically  $E_o$  is determined by the laminate capacitance; and (iii) that the SNR has a scale effect, where it can be increased simply by increasing the volume of the sensor.

As an example of this scale effect, the waveforms in real time of the output noise and lowest detectable magnetic field are shown in Fig.4-4. Data are shown for both small (No.1 in Table IV-I) and large (No.4) sensors in each figure part. The output noise level of the small ME sensor was  $\sim 20\text{mV}$ , while the large one was  $\sim 30\text{mV}$ . The lowest detectable magnetic field of the small ME sensor was about  $3\text{nT}$ , while the large one can achieve  $1\text{nT}$  magnetic field sensitivity. These results coincide well with our predictions of (4.5) and (4.6)

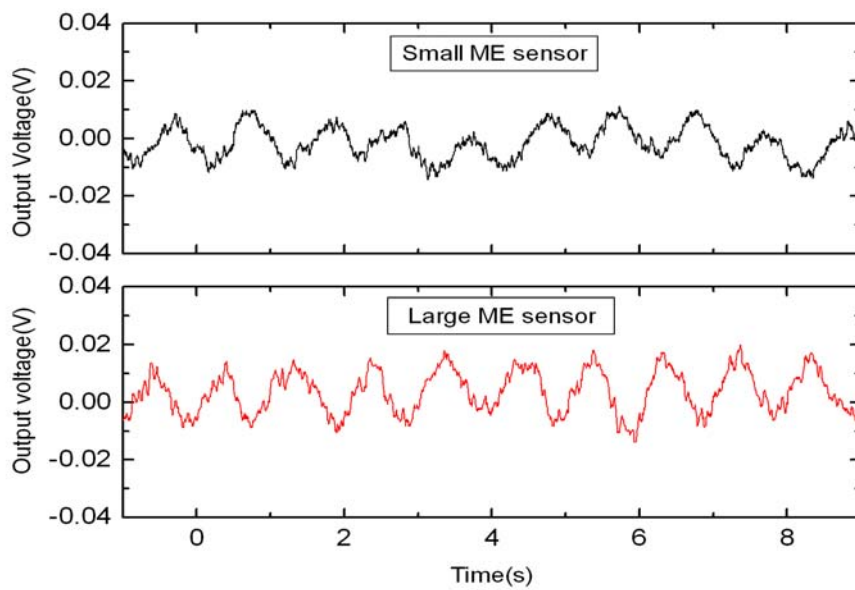
Finally, in Fig.4-5, I plot the lowest detectable magnetic signal as a function  $\frac{1}{\sqrt{V}} \cdot \alpha_{ME}$  for the various ME laminates. The linear trends in these results demonstrate that to detect smaller magnetic fields, one can either increase the sensor volume  $V$  or the value of ME voltage coefficient  $\alpha_{ME}$ .

#### 4.2.2 ME array to enhance sensitivity

Fig.4-2 provides a current source model for the ME laminate sensors. For convenience, some may prefer a voltage source model, and thus we can convert Fig.4-2 to Fig.4-6 by Thevinin's theorem. Using these models, we can predict the



(a)



(b)

**Fig.4-4.** (a) Waveforms in real time of the output noise level ( $E_{no}$ ) of a small LT mode ME laminate (sensor No.2 in Table IV-I) and of a large one (sensor No.5); and (b) The lowest magnetic field ( $f=1\text{Hz}$ ) detectable with a 95% confidence level. The small ME sensor had a sensitivity limit of  $\sim 3\text{nT}$ , whereas the large ME sensor of  $\sim 1\text{nT}$ .

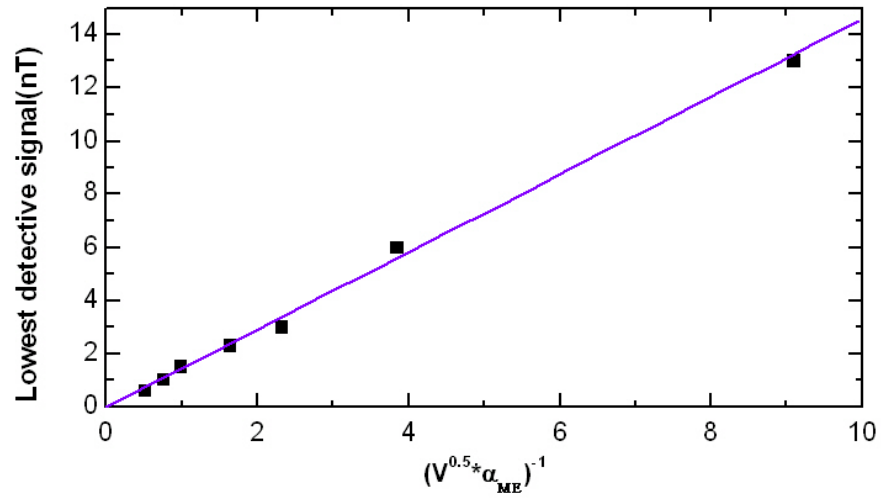
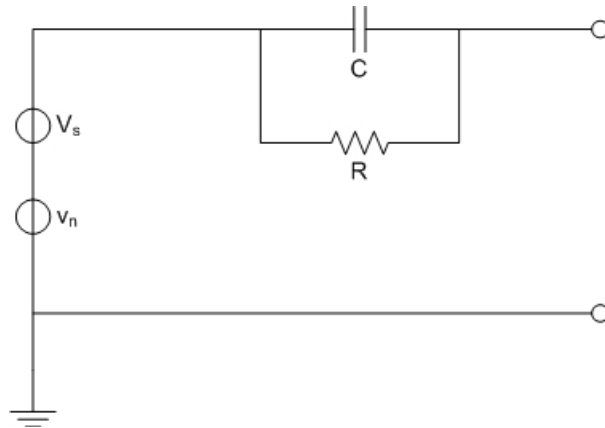


**Fig.4-5.** The lowest magnetic field signal ( $f=1\text{Hz}$ ) detectable with a 95% confidence level on

$$\frac{1}{\sqrt{V}} \cdot \alpha_{ME}$$



$$V_s = j\omega\alpha_0\varepsilon^{-j\phi}H(j\omega) \cdot \frac{R}{1+j\omega RC}, \quad v_n = i_n \cdot \frac{R}{1+j\omega RC}$$

**Fig.4-6.** Equivalent circuit model for the ME laminate sensor, including noise spectra considerations: voltage source model.

sensitivity of our detection unit (ME laminate + detection circuitry) as a function of frequency in the quasi-static range. The signal-to-noise (SNR) of the models in Fig.4-2 and Fig.4-6 can then be obtained as:

$$SNR = \frac{j\omega\alpha_0\varepsilon^{-j\phi}H(j\omega)}{i_n}. \quad (4.7)$$

Next, I extend this approach for “ME systems” to ME arrays. I predict the signal current level, noise current level, and signal-to-noise ratio (SNR) for both parallel and serial arrangements of ME units into arrays. I have also confirmed the predictions by experimental investigations.

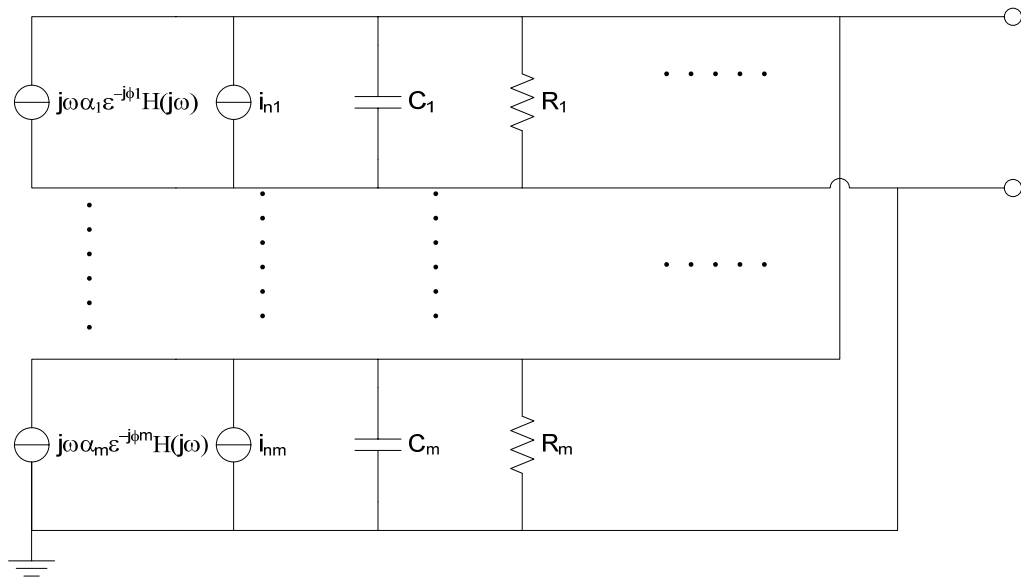
#### *ME array in parallel mode*

In this case, m number of ME sensor units are connected in parallel. The equivalent circuit model is shown in Fig.4-7(a).

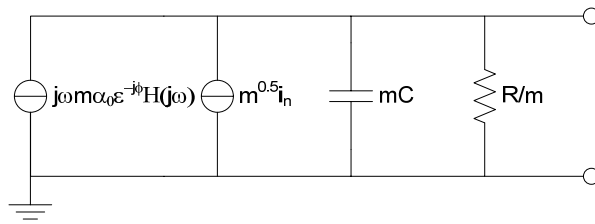
For simplification, we can assume that the signal response of all these ME units are harmonic to the applied magnetic field  $H(j\omega)$ : i.e., they have the same ME charge coefficients ( $\alpha_0e^{-j\phi}$  or  $\alpha_{me}$ ), impedance (R//C), and noise level ( $i_n$ ). When we apply a magnetic signal  $H(j\omega)$  to this ME sensor array, the response current signals add directly from each ME unit response, as follows:

$$I_{sP} = j\omega\alpha_1\varepsilon^{-j\phi_1}H(j\omega) + \dots + j\omega\alpha_m\varepsilon^{-j\phi_m}H(j\omega) = m \cdot j\omega\alpha_0\varepsilon^{-j\phi}H(j\omega). \quad (4.8)$$

However, because inherent noise is non-harmonic, the terms can not simply be added directly. Rather, the value of the total noise can only be evaluated by a root-square sum of all noise contributions. Assuming that all the noise sources are uncorrelated, we can estimate the RMS noise current as.<sup>51</sup>



(a)



(b)

**Fig.4-7.** (a) Equivalent circuit for the ME array in parallel model; and (b) the simplification.

$$i_{nP} = \sqrt{i_{n1}^2 + i_{n2}^2 \dots + i_{nm}^2} = \sqrt{m}i_n. \quad (4.9)$$

We can acquire the equivalent model for Fig. 4.7(b), from which we can determine that the SNR of the ME array in parallel as:

$$SNR_p = \sqrt{m} \frac{j\omega\alpha_0\varepsilon^{-j\phi}H(j\omega)}{i_n}. \quad (4.10)$$

From equations (4.8) and (4.9), we can find that the signal current increases by a factor of  $m$ , but that the noise current increases by  $\sqrt{m}$ . By comparing equations (4.7) and (4.10), we can also see that the SNR of the ME array in parallel increases by a factor of  $\sqrt{m}$ .

#### *ME array in serial mode*

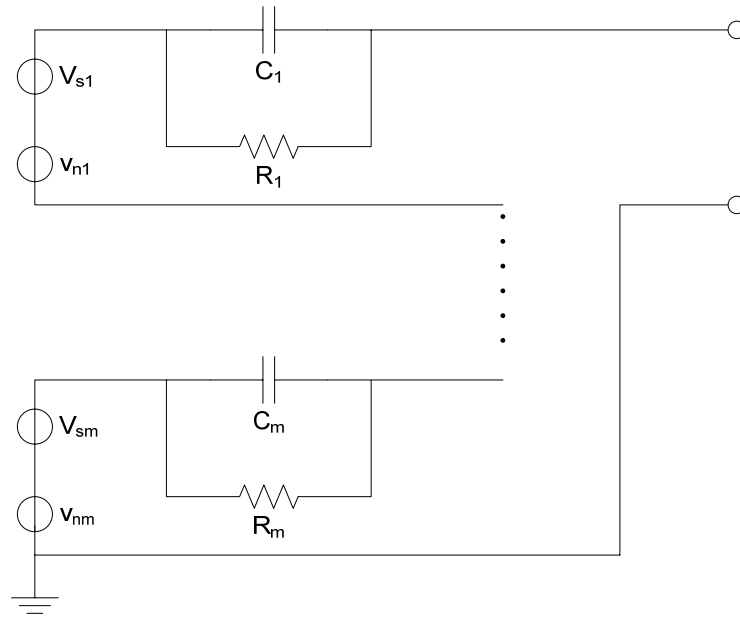
In this case,  $m$  number of ME sensor units were connected in serial. The equivalent model for this connection is shown in Fig.4-8(a). We used a voltage source approach here for convenience in the analysis.

For simplification, we assume that the signal response of all these ME units are harmonic to the applied magnetic field  $H(j\omega)$ : i.e., they have the same ME charge coefficients ( $\alpha_0 e^{-j\phi}$  or  $\alpha_{me}$ ), impedances ( $R/C$ ), and noise levels ( $i_n$ ). We can then find that the total voltage response to an applied magnetic field  $H(j\omega)$  is as follows:

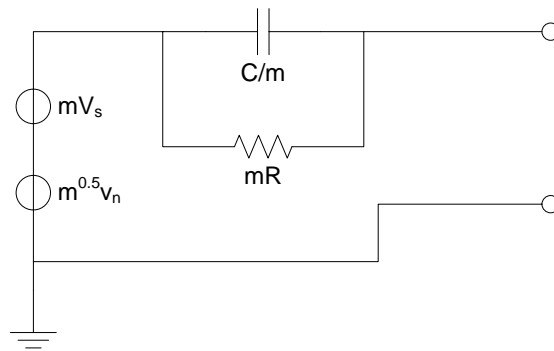
$$\begin{aligned} V_{sS} &= j\omega\alpha_1\varepsilon^{-j\phi_1}H(j\omega) \cdot \frac{R_1}{1+j\omega R_1 C_1} + \dots + j\omega\alpha_2\varepsilon^{-j\phi_2}H(j\omega) \cdot \frac{R_2}{1+j\omega R_2 C_2} \\ &= m \cdot j\omega\alpha_0\varepsilon^{-j\phi}H(j\omega) \cdot \frac{R}{1+j\omega RC} \end{aligned} \quad (4.11)$$

Again, the noise level must be calculated by a root-square sum, which results in:

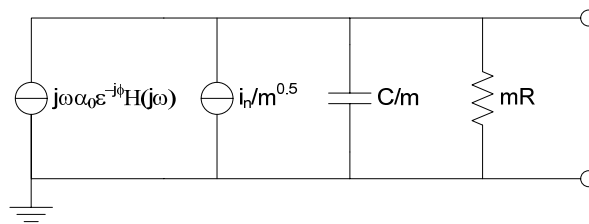
$$v_{nS} = \sqrt{v_{n1}^2 + \dots + v_{nm}^2} = \sqrt{m}i_n \cdot \frac{R}{1+j\omega RC}; \quad (4.12)$$



(a)



(b)



(c)

**Fig.4-8.** (a) Equivalent circuit for the ME array in serial model; (b) simplification of (a); and (c) equivalent circuit of (b).

We can acquire the voltage source model that is shown in Fig.4-8(b). For comparisons, we can convert this model into a current source one by the Norton theorem, as shown in Fig.4-8(c).

From the equivalent circuit of Fig.4-8(c), we can see that the current signal ( $I_{sS}$ ) and noise current level ( $i_{nS}$ ) are:

$$I_{sS} = j\omega\alpha_0\varepsilon^{-j\phi}H(j\omega) \quad (4.13)$$

$$i_{nS} = \frac{1}{\sqrt{m}}i_n \quad (4.14)$$

The SNR of the ME array in serial, then, is:

$$SNR_s = \sqrt{m} \frac{j\omega\alpha_0\varepsilon^{-j\phi}H(j\omega)}{i_n}. \quad (4.15)$$

From (4.13) and (4.14), we can see that the signal is unchanged by a serial arrangement of ME units into array, whereas the noise current is decrease by a factor of  $\sqrt{m}$ : thus, the SNR is increased by a factor of  $\sqrt{m}$ .

We next tested the predictions of (4.8) to (4.10) and (4.13) to (4.15). We constructed several Longitudinal-Transverse (L-T) ME laminate sensors, and arranged them in serial and parallel arrays. Each unit in the array was constructed from two pieces of Terfenol-D (size  $14 \times 6 \times 1.1 \text{mm}^3$ ) and one piece of PZT (size  $15 \times 6 \times 0.5 \text{mm}^3$ ). For signal (noise) amplification, we also designed a low noise ( $< 1 \text{fA}_{\text{rms}}$ ) low power consumption ( $\sim 10 \mu\text{W}$ ) charge amplifier with gain of  $\sim 1 \text{pC/V}$  over the frequency bandwidth of  $0.2 \text{Hz} \sim 10 \text{Hz}$ . The ME array and the prototype of the circuit are illustrated in Fig.4-9.

Care must be taken in construction and measurement: including excellent

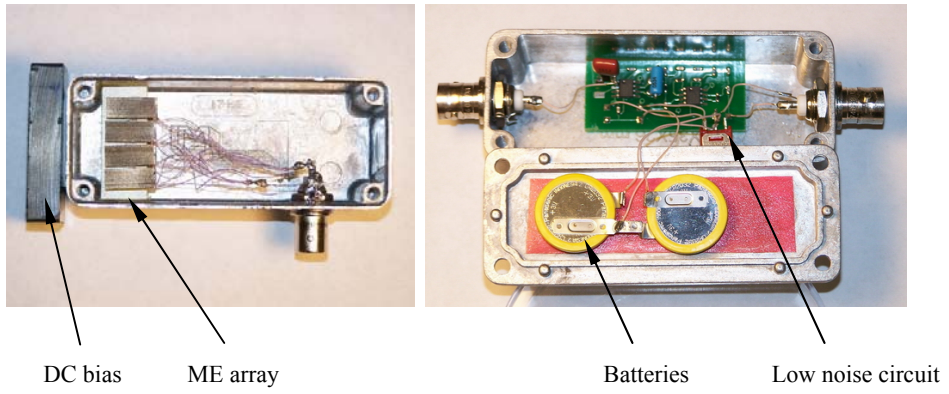


**Fig.4-9.** Prototype of the ME array and the low noise low power detection circuit.

grounding and shielding techniques, low humidity, stable environment temperature, and vibration noise isolation. The detection system was also kept under constant operation conditions for several hours before measurements were performed.

The output noise level, the ME charge response and the SNR are given in Fig.4-10 for the parallel array, and in Fig.4-11 for the serial one. From the data, we can see that the signal for the parallel mode increases linearly with the number of elements  $N$  in the array; whereas in serial arrangement, the signal is independent of  $N$ . In addition, we can see that the noise level increases by  $\sqrt{N}$  in the parallel mode, but decreases proportionally to  $\sqrt{N}$  for the serial mode. Because of these opposite trends in signal and noise, both the parallel and serial arrangements have the same net result effect on the SNR: which increased linearly with  $\sqrt{N}$ . These findings confirmed the predictions of (4.10) and (4.15), above.

Finally, we determined the lowest detectable signal for a ME array consisting of eight pieces of L-T units, and compared the results to a corresponding one for a single sensor unit. In Fig.4-12, we can see that a single LT unit can only detect a magnetic field change of 3nT at 1Hz, whereas the ME array could detect a signal as low as 1nT at 1Hz. These results, again, confirm our prediction for the SNR enhancement by array constructions.

The noise spectrum of the ME array constructed by LT ME unit for serial and parallel modes was also carried out. To measurement the noise spectrum, we need to amplify the noise before it is fed into the spectrum analyzer. I connected the sensor output to a low noise current amplifier Keithley 425 with a low noise cable and then

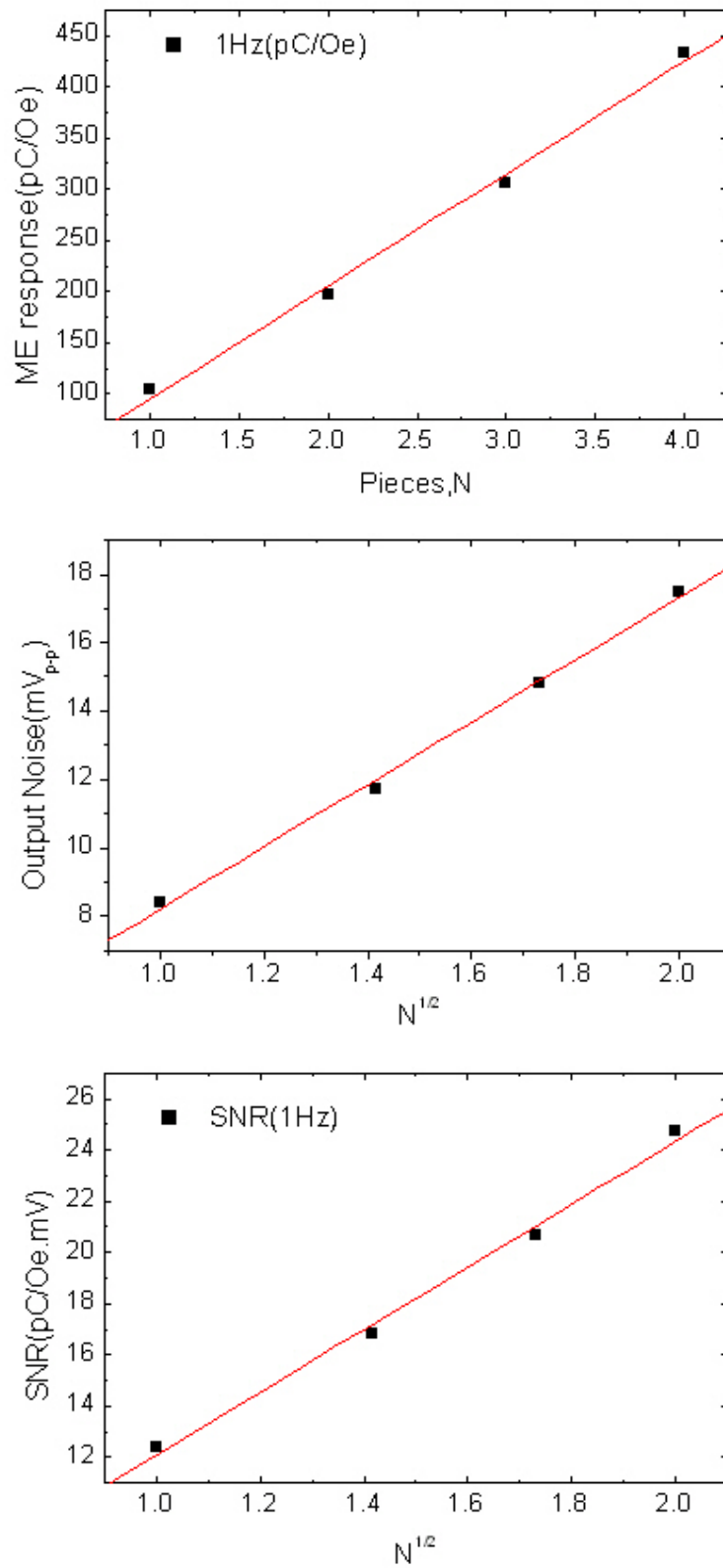


**Fig.4-10.** Signal response, noise level and SNR for parallel mode ME array.

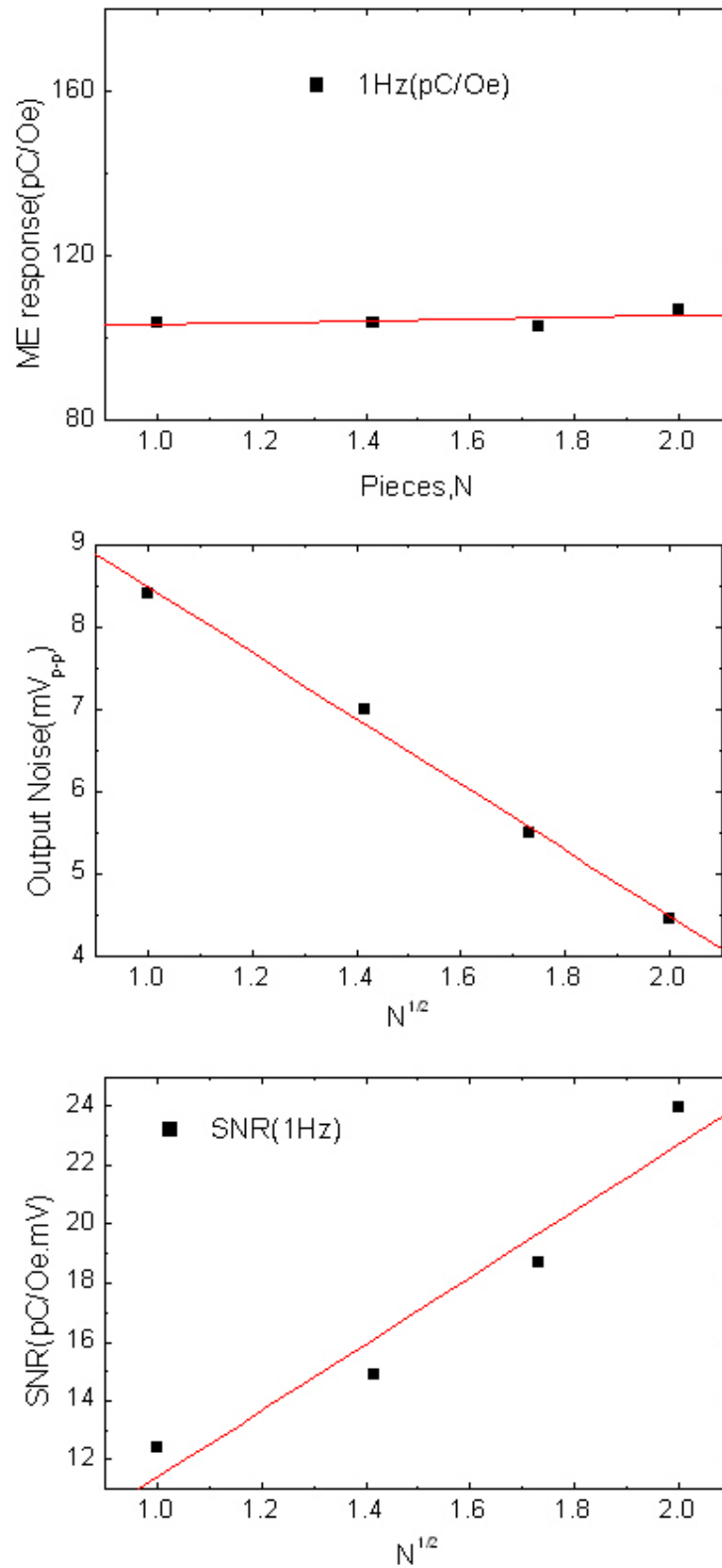


**Fig.4-11.** Signal response, noise level and SNR for serial mode ME array.

feed the amplifier's output to a Dynamic signal analyzer SR785. Experimental result was illustrated in Fig.4-13, where "P" and "S" denote parallel and serial mode, separately. From the spectrum measurement result, we can see that the noise spectrum of P4 (parallel 4 pieces of LT ME units) is greater than P3, and the noise spectrum of these sample follow the sequence as following: **P4 > P3 > P2 > 1 > S2 > S3 > S1**. This result again confirms our previous noise prediction.

### **4.3 ME sensitivity optimization on considering external noise**

In the previous section, we proposed a ME sensor design optimization methods on considering internal noise. However, practical sensor applications are also always notably affected by environmental or external noise sources, such as thermal fluctuation and mechanical vibration. These external noises will be dominating factors that affect the sensor's sensitivity in practical applications.

In Chapter 1, I introduced the fundamental external noise sources. For ME sensors, the dominant ones are the thermal fluctuation and mechanical vibration sources. Thermal fluctuation noise is pyroelectric in origin, where the spontaneous polarization of the piezoelectric phase is temperature dependent, resulting in a dielectric displacement current in response to temperature changes; whereas the vibrational noise is piezoelectric in origin, where the spontaneous polarization is coupled to pressure and stress changes, via piezoelectricity. As for all magnetic field sensors, it is important that ME sensors be designed by such a means that optimizes its abilities to cancel these external noise.

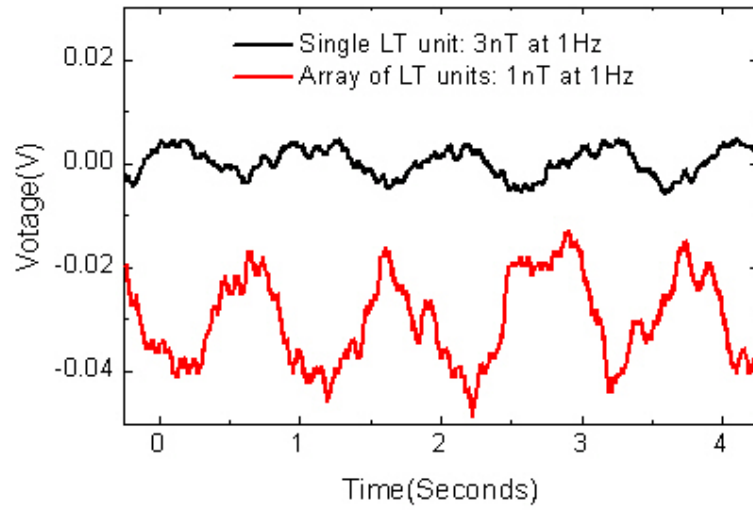


**Fig.4-12.** Waveforms in real time for a L-T ME unit corresponding to 3nT, and L-T ME array corresponding to 1nT sinusoid magnetic signal at 1Hz.

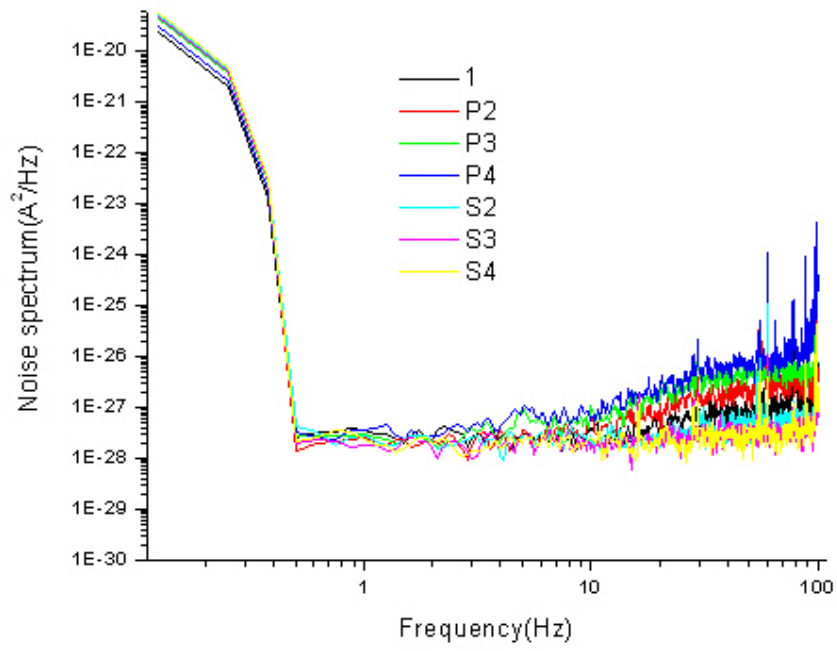


**Fig.4-13.** Noise spectrum of the ME array in serial and parallel mode.

Here, we consider the ability of various ME modes to cancel environmental noise from thermal and vibrational sources. The findings are summarized in Table IV-II, where it can be seen that there are various configurations that have the internal abilities to reject thermal or vibrational noise. The results provide insights into how future ME laminates configurations might be arranged in order to provide enhanced signal-to-noise ratios.

#### **4.3.1 External noise on ME sensors**

To understand how the external noise affects the ME sensors, we first need to know the deformation of the ME sensors under external noises. These effects can be described as follows:

##### *Vibration:*

Let us assume a rectangular ME laminate sensor, as shown in Fig.4-14(a). Stray vibrations will excite various vibrational modes, but the dominant one will be the fundamental bending mode. It has the lowest resonance frequency, and thus will couple best to the environmental vibrational noise which is also generally of low frequencies. For simplicity, we consider here that vibration noise excites only this bending mode.

In Fig.4-14(b), we illustrate the fundamental bending mode for a rectangular ME sensor. Please note that there is a neutral surface, which ideally has no shear force exerted on it. The area of the rectangle that is below this neutral surface is in compression, whereas that above it is in tension. If we measure the piezoelectrically

*Table IV-II. ME laminate sensor.*

Mode	Vibration Cancellation	Thermal Cancellation
Unimorph	No	No
Bimorph	Partially	Partially
L-T, T-T	Yes	No
L-L, T-L	Yes	No
Push-Pull	Yes	No
Multi-Push-Pull	Yes	No
SS-UN	Yes	No
US-SN	No	Yes

\* SS-UN: Symmetrical-signal, unsymmetrical noise.

\*\* US-SN: Unsymmetrical-signal, symmetrical noise.

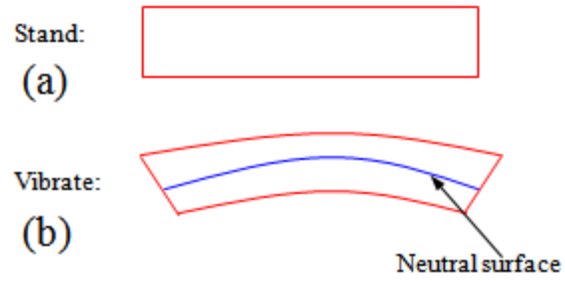


**Fig.4-14.** (a) A force free rectangular plate, and (b) influence of vibrations on the shape deformation of the rectangular plate.

induced charge both above and below the neutral line, we would find that they are of opposite signs but nearly of the same magnitude. This figure conceptually demonstrates that vibrational noise sources can be cancelled, if the structure of the sensor is design to be symmetrical.

#### *Temperature fluctuation*

Temperature is a scalar property. The four basic ME modes and the push-pull mode illustrated in Fig.1-3 and Fig.1-5 have symmetric structures. When the temperature of a symmetrical rectangle is changed, thermal expansion will strain it by the same percent in the same directions, as shown in Fig.4-15(a). In this case, only longitudinal / transverse deformations will be excited.

However, the more complex ME laminate configurations, such as unimorph and bimorph structure, are nonsymmetric. Thus, when the temperature changes, both bending and longitudinal modes will be excited due to thermal expansion differences between the various layers, as illustrated in Fig.4-15(b). Again, there is a neutral surface for the induced bending mode. Charges induced from this temperature change from above and below the neutral line are of opposite sign but nearly same magnitude. This figure conceptually demonstrates that thermal noise can be partially cancelled by the sensor itself, using an unsymmetrical structure.

#### **4.3.2. Analysis of external noise in different modes of ME laminates.**

In this part, we will analyze how will the external noise (vibration, thermal fluctuation) affects ME sensors in different modes, including unimorph, bimorph, L-T,

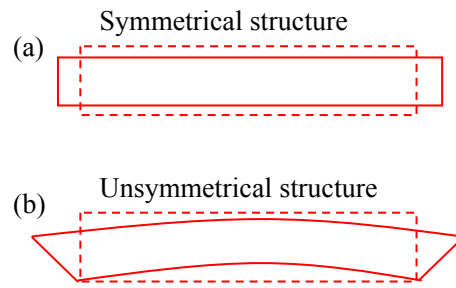


**Fig.4-15.** External thermal noise on the plate in a (a) symmetrical structure; (b) unsymmetrical structure.

T-T, L-L, T-L, Push-pull, Multi-push-pull. And we will also introduce two new modes which are designated as unsymmetrical signal-symmetrical noise (US-SN) mode and symmetrical signal-unsymmetrical noise (SS-UN) mode. How will the external noise affect ME sensors in these two new modes will be discussed.

### *Unimorph*

A unimorph is an unsymmetrical structure.<sup>42</sup> Its ME signal will contain both expanding and bending mode contributions. In this case, vibrational bending noise and the signal bending mode will be mixed – we will be unable to separate them. Accordingly, a unimorph ME laminate will not have vibration noise cancellation ability. In a similar manner, external thermal noise does not cancel for a unimorph structure, again simply because the signal and noise modes are mixed. Fig.4-16 illustrates the output charge induced across the piezoelectric layer due to stray vibrations and temperature fluctuation.

### *Bimorph*

A bimorph is also an unsymmetrical structure.<sup>43</sup> The ME signal will again produce both bending and expanding mode contributions. In this case, the expanding mode signal output will cancel due to the structure's design, and consequently only the bending signal mode output will remain. This bending mode signal is analyzed in Fig.4-17(a). It has a differential structure, which will result in a partial cancellation of the noise introduced by the vibration.

External thermal noise will excite both expanding and bending modes in a bimorph.

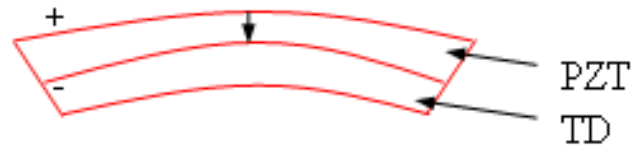


**Fig.4-16.** Effect of vibrational and thermal noise on a unimorph.

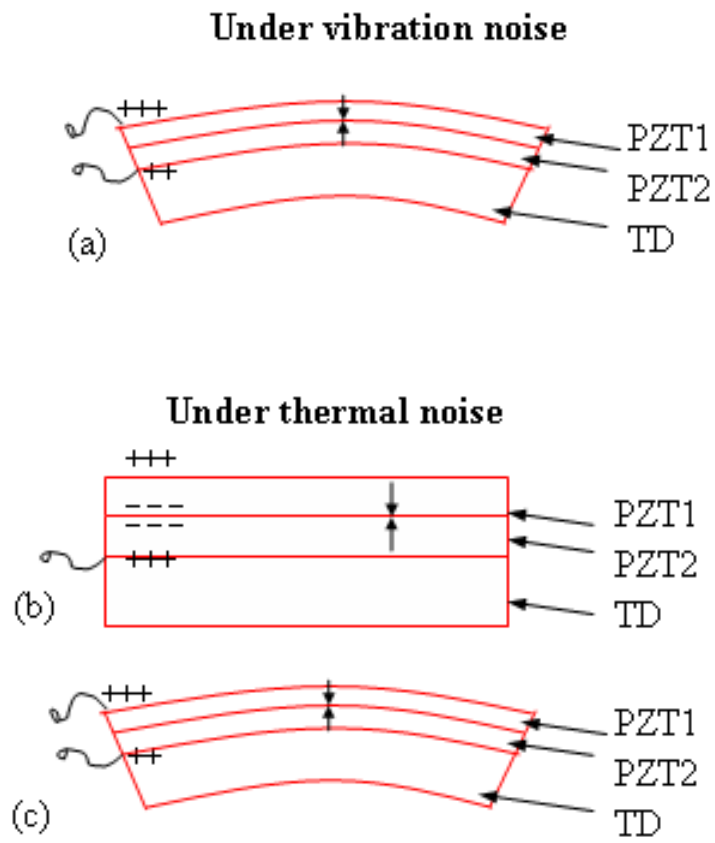


**Fig.4-17.** Effect of environmental noise on bimorph ME laminate (a) vibrational noise which excites bending mode; (b) thermal noise which excites a longitudinal mode; and (c) thermal noise which excites a bending mode.

Analysis of the noise introduced by thermal changes is given in Fig.4-17(b) for the expanding mode and in (c) for the bending one. We can see in Fig.4-17(b) that thermal noise is fully cancelled in the expanding mode, but in 4-17(c) that it is only partially cancelled in the bending mode.

The combinations of Fig.4-17(a) to (c) demonstrate that the bimorph ME structure has the ability to partially cancel both external vibrational and thermal noise. However, unfortunately, at the same time, this cancellation will also reduce the ME signal. The farther the distance of the two PZT layers from the neutral surface, the smaller the remaining signal will be. Accordingly, practical designs must consider both the noise cancellation and signal loss.

#### *L-T, T-T*

The L-T and T-T configurations have a symmetrical structure. For this configuration,<sup>40</sup> a ME signal is produced only in the expanding mode, whereas vibrational noise is introduced through the bending mode. This configuration has a built-in ability to cancel vibrations in the bending mode. As shown in Fig.4-18(a) (due to the L-T, T-T structure's symmetric nature, only the PZT portion of the ME laminate is shown), the sign of the induced charges are reversed on going from above to below the neutral line. Accordingly, the net output from vibrational noise is rejected.

Due to the symmetric nature of the L-T, T-T configuration, a bending mode will not be excited by thermal changes. Rather, thermal noise will be constrained to the expanding mode. This makes it impossible to separate the thermal noise from the ME signal by the sensor itself.

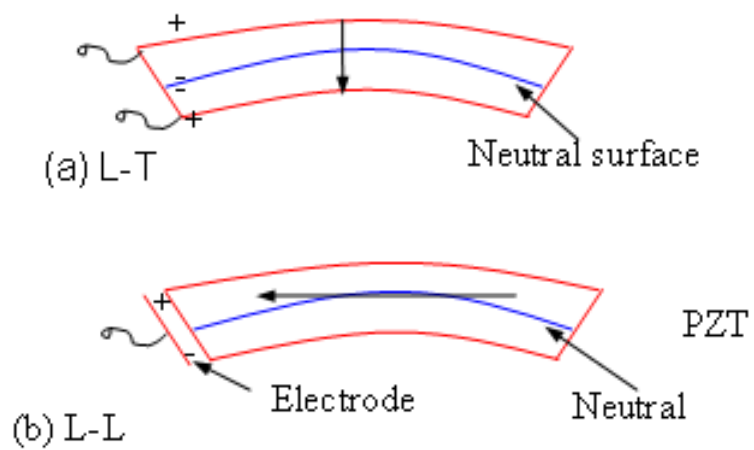


**Fig.4-18.** Effect of vibration bending noise on the PZT layer in (a) L-T, T-T modes ME laminate; and (b) L-L, T-L modes ME laminate.

### *L-L, T-L*

The L-L and T-L configurations also have a symmetrical structure.<sup>40</sup> Again, the ME signal is produced only in the expanding mode. Only vibrational noise, and not thermal, can excite a bending mode which can be separated from the expanding mode excited by the ME signal. Analysis of the vibrational noise is illustrated in Fig.4-18(b). Again, there is a neutral surface, above which there is a positive charge and below which there is a negative one: expanding noise is cancelled out. However, because thermal noise is constrained to the expanding mode with the ME signal, it can not be rejected without canceling the signal.

### *Push-Pull: single unit*

Both the L-L and L-T push-pull configurations are symmetrical structures,<sup>41</sup> where thermal noise again can not excite a bending mode. These configurations are shown in Fig.4-19 (a) and (b), respectively. In both of these push-pull modes, vibration noise is contained in the bending mode, whereas thermal noise is in the expanding. Both structures have a built-in vibration cancellation: as illustrated in the insets of the figures, where we can see that the output will be zero for bending noise.

### *Push-pull: multi unit*

A modification of the L-L push-pull mode has been studied in magnetostrictive / (1-3) piezo-fiber composites, where the piezo-fibers are poled in a manner such as to create numerous push-pull units back to back.<sup>36</sup> The poling condition of the piezo-fiber layer is illustrated in Fig.4-19(c). This multi push-pull structure also has

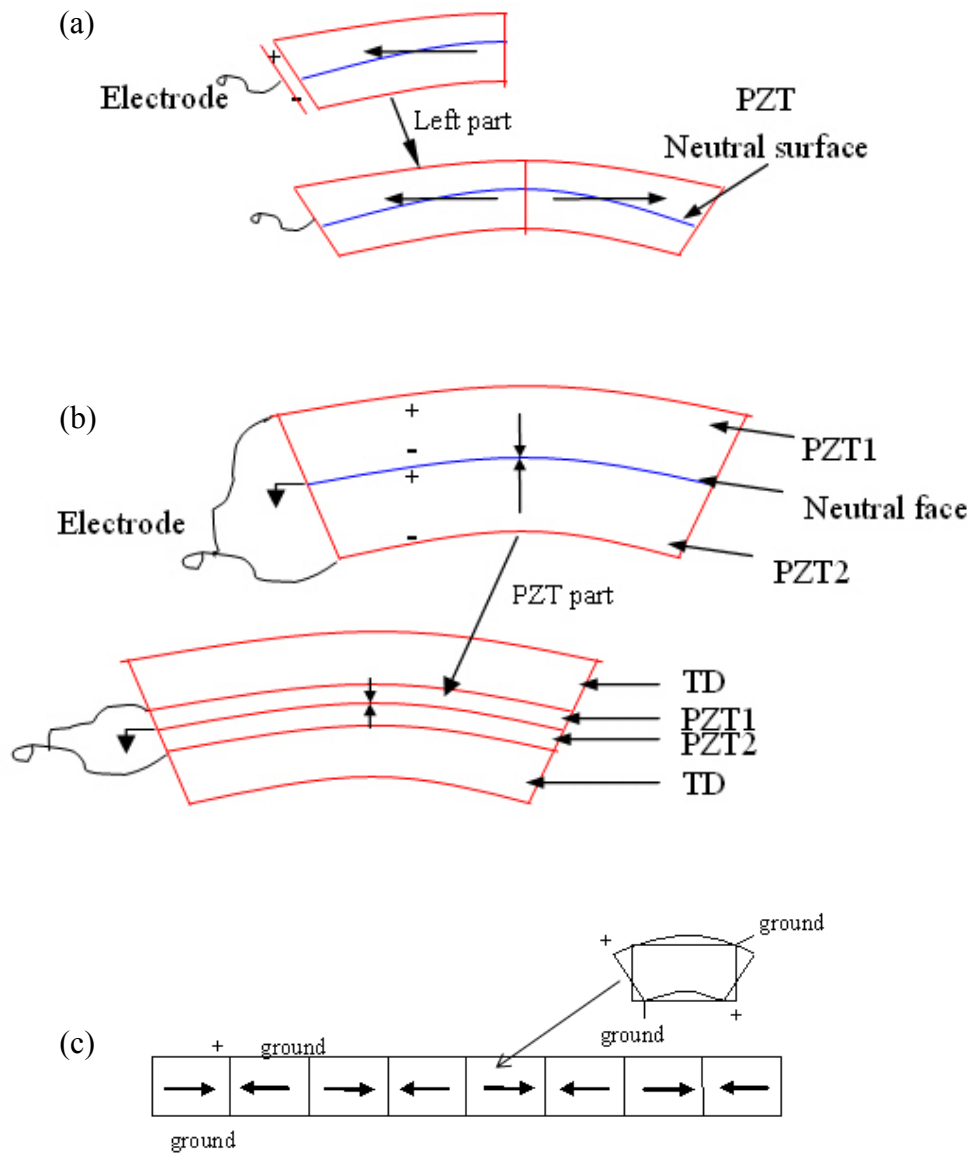


**Fig.4-19.** Vibration bending noise in (a) the L-L push-pull structure; (b) the L-T push-pull structure, where the inset shows the cancelation of vibration effects; (c) in a multi push-pull configuration, each individual push-pull unit works in the L-L mode.

the ability to cancel vibration noise, as shown in the inset of the figure. The advantage of this configuration is the higher geometric capacitance of the piezo-fiber layer, over that of a single monolithic one.

#### *Symmetrical Signal, unsymmetrical noise mode*

A symmetrical signal, unsymmetrical noise mode, (i.e., a SS-UN mode), is a ME construction that is designed to have mechanically symmetric responses to an applied signal, while having unsymmetrical responses to external noise. Following this designation, we can see that L-T, T-T, L-L, T-L, push-pull modes all fall in this category. More accurately, we should note that these modes are only unsymmetrical to vibration noise, and not to thermal fluctuation. From our above analysis, it can be noted that thermal noise in a symmetrical structure can only excite symmetrical deformation: i.e., the SS-UN mode can not separate the thermal noise from the signal “itself”. So for this mode design, when the temperature fluctuation is a problem, a high pass filter is required in the detection circuitry since temperature fluctuation is always a low frequency noise. Our previously research used this method to reduce the temperature’s affect and stabilized the ME unit output.

#### *Unsymmetrical Signal, Symmetrical noise mode*

An unsymmetrical signal, symmetrical noise mode, (i.e. a US-SN mode), is a design where the sensor has mechanically unsymmetrical responses to an applied signal, while having symmetrical responses to external noise. An unsymmetrical signal configuration can be designed by introducing a non-magnetic material, which

has the same elastic stiffness and temperature coefficient as that of the magnetic layer(s). In this case, the magnitude of the signal will be decreased some, but will have advantages with regards to thermal noise cancellation. We illustrate this concept by the following two designs.

US-SN configuration 1 is illustrated in Fig.4-20(a). It is a three layer structure consisting of a bimorph piezoelectric layer sandwiched between magnetostrictive and nonmagnetic layers. Analysis of the charges across the piezoelectric layer induced from bending is shown in Fig.4-20(b). We can see that this configuration does not cancel vibration noise. Analysis of the charges induced across the piezoelectric layer by thermal changes is shown in Fig.4-20(c). Assuming that the non-magnetic and magnetostrictive layers have the same elastic stiffness and temperature coefficient thereof, we can see that the charge outputs cancel. Thus, the thermal noise is rejected.

US-SN configuration 2 is illustrated in Fig.4-21(a). It is a four layer structure consisting of two piezoelectric layers poled in the same direction sandwiched between magnetostrictive and nonmagnetic layers. However, the top electrode of PZT 1 and the bottom electrode of PZT 2 are connected as electrode 1, whereas the bottom electrode of PZT 1 and the top electrode of PZT 2 are connected as electrode 2. Analysis of the charges across the piezoelectric layer induced from this bending is shown in Fig.4-21(b). We can see that this configuration does not cancel vibration noise. Analysis of the charges induced across the piezoelectric layer by thermal changes is shown in Fig.4-21(c). Assuming that the non-magnetic and magnetostrictive layers have the same elastic stiffness and temperature coefficient

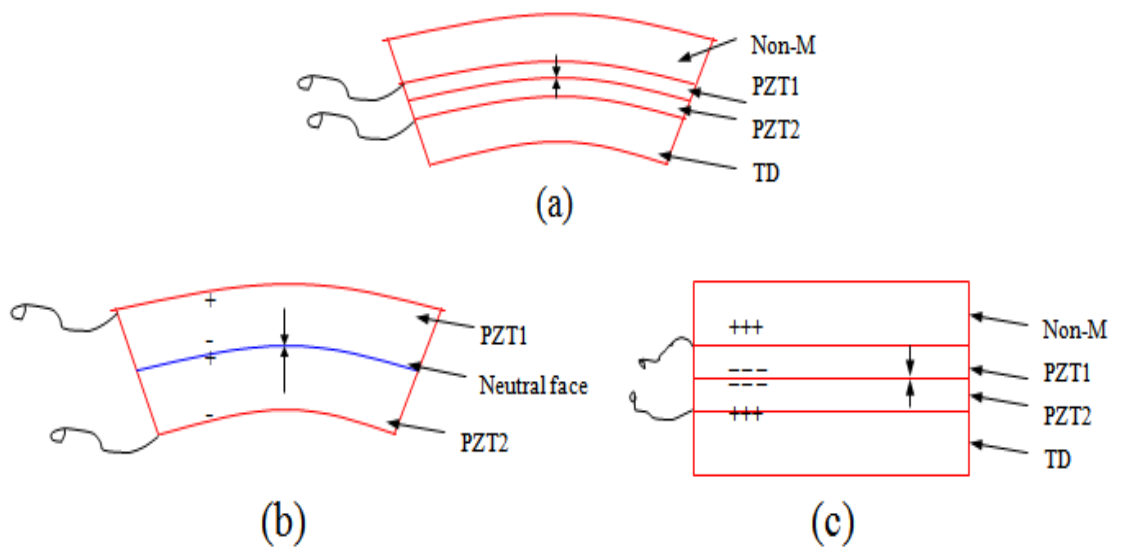


**Fig.4-20.** Bending on US-SN structure 1 (a); and noise analysis of piezoelectric layer for the structure 1: (b) vibration bending noise, and (c) thermal noise.

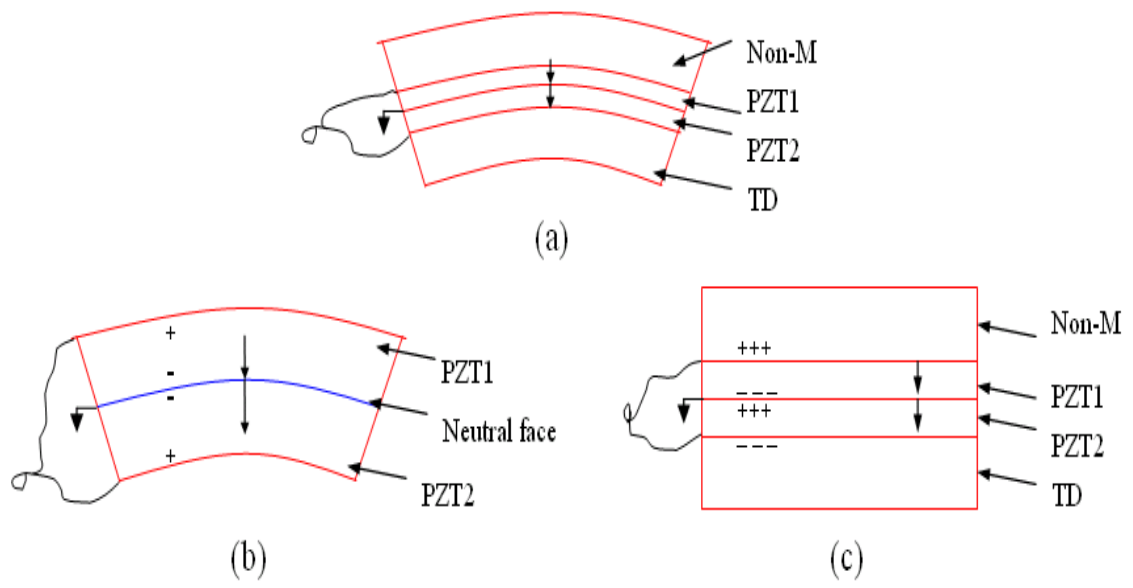


**Fig.4-21.** Bending on US-SN structure 2 (a); and noise analysis of piezoelectric layer for the structure 2: (b) vibration bending noise, and (c) thermal noise.

thereof, we can see that the charge outputs cancel. Thus, the thermal noise is rejected.

An unsymmetrical signal configuration could also be designed by making use of the piezomagnetic properties of the magnetostrictive layer. Previous researches have shown that giant magnetostrictive materials (Terfenol-D, Metglass) require a DC bias to achieve a high effective piezomagnetic condition, whereas the magnetization direction is determined by the sign of the applied DC bias. If two magnetostrictive layers are magnetized in opposing directions, then accordingly their ME response will be opposite to each other. If we replace the non-magnetostrictive layer in Fig.4-20 (or Fig.4-21) with a magnetostrictive one while making its magnetization direction opposite to the first, then the signal will be unsymmetrical, whereas the thermal noise response is symmetrically. This structure has been investigated as shown in Fig.4-22 and showed good resist to the temperature fluctuation.<sup>72</sup>

Comparing to Fig.4-20, this structure will have a higher ME performance due to the top and the bottom magnetostrictive phase will both contribute for ME coupling.

#### **4.3.3. Investigations of vibrational noise rejection.**

Investigations of vibrational noise were performed for various ME sensors. The experiment for vibration damping is illustrated in Fig.4-23. The ME sensor was put on a small table above a shaker which was driven by a bipolar power amplifier (HP6826A). A frequency dependent source signal, which was provided by a lock-in amplifier (SR850), was fed into the HP6826A for amplification. The output signal was then measured by the SR850 Lock-in amplifier. The ME laminate composites we characterized are listed in Table IV-III, along with their corresponding sizes.

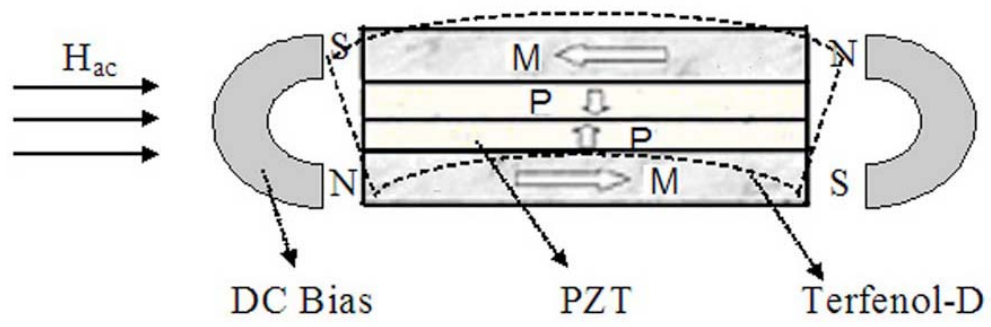


**Fig.4-22.** US-SN mode 3

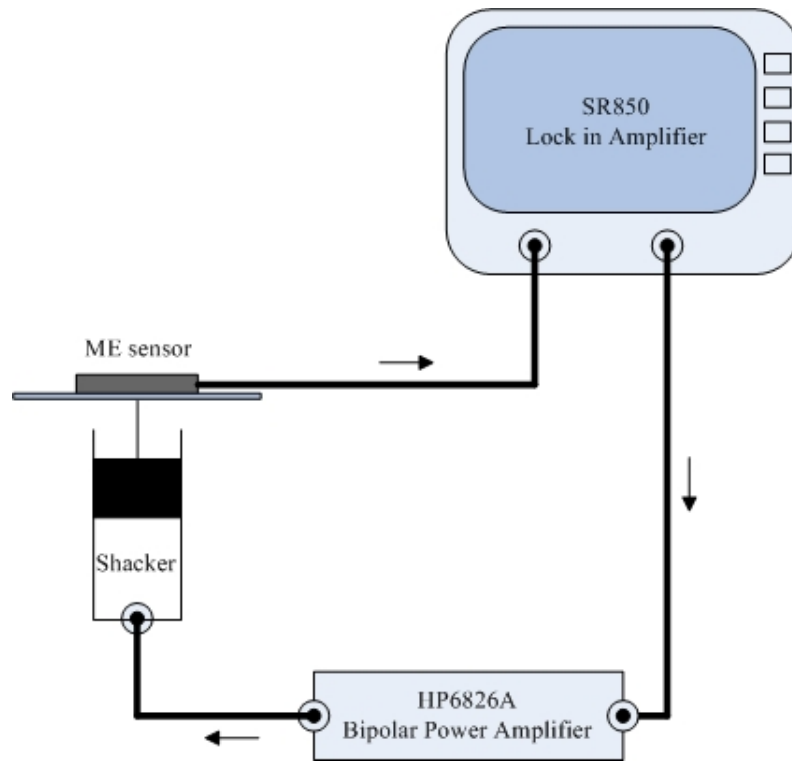


**Fig.4-23.** vibrating damping experiment setup for ME laminate sensor.

Table IV-III. ME laminate sensor.

Mode and No.	Each TD Size L× W× H (mm <sup>3</sup> )	Each PZT Size L× W× H (mm <sup>3</sup> )	Total Size L× W× H (mm <sup>3</sup> )
Unimorph 1	14×6×1.2	15×6×1.0	15×6×2.2
Unimorph 2	14×6×2.4	15×6×1.0	15×6×3.4
Bimorph 1	14×6×1.2	15×6×0.5	15×6×2.2
Bimorph 2	14×6×2.4	15×6×0.5	15×6×3.4
LT 1	14×6×0.6	15×6×1.0	15×6×2.2
LT 2	14×6×1.2	15×6×1.0	15×6×3.4
LT-PP 1*	14×6×0.6	15×6×1.0	15×6×2.2
LT-PP 2*	14×6×1.2	15×6×1.0	15×6×3.4

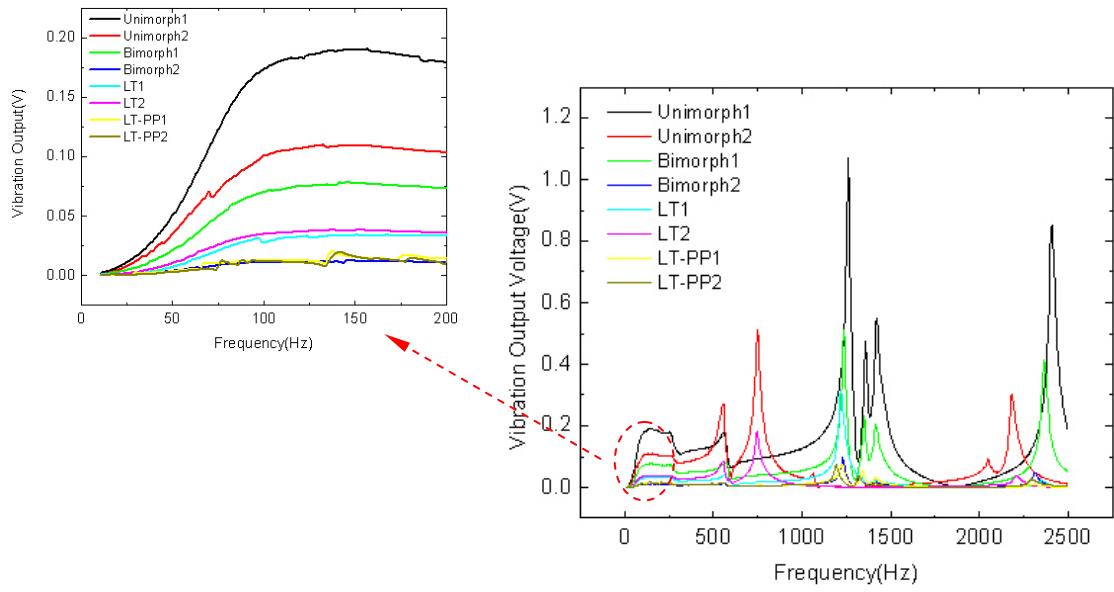
\* LT-PP: LT-Push-pull mode

The vibration frequency dependence for these ME laminate sensors are shown in Fig.4-24(a). We amplify the low frequency portion of the spectrum to better illustrate vibration noise rejection. In the figure inset, we can see that L-T and LT-push-pull modes have the best vibration cancellation performance while the bimorph has some capabilities in this regard; whereas the unimorph has nearly none. These figures are consistent with the prediction in Section 4.3.1.

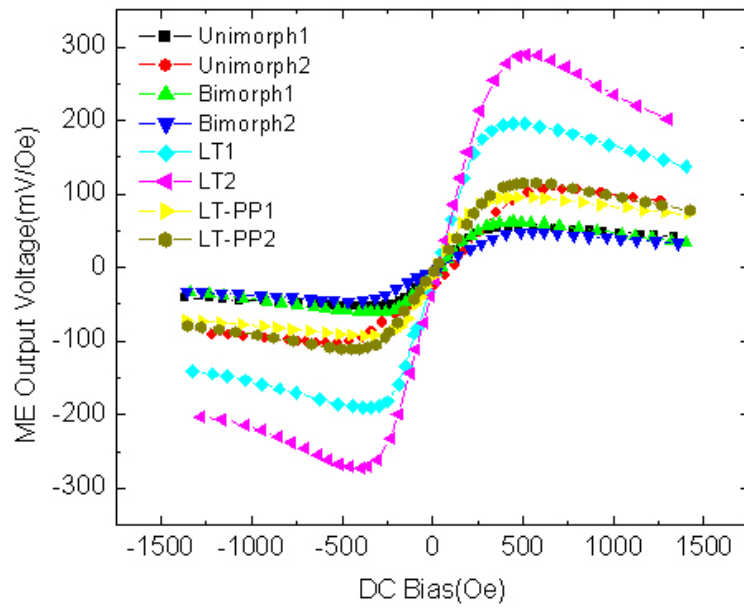
I Next measured the ME voltage coefficient of these various ME laminate configurations of Table IV-III at different DC bias. The results are shown in Fig.4-24(b). One can see from this figure that the L-T mode has the highest ME induced voltage, compared to the bimorph and unimorph modes. At the optimized DC bias for each of these ME sensors, I finally calculated the SNR, as shown in Fig.4-25. We can see that the L-T and LT-PP modes have the highest value of SNR, while the bimorph is intermediate, whereas the unimorph has the lowest. Again, these results are consistent with our prediction in section 4.3.1.

#### **4.4. Low resonant frequency Giant ME effect**

Here, I will show by incorporating a relatively high- $Q_m$  elastic steel (third-phase) layer in magnetostrictive/piezoelectric laminates that (i) the resonance frequency can be notably decreased without increasing the size of Terfenol-D, while (ii) the resonance enhancement of the ME effect is significantly increased. My concept for a Terfenol-D/elastic-steel/PZT (or TSP) ME laminate is illustrated in Fig.4-26 (a). For comparisons, part (b) of this figure illustrates a Terfenol-D/PZT (or TP)



(a)



(b)

**Fig.4-24.** (a) Vibrating damping experimental result for different ME sensor; (b) ME voltage for different ME sensor.

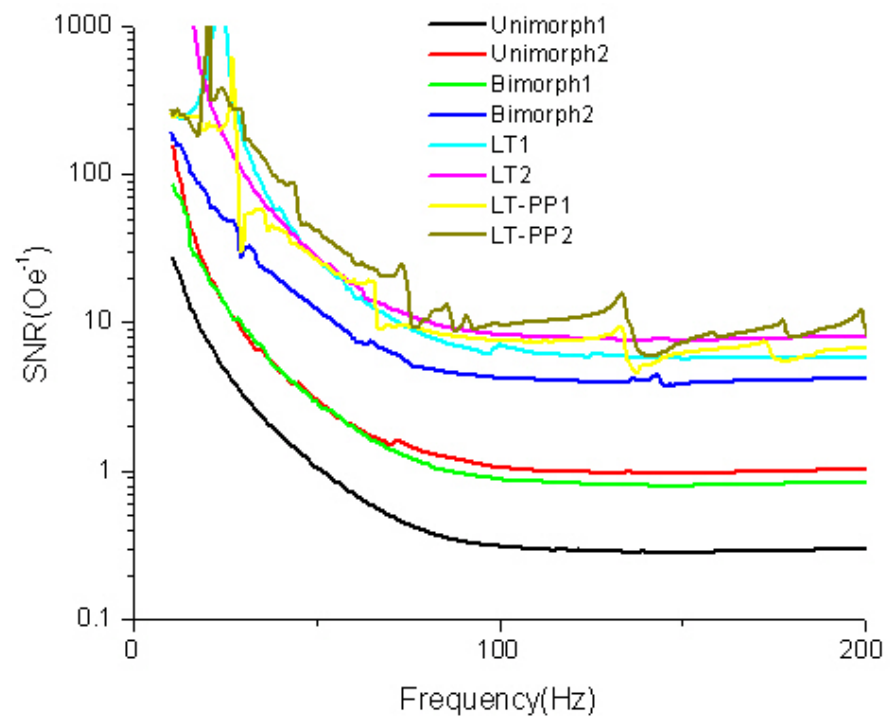


**Fig.4-25.** SNR for different ME sensor.

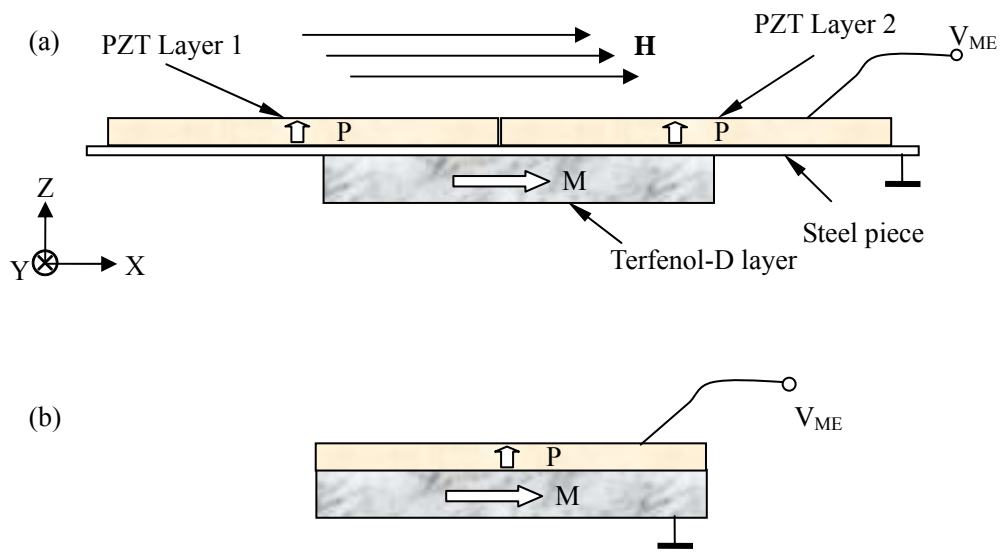


**Fig.4-26.** Illustration of ME laminate configurations (a) Terfenol-D/Steel/PZT three-phase bending-mode unimorph; and (b) Terfenol-D/PZT unimorph.

unimorph-type construction. The sizes of the Terfenol-D, PZT (APC-850), and steel layers in Fig.4-26(a) are  $14 \times 6 \times 1.1 \text{mm}^3$ ,  $15 \times 6 \times 0.5 \text{mm}^3$  and  $32 \times 6 \times 0.09 \text{mm}^3$ , respectively. These layers were bonded together using an epoxy. The magnetization ( $\mathbf{M}$ ) of the magnetostrictive Terfenol-D layer was oriented along the longitudinal (or X-axis) direction, and that of the polarization ( $\mathbf{P}$ ) of the piezoelectric PZT ones were along the thickness (or Z-axis) direction. Because the Terfenol-D layer was asymmetrically bonded to one side of the elastic-steel layer (see Fig.4-26a), a low-frequency bending moment was produced in response to an applied magnetic field  $\mathbf{H}$  that was //X.

The 1<sup>st</sup> bending-mode resonance frequency is much lower than that of the fundamental longitudinal mode. We may suppose that the ME laminate is a free-free bar, and its bending mode resonant frequency is<sup>42, 73</sup>

$$f_n = \frac{\pi \cdot d}{4\sqrt{3} \cdot l^2} \sqrt{\frac{1}{\bar{\rho} \cdot \bar{s}_{11}}} \beta_n^2 ; \quad (4.16)$$

where  $d$  is the thickness of the laminate,  $l$  the length of the laminate,  $\bar{\rho}$  the average density of the laminate,  $\bar{s}_{11}$  the equivalent elastic compliance, and  $\beta_n \approx (n+1/2)$  the mode order. The average density  $\bar{\rho}$  and equivalent elastic compliance  $\bar{s}_{11}$  of our three-phase bending-mode laminates are then:

$$\bar{\rho} = \gamma_m \rho_m + \gamma_s \rho_s + \gamma_p \rho_p \quad (4.17a)$$

$$\bar{s}_{11} = \frac{S_{11}^m S_{11}^p S_{11}^s}{\chi_m S_{11}^p S_{11}^s + \chi_m S_{11}^m S_{11}^s + \chi_s S_{11}^m S_{11}^p} ; \quad (4.17b)$$

where  $\gamma_m$ ,  $\gamma_s$ , and  $\gamma_p$  are the volume fractions of Terfenol-D, elastic-steel, and PZT-850 layers, respectively;  $\rho_m$ ,  $\rho_s$ , and  $\rho_p$  the respective densities of the layers;

$S_{11}^m$ ,  $S_{11}^s$ , and  $S_{11}^p$  the respective elastic compliances of the layers; and  $\chi_m$ ,  $\chi_s$ , and  $\chi_p$  the respective cross-sectional area fractions. Using typical material parameters for the respective layers of the laminate given in Tables IV-IV, equations (4.16) and (4.17), and the laminate geometries given above, I can predict the resonance frequency of the 1<sup>st</sup> bending mode (n=1) of the three-phase laminates to be ~5.1kHz. This predicted value is very close to the measured one (as will be shown below in Fig.4-28).

I next calculated the vibrations of the 1<sup>st</sup> bending-mode of our three-phase ME laminate using Finite Element Analysis (FEA), assuming free-free boundary conditions, as shown in Fig.4-27. Both nodes were located near the two ends of the Terfenol-D layers. Since the middle part of the laminate has higher effective stiffness and mass than those at the two ends, the vibration amplitudes at the ends are much larger than that at the center. Furthermore, the elastic-steel (high  $Q_m$ ) layer will increase the effective mechanical factor  $Q_{m,eff}$  of the laminate, which will in turn increase the resonance-enhancement of  $V_{ME}$ , in a manner that is directly proportional to the  $Q_{m,eff}$  of the laminate, given as:<sup>74</sup>

$$dV_{ME} / dH \propto \frac{Q_{m,eff} \varphi_m \varphi_p}{Z_0} \quad (4.18)$$

where  $\varphi_m$  and  $\varphi_p$  are magneto-elastic and elasto-electric coupling factor in the bending-mode, and  $Z_0$  the characteristic mechanical impedance of the laminate.

Experimental investigations of the ME properties were then carried out by placing the laminates in a Helmholtz coil (holding the sample at the two nodes), and applying a small ac magnetic field ( $H_{ac}$ ) along the longitudinal direction of the laminate. A DC magnetic bias ( $H_{dc}$ ) was superimposed to  $H_{ac}$  along that same direction. The voltages

*Table IV-IV. Typical material parameters for the laminate layers..*

	Qm	Density (g/cm <sup>3</sup> )	Elastic Compliance (m <sup>2</sup> /N)	Volume Fraction	Area Fraction
Terfenol-D	<10	9.2	1.67×10 <sup>-11</sup>	0.463	0.651
Steel	~200	7.7	5.12×10 <sup>-12</sup>	0.0865	0.053
PZT-850	~80	7.7	1.59×10 <sup>-11</sup>	0.225	0.296

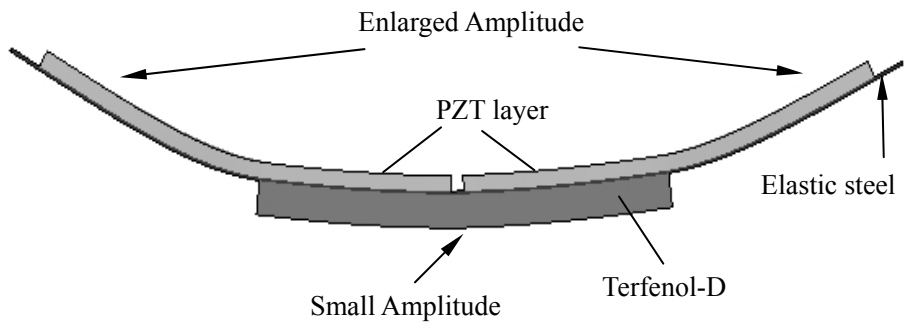


**Fig.4-27.** Illustration of the 1st bending-mode vibrations, calculated using FEA method.

induced across the PZT layer(s) were then measured for various  $H_{dc}$  and  $H_{ac}$  over a wide frequency range of 10 ~50k Hz, using a lock-in amplifier method.

Fig.4-28(a) shows  $V_{ME}$  (in V/cm-Oe) for both our three-phase bending-mode laminate (Fig.4-26(a)), and for comparisons a corresponding unimorph (Fig.4-26(b)). Data are shown as a function of  $H_{dc}$  at a measurement frequency of  $f=100\text{Hz}$ . A maximum value of  $V_{ME}$  can be seen for both laminates at  $H_{dc}\approx 300\text{Oe}$ : this maximum occurs when the magnetic layer has a maximum effective piezomagnetic coefficient. At low frequencies (sub-resonant), the unimorph ME laminate has a notably higher value of  $V_{ME}$  than our three-phase one. From these data, it can be concluded that a co-laminated elastic-steel layer in ME laminates does not facilitate ME coupling at low frequencies. However, under resonance drive, I will next show that co-lamination with an elastic-steel layer increases the resonance-enhancement of  $V_{ME}$ . Fig.4-28(b) shows  $V_{ME}$  of both the bending-mode and unimorph laminates as a function of the drive frequency. In this figure, the three-phase bending-mode laminate can be seen to have a sharp resonance frequency at  $\sim 5\text{kHz}$ , in agreement with that predicted by (4.16), with a resonance-enhanced ME coefficient of  $V_{ME}=40\text{V/cm-Oe}$ . Whereas, the unimorph of similar Terfenol-D and PZT layer geometries had a 1<sup>st</sup> bending-mode resonance frequency of 19.2kHz, and a resonance-enhanced  $V_{ME}$  of 22V/cm-Oe.

The effective mechanical quality factor can be determined from the resonance peak as  $Q_{m,eff} = f_r/\Delta f$ , where  $\Delta f$  is the 3-dB bandwidth. For our three-phase laminate  $Q_{m,eff} \approx 78$ , whereas that of the unimorph was  $\approx 30$ : a ratio of  $\approx 2.6:1$ , similar to that experimentally observed in  $V_{ME}$  (see Fig.4-28(b)), and consistent with predictions of

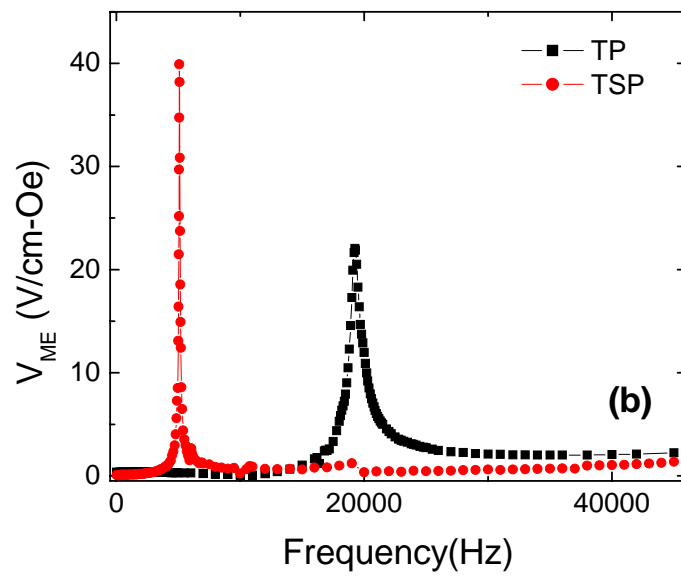
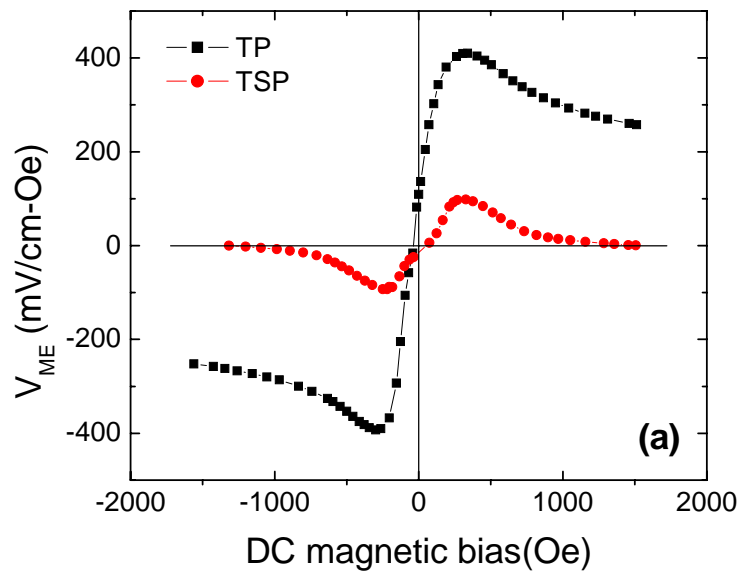


**Fig.4-28.** Magnetolectric voltage coefficient ( $V_{ME}$ ) for both our Terfenol-D/Steel/PZT and Terfenol-D/PZT laminates: (a) as a function of DC magnetic bias taken at a measurement frequency of  $f=100\text{Hz}$ ; and (b) as a function of frequency taken under a DC magnetic bias of  $H_{dc}=300\text{Oe}$ .

(4.18). These data demonstrate that a relatively high  $Q_m$  elastic phase will increase the value of laminate's  $Q_{m,eff}$ , which result in increased resonance-enhancement in  $V_{ME}$ . The results provide new insights into how enhanced ME interactions over desired frequency ranges can be developed by novel laminate configurations.

The effective mechanical quality factor can be determined from the resonance peak as  $Q_{m,eff} = f_r/\Delta f$ , where  $\Delta f$  is the 3-dB bandwidth. For my three-phase laminate  $Q_{m,eff} \approx 78$ , whereas that of the unimorph was  $\approx 30$ : a ratio of  $\approx 2.1$ , similar to that experimentally observed in  $V_{ME}$  (see Fig.4-28(b)), and consistent with predictions of (4.18). These data demonstrate that a relatively high  $Q_m$  elastic phase will increase the value of laminate's  $Q_{m,eff}$ , which results in increased resonance-enhancement in  $V_{ME}$ . The finding provides insights into how enhanced ME interactions over desired frequency ranges can be developed by designing laminate configurations: such flexibility could be important to electromagnetic energy conversion, sensors, filters, and resonators based on ME laminates.

#### **4.5 Discussion and Summary.**

In this Chapter, I have investigated detection sensitivity optimization for various ME laminates sensors. These investigations can be divided into those considering internal and external noise effects. Some useful results have been found, which can be summarized as follows:

- (1) Optimization on considering the internal noise (single element):** I theory predicts and experiments confirm (for various ME sensors using the same

detection circuitry) that noise is proportional to  $\sqrt{C}$ , and that the SNR is proportional to  $\sqrt{V} \cdot \alpha_{ME}$ . Highly sensitive ME laminate can be designed by either increasing the ME voltage coefficient  $\alpha_{ME}$ , or increasing the effective volume V of the piezoelectric phase.

- (2) **Optimization on considering the internal noise (multiple elements):** ME arrays in parallel increase the signal and noise currents by factors of m and  $\sqrt{m}$ , respectively; while ME arrays in serial do not increase the signal, but reduce the noise by  $\sqrt{m}$ . Accordingly, the signal-to-noise ratio increases by a factor of  $\sqrt{m}$ , for both serial and parallel modes. Highly sensitive ME laminate sensor can be design by either serial or parallel ME units.
- (3) **Optimization on considering the external noise:** *First*, if the mode produced by the ME signal is the same as that made by noise, then the ME signal and noise can not be separated. Only filters or magnetic gradiometers might help in this case, but then only at the expense of decreased ranging capabilities. *Second*, to separate noise and the ME signal, a ME sensor should be designed such that the ME signal occurs in one mode, whereas the noise is constrained in another. Then, and only then, can one use a differential method to cancel the noise while not rejecting the signal. *Third*, certain laminate configurations have built-in vibration cancellation capabilities. These are the SS-US (symmetrical signal, unsymmetrical noise) modes, such as L-T, L-L, TT, TL, and push-pull. If the environment that the sensor is required to operate in has a high degree of vibrations, one of these SS-UN modes is best suited for that

environment. To further reduce vibrational noise, I recommend using laminates with a high stiffness in the transverse direction: this can be accomplished simply by use of a thicker ME laminate. If the sensor is limited to be thin, then I recommend using multi-layer stacks. *Fourth*, in signal symmetrical structures, thermal noise can not be rejected from the signal. This is simply because the thermal noise is introduced, via longitudinal / transverse deformation, similar to the signal. Accordingly, US-SN (unsymmetrical signal, symmetrical noise) modes have the ability to cancel thermal noise. If the environment in which the ME sensor operates is exposed to significant thermal changes, then US-SN mode ME laminate configurations are the best choice as magnetic sensors.

- (4) Optimization basing on decreasing bending mode frequencies: three-phase laminates have (i) larger resonance enhancements in the ME voltage coefficient (i.e., high  $Q_{m,eff}$ ), while operated at (ii) significantly lower resonance frequencies (i.e., length extensional bending-mode vibration).

*Parts of these chapter are reprint from the reference<sup>75, 76</sup>*

# CHAPTER 5

## ME DETECTION CIRCUIT OPTIMIZATION

### 5.1 Introduction

A ME detection system consists not only the ME sensor but also the detection circuit. To acquire a best magnetic field detection performance, we should also take the circuit optimization into the design consideration. Previous investigations have shown that a charge detection scheme is the best method by which to implement a ME sensors. Fig.5-1 illustrates this fundamental detection topology: it has been known and used for decades. Provided that  $C_i \ll gC_f$ , the effective input capacitance is  $C_{\text{eff}} = (1+g)C_f$ , which is independent of  $C_i$ : where  $C_i$  and  $C_f$  are input and feedback capacitances, and  $g$  is the open loop gain of the charge amplifier. Thus, the output signal is  $V_{\text{out}} \approx Q_i/C_f$ , where  $Q_i$  is the input charge.<sup>77-83</sup>

Until now, many highly sensitive charge amplifiers have been developed.<sup>84-87</sup> However, little attention has been given to how to increase the signal-to-noise ratio (SNR) in CCSS measurements that uses the fundamental charge amplifier topology of Fig.5-1. In the following sections, I will investigate the SNR of this measurement and determine how various equivalent parameters (such as feedback capacitance  $C_f$ , feedback resistance  $R_f$ , etc.) affect the sensitivity. I will also introduce a method which will increase the SNR or sensitivity further. Simulations were also carried out to verify the theory. Only intrinsic noise will be considered in this chapter.

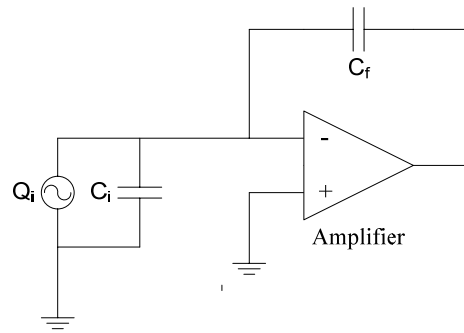


**Fig.5-1.** Fundamental topology for a charge amplifier.

## 5.2 SNR on feedback components

### 5.2.1 Charge scheme and SNR calculation

Fig.5-2 illustrates an equivalent circuit that includes intrinsic noise (Johnson noise, shot noise, 1/f noise, etc) for the ME measurement. This is a necessary modification to Fig.5-1 for practical considerations. The parameters  $i_{nR}$  and  $i_{ns}$  are the spectral current noise densities of the feedback resistor and source sensor, and  $i_n$  and  $e_n$  are the equivalent input spectral current and voltage noise densities of the amplifier. To simplify, I assume that all noise sources are uncorrelated except  $i_n$  and  $e_n$ : some noise source in the amplifier might contribute to both  $e_n$  and  $i_n$ , making them correlated.<sup>51</sup> The  $e_n$ - $i_n$  correlation factor is designated as  $\rho$ . The charge gain  $H(s)$ , current noise ( $i_n$ ,  $i_{ns}$ ,  $i_{nR}$ ) gain  $Z_n(s)$ , and the voltage noise ( $e_n$ ) gain  $A_n(s)$  are given as follows

$$\begin{aligned} H(s) &= \frac{sR_f}{(1 + sR_f C_f) \cdot \left(1 + \frac{if}{f_x}\right)}; \\ Z_n(s) &= \frac{R_f}{(1 + sR_f C_f) \cdot \left(1 + \frac{if}{f_x}\right)}; \\ A_n(s) &= \frac{R_i + R_f}{R_i} \frac{1 + s\overline{RC}}{(1 + sR_f C_f) \cdot \left(1 + \frac{if}{f_x}\right)}; \end{aligned} \quad (5.1)$$

where  $f_x = \text{GBP}/(1 + C_i/C_f)$  and GBP is the amplifier's gain bandwidth product;

$\overline{R} = R_f // R_i$  and  $\overline{C} = C_f + C_i$ . The SNR is then

$$SNR = \frac{V_s}{V_n} = \frac{Q \cdot H(f)}{\left( \int_{f_L}^{f_H} \left( i_{nR}^2 \cdot |Z_n(f)| + e_n^2 \cdot |A_n(f)|^2 + 2\rho \cdot i_n \cdot e_n \cdot |Z_n(f)| \cdot |A_n(f)| \right) df \right)^{\frac{1}{2}}}; \quad (5.2)$$

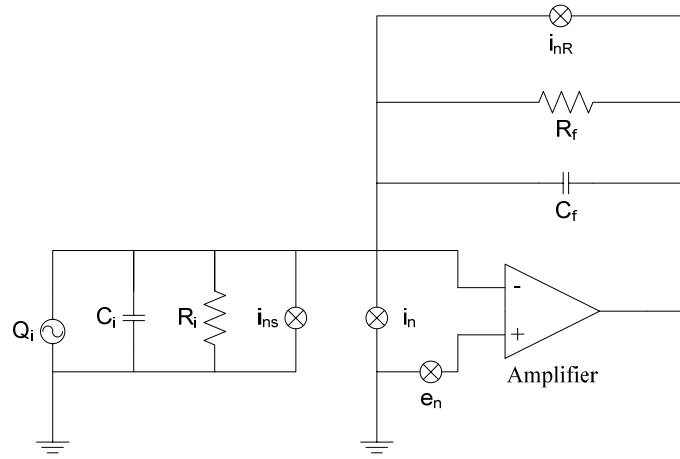


**Fig.5-2.** ME charge measurement scheme.

where  $i_{nt}^2 = i_{ns}^2 + i_n^2 + i_{nR}^2$ . In fact,  $V_n$  does not change notably with the signal frequency; whereas,  $V_s$  does simply because the charge gain  $H(f)$  is frequency dependent.

Now, consider the charge flat response range of  $f_p \sim f_x$  ( $f_p = 1/(2\pi R_f C_f)$ ). In this range,  $H(f)$  can be simplified to be the constant  $1/C_f$ . Equation (5.2) then simplifies to

$$SNR = \frac{Q}{C_f \cdot \left( \int_{f_L}^{f_H} \left( i_{nt}^2 \cdot |Z_n(f)|^2 + e_n^2 \cdot |A_n(f)|^2 + 2\rho \cdot i_n \cdot e_n \cdot |Z_n(f) \cdot A_n(f)| \right) df \right)^{\frac{1}{2}}}; \quad (5.3)$$

where  $i_{nt}^2 = i_{ns}^2 + i_n^2 + i_{nR}^2$ . The affect of SNR on the charge flat response range becomes  $\int_{f_L}^{f_H} E_N df$ , where

$$E_N = \left( \left( i_{ns}^2 + i_n^2 + \frac{4kT}{R_f} \right) \cdot |C_f \cdot Z_n(f)|^2 + e_n^2 \cdot |C_f \cdot A_n(f)|^2 + 2\rho \cdot i_n \cdot e_n \cdot |C_f^2 \cdot Z_n(f) \cdot A_n(f)| \right). \quad (5.4)$$

The factors that affect  $E_N$  can be categorized as:

$$F_1 = |C_f \cdot Z_n(f)|^2 = \frac{R_f^2 C_f^2}{\beta}; \quad (5.5a)$$

$$F_2 = \frac{4kT}{R_f} |C_f \cdot Z_n(f)|^2 = \frac{4kTR_f^2 C_f^2}{\beta}; \quad (5.5b)$$

$$F_3 = |C_f \cdot A_n(f)|^2 = \frac{C_f^2}{R_i^2} \cdot \frac{(R_i + R_f)^2 + \omega^2 R_i^2 R_f^2 (C_i + C_f)^2}{\beta}; \quad (5.5c)$$

$$F_4 = |C_f^2 \cdot Z_n(f) \cdot A_n(f)| = \sqrt{F_1 \cdot F_3}; \quad (5.5d)$$

$$\beta = \left( 1 + \omega^2 R_f^2 C_f^2 \right) \cdot \left( 1 + \left( \left( 1 + \frac{C_i}{C_f} \right) f \right) \right) \Bigg|_{GBP} \Bigg|^2.$$

Clearly, to achieve a higher SNR, one needs a lower value of  $E_N$ . From (5.4) and (5.5), we can see that lower values of  $F_1$ ,  $F_2$ ,  $F_3$ , and  $F_4$  will result in a lower  $E_N$ .

## 5.2.2 Special case considerations

I discuss below specific cases of how  $C_f$  and  $R_f$  affect the values of  $F_1$ ,  $F_2$ ,  $F_3$  and  $F_4$ . I assume that there is not a filter behind the charge amplifier in these case.

*Case 1: Reduce  $C_f$  while fixing  $R_f$*

From (5.5) we can see that  $F_1$ ,  $F_2$ ,  $F_3$ , and  $F_4$  decrease with decreasing  $C_f$ . As a result, the value of SNR in (5.3) will be increased. However, for a fixed  $R_f$ , the value of  $C_f$  will be limited by the lowest flat charge response frequency  $f_1$ . Furthermore, I also require that  $f_x \gg f_p$  (frequency bandwidth and stability requirement), so we have:

$$\frac{1}{2\pi R_f \cdot C_f} = f_p \leq f_1; \quad \frac{1}{2\pi R_f \cdot C_f} \ll \frac{GBP}{1 + \frac{C_i}{C_f}}. \quad (5.6a)$$

$$\text{or, } C_f \geq \frac{1}{2\pi R_f f_1}; \quad 2\pi R_f \cdot GBP \cdot C_f^2 - C_f \gg C_i. \quad (5.6b)$$

*Case 2: Reduce  $C_f$  while fixing the frequency  $f_p = f_1$ :*

We can also see that  $F_1 \sim F_4$  will be reduced as  $C_f$  is decreased; consequently, the SNR will increase. This provides a strategy for feedback component choosing: if we have  $R_f = 1G\Omega$ ,  $C_f = 100pF$  and  $R_f = 100Meg\Omega$ ,  $C_f = 1000pf$ , both of which will have the same charge corner frequency, then we know that the first choice will provide higher sensitivity.

*Case 3: Reduce  $R_f$  while fixing  $C_f$ :*

From (5.5), we can see that  $F_1$  continuously decreases with reduction in  $R_f$ . However,  $F_2$  is not monotonic with  $R_f$ . For  $R_f < 1/(\omega C_f)$ ,  $F_2$  increases with increasing  $R_f$ ;

whereas, for  $R_f > 1/(\omega C_f)$ , it decreases. So, choosing either a  $R_f$  as small or as large as possible is a best way to minimize  $F_2$ . A minimum in  $F_3$  occurs at a specific  $R_f$ ,

$$\text{where } R_f = \frac{R_i C_i^2 + 2R_i C_i C_f + 1 + \sqrt{(R_i C_i^2 + 2R_i C_i C_f + 1)^2 + 4\omega^2 R_i^2 C_f^2}}{2\omega^2 R_i C_f^2}.$$

However, minima in neither  $F_2$  nor  $F_3$  occur at the same value: this makes optimization a complex problem for analysis. In this case, the best way to find an optimized value of  $R_f$  is by using computer-based calculation tools.

*Case 4: Reduce  $R_f$  while fixing the frequency  $f_p=f_1$ :*

This will result in an increase of  $C_f$  simply because of  $f_p=1/(2\pi R_f C_f)$ . I can refer to case 2 considered above, and draw the conclusion that reducing  $R_f$  with  $f_p=f_1$  will decrease SNR.

These special considerations show how the SNR is affected by  $C_f$  and  $R_f$ . In order to achieve a high SNR, a small  $C_f$  value that satisfies (5.6) should be selected. Furthermore, we can draw a useful conclusion for the design that if the lowest required measurement frequency of the charge source is  $f_1$ , then it is not necessary to make the high corner frequency ( $f_p$ ) of the charge amplifier lower than  $f_1$ : as doing so will decrease the system's SNR.

In addition to  $R_f$  and  $C_f$ , the source impedance also needs to be taken into consideration when optimizing the SNR. With changing  $R_i$ , only  $F_3$  and  $F_4$  are affected: increasing  $R_i$  decreased both, and accordingly SNR will be increased. For the parameter  $C_i$ , the situation becomes a little more complicated. But we can turn to a more practical case where a low pass filter is always placed behind the charge

amplifier to limit the bandwidth and lower the noise level. This will change  $F_{i=1-4}$ , because terms for low-pass poles need to be inserted into the denominators of the respective equations for  $F_{i=1-4}$ , and the  $(1+jf/f_x)$  terms can be neglected. In this case, only  $F_3$  and  $F_4$  are affected by  $C_i$ . Both will decrease with decreasing  $C_i$ , and consequently SNR will increase. When a low pass filter is introduced, the trends discussed in case 1~ case 4 are still the same, except that equation (6) becomes

$$\frac{1}{2\pi R_f \cdot C_f} = f_p \leq f_1; \quad \frac{1}{2\pi R_f \cdot C_f} \ll f_H \quad (5.7a)$$

$$\text{or, } C_f \geq \frac{1}{2\pi R_f f_1}; \quad 2\pi R_f \cdot f_H \gg C_f; \quad (5.7b)$$

where  $f_H$  is the corner frequency of the low pass filter induced.

Previous analysis has shown that we can choose large value for  $R_f$  and reduce  $C_f$  to achieve high SNR. However, this may not always be a practical method, since the bias current of the amplifier will saturate the output when the feedback resistor  $R_f$  becomes too large. In the consideration of the bias current, we need to satisfy

$$I_b \cdot R_f \ll V_s; \quad (5.8)$$

where  $I_b$  is the bias current and  $V_s$  the saturation output voltage of the amplifier. In addition, stray capacitances and resistances are other practical design limitations that require consideration. It has been recommended that the feedback capacitor  $C_f$  should not be less than 10pF.

### 5.2.3 Spice simulation result

Spice simulations of the output noise level  $V_{no}$  and signal-to-noise ratio SNR were performed as a function of the feedback capacitance  $C_f$  and feedback resistance  $R_f$ .

Source impedances and noise features used in the simulations are given in Table V-I.

The charge output of the CCSS during simulations was set to be 100fC.

Simulation results for  $V_{no}$  and SNR as a function of  $C_f$  ( $10^{-12}$  to  $10^{-9}$ F) are shown in Fig.5-3, at various frequencies. These simulations were done using a fixed feedback resistance of  $R_f=1G\Omega$ . In this figure, we can see that  $V_{no}$  and SNR are both increased as  $C_f$  is reduced.

Next, simulations were performed with a fixed frequency of  $f_p=f_1=10$ Hz, while  $C_f$  was varied. In Fig.5-4, we can see as  $C_f$  is reduced that  $V_{no}$  is notably increased. However, in this case, the SNR was only slightly increased, except that is at extremely low values of  $C_f$ . Finally, we simulated  $V_{no}$  and SNR as a function of  $R_f$  at various frequency, using a feedback capacitance fixed at  $C_f=100$ pF. As shown in Fig.5-5, the output noise level increased with increasing  $R_f$ , whereas the SNR decreased.

The simulations show that a highly sensitive ME measurement system is not necessarily a low output noise system. And the findings also suggest that the way to obtain high SNR by reducing  $C_f$  as much as possible.

## **5.3 New charge topology for SNR improvement**

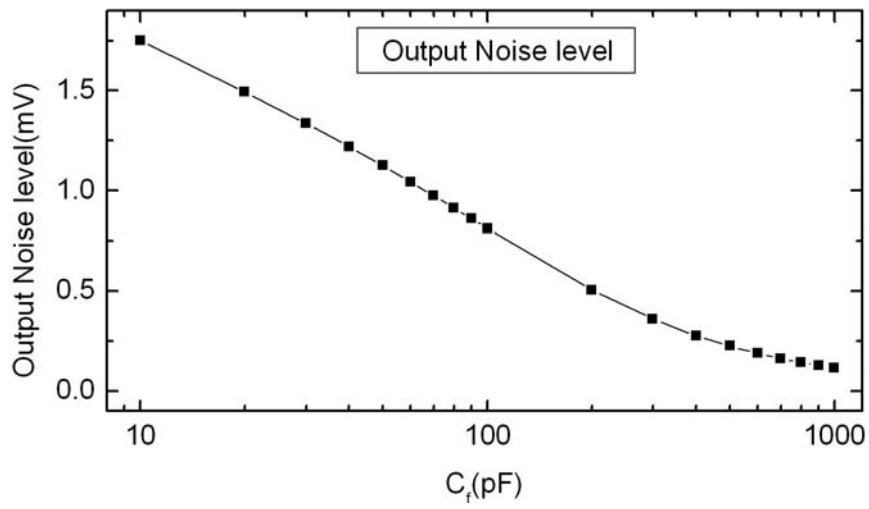
### **5.3.1 High SNR charge measurement topology: Theory**

The charge scheme shown in Fig.5-2 has been widely used in capacitive charge source sensor measurements. The transfer function  $H_s(s)$  of the output signals response to the input charge  $Q_i$ , and the current noise gain  $Z_n(s)$  are as follows:

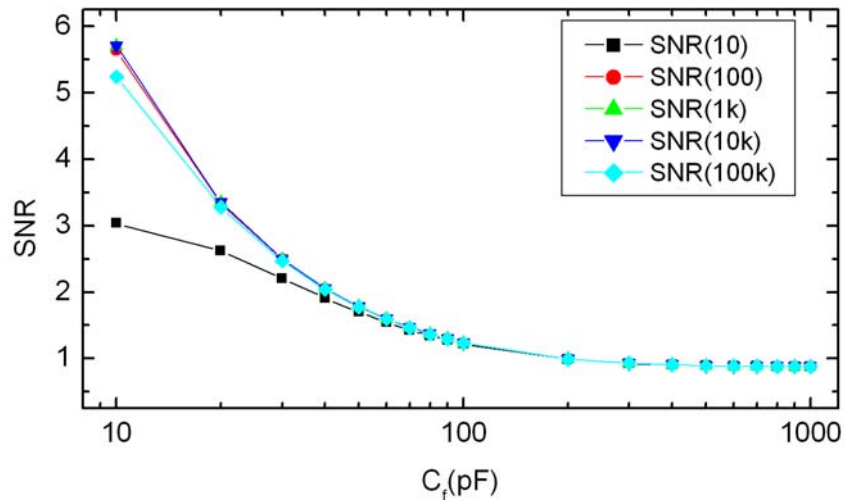
*Table V-I. Impedance and noise features of the sensor for simulation.*

Parallel resistance $R_i(\Omega)$	Parallel capacitance $C_i(F)$	White noise floor $i_{nw}(fA/\sqrt{Hz})$	1/f Noise corner frequency $f_{ci}(Hz)$
1G	1n	100	100

The Operational amplifier for the simulation is AD745 from Analog Corp.

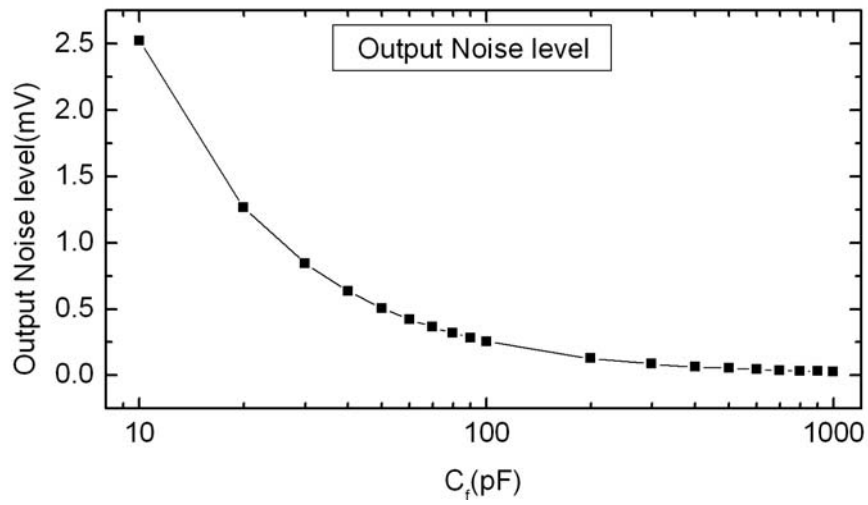


(a)

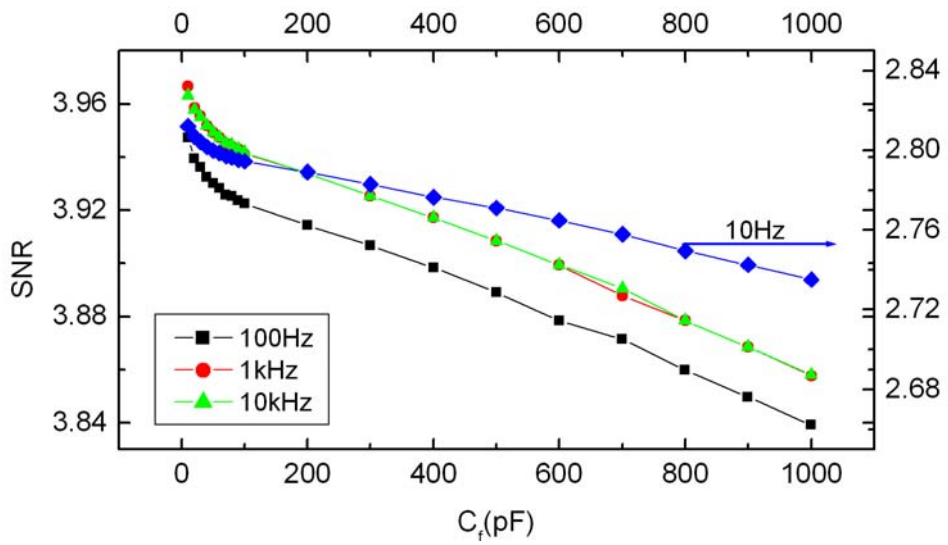


(b)

**Fig.5-3.** Simulation as a function of feedback capacitance ( $10^{-12} < C_f < 10^{-9}$  F) at various frequencies for (a) output noise level  $V_{no}$ , and (b) signal to noise ratio SNR. The simulations were performed using a fixed feedback resistance of  $R_f = 1$  G.

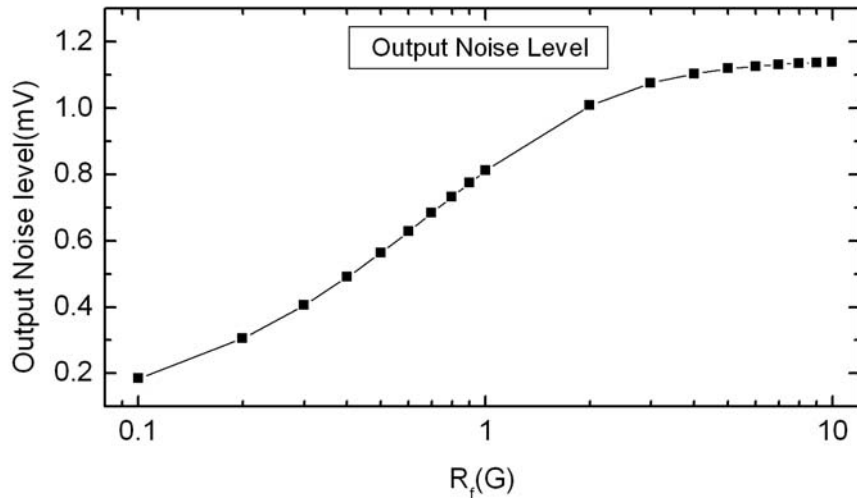


(a)

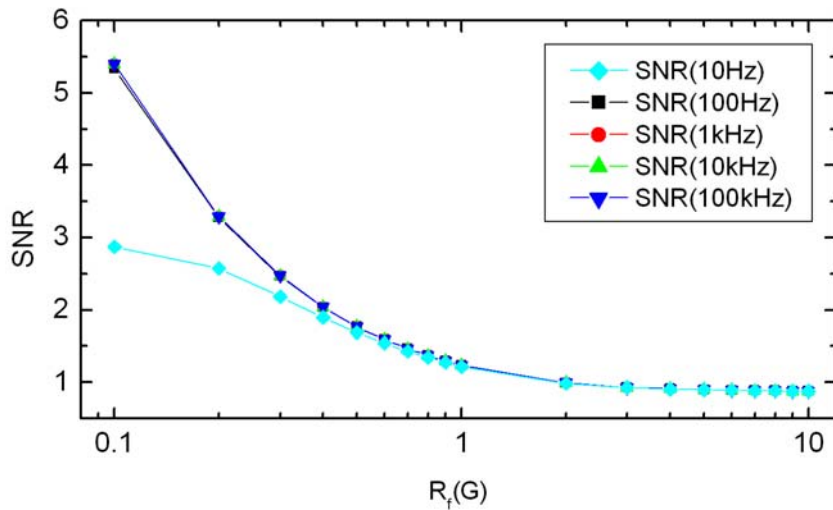


(b)

**Fig.5-4.** Simulation as a function of feedback capacitance ( $10^{-12} < C_f < 10^{-9}$ F) for (a) output noise level  $V_{no}$ , and (b) signal to noise ratio SNR. The simulations were performed using a fixed frequency of  $f_p = f_1 = 10$ Hz.



(a)



(b)

**Fig.5-5.** Simulation as a function of feedback resistance ( $10^8 < R_f < 10^{10} \Omega$ ) at various frequencies for (a) output noise level  $V_{no}$ , and (b) signal to noise ratio SNR. The simulations were performed using a fixed feedback capacitance of  $C_f = 100 \text{pF}$ .

$$H_s(s) = \frac{sR_f}{(1 + sR_f C_f)}, \quad (5.9a)$$

$$Z_n(s) = \frac{R_f}{(1 + sR_f C_f)}; \quad (5.9b)$$

where  $s = \sigma + j\omega$  is a complex frequency in complex nepers per second, here  $\sigma$  is the neper frequency in nepers per second and  $\omega$  is the angular frequency in radians per second.

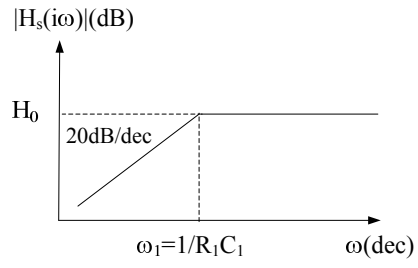
The Bode plot of these transfer functions are given in Fig.5-6, where  $H_0 = Q/C_f$  and  $Z_0 = R_f$ . From Fig.5-6, we can see that the transfer functions of  $H_s(s)$  and  $Z_n(s)$  are different. For the  $H_s(s)$ , there is a zero at the frequency of  $\omega = 0$  and a pole at  $\omega = \omega_1 = 1/(R_1 C_1)$ , whereas for  $Z_n(s)$ , only a pole at  $\omega = \omega_1 = 1/(R_1 C_1)$ .

For a charge measurement unit to achieve a high sensitivity, the corner frequency  $f_p$  of the charge amplifier should not be lower than that of the lowest frequency signal to be detected ( $f_1$ ). If we introduce a high pass high order filter with a corner frequency slightly lower than  $f_p$  just behind the charge amplifier, then the charge response in the measurement frequency of interested will not be significant change. However the noise gain will be notably change. This will reduce the output noise level. To understand, we thus draw the fundamental topology as given in Fig.5-7(a).

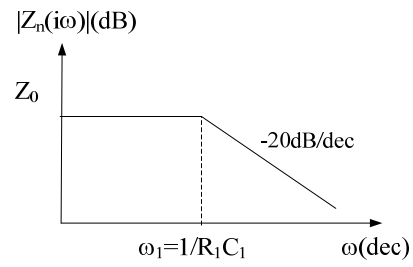
The output signal response  $H_{s1}(s)$  and the current noise gain  $Z_{n1}(s)$  can be obtained from the topology of Fig.5-7(a), as follows

$$H_{s1}(s) = \frac{sR_f}{(1 + sR_f C_f)} \cdot H_{hp}(s), \quad Z_{n1}(s) = \frac{R_f}{(1 + sR_f C_f)} H_{hp}(s); \quad (5.10)$$

where  $H_{hp}(s)$  is the transfer function of the high pass high order filter that we introduced. We can then illustrate these transfer functions in the Bode plot of Fig.5-7,

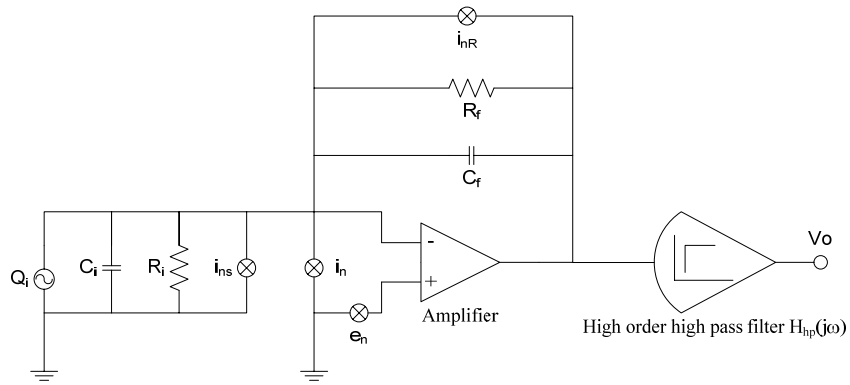


(a)

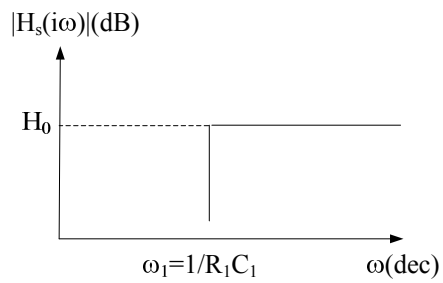


(b)

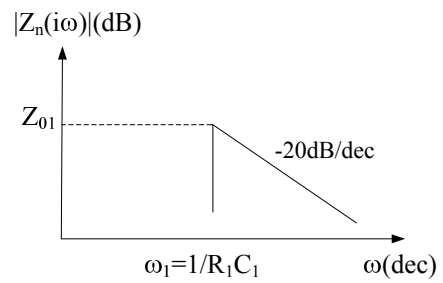
**Fig.5-6.** Transfer function of the (a) signal response  $H_s(s)$  and (b) current noise gain  $Z_n(s)$ .



(a)



(b)



(c)

**Fig.5-7.** (a) The high SNR topology; (b) transfer function of the signal response  $H_{s1}(s)$ ; and (c) transfer function of current noise gain of  $Z_{n1}(s)$ .

where  $H_0=Q/C_f$  and  $Z_0=R_f$ .

By comparing Fig.5-6(a) and Fig.5-7(b), we can see that the signal's response at frequencies higher than  $\omega_1$  is not changed by the insertion of the high pass filter. However, the current noise gain is notably change. The value of  $|Z_n(j\omega)|$  is notably smaller in Fig.5-7(c) than in Fig.5-6(b), and the output noise level  $E_{no}$  is given as:<sup>49, 51</sup>

$$E_{no} = \left( \int_{f_L}^{f_H} i_n^2(\omega) |Z_n(j\omega)|^2 df \right)^{0.5} . \quad (3)$$

This means that the output noise level from the fundamental topology of Fig.5-7(a) is lower than that of Fig.5-2. Correspondingly, the SNR (sensitivity) of Fig.5-7(a) is higher than that of Fig.5-2.

### 5.3.2 Spice Simulation

To test the prediction, a spice simulation was performed. I set the source sensor to have the properties as shown in table V-II. The simulated spectral voltage noise density from the I-V conversion (H device, gain=1) of the source sensor is then shown in Fig.5-8, which yielded a simulated source current noise density close to that required in Table V-II.

The charge source measurement frequency range that we are interested in is  $10\text{Hz} < f < 1\text{kHz}$ . I accordingly set up a fundamental measurement circuitry for simulation, including a high-pass high-order filter behind the charge amplifier. I used a 4th order high-pass Butterworth filter with a corner frequency of  $\sim 10\text{Hz}$ . The fundamental circuitry topology that we simulated is given in Fig.5-9.

*Table V-II. Properties of the source sensor for simulation.*

Parallel resistance $R_i(\Omega)$	Parallel capacitance $C_i(F)$	Charge $Q(C)$	$1/f$ Noise corner frequency $f_{ci}(Hz)$	White noise floor $i_{nw}(fA/\sqrt{Hz})$
10G	1n	1p	10	100

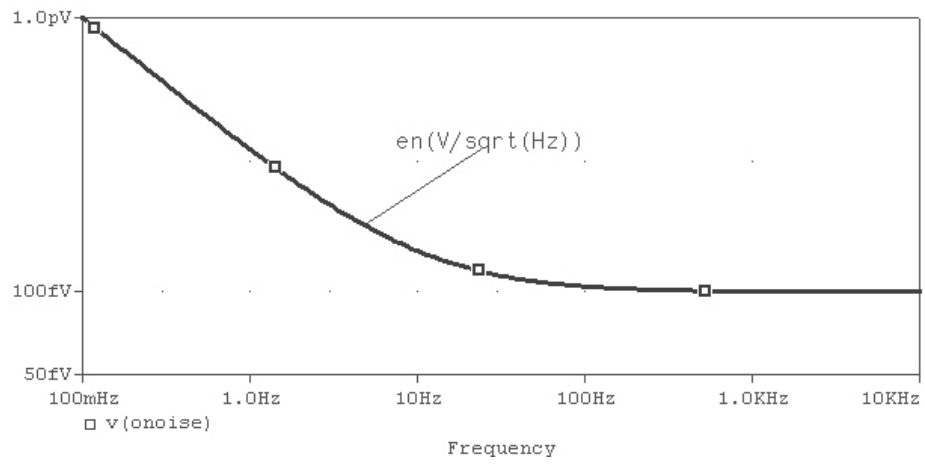


**Fig.5-8.** Source spectral current noise density.

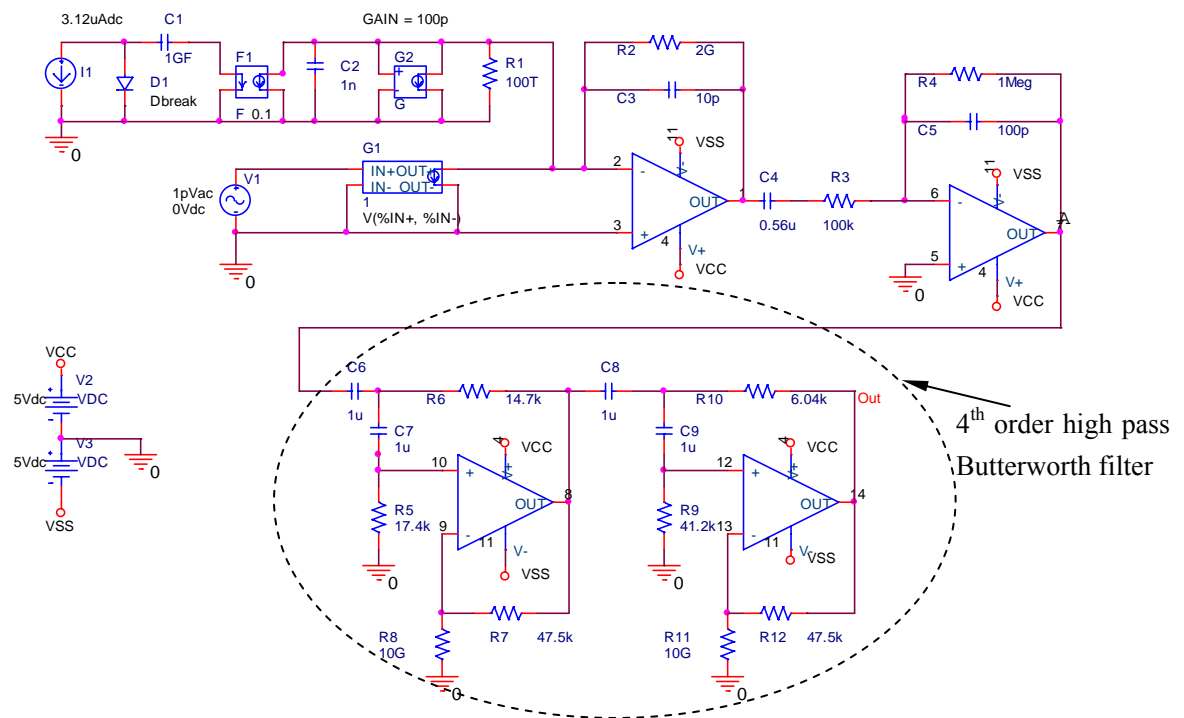


**Fig.5-9.** Charge amplifier with high pass filter simulation circuitry.

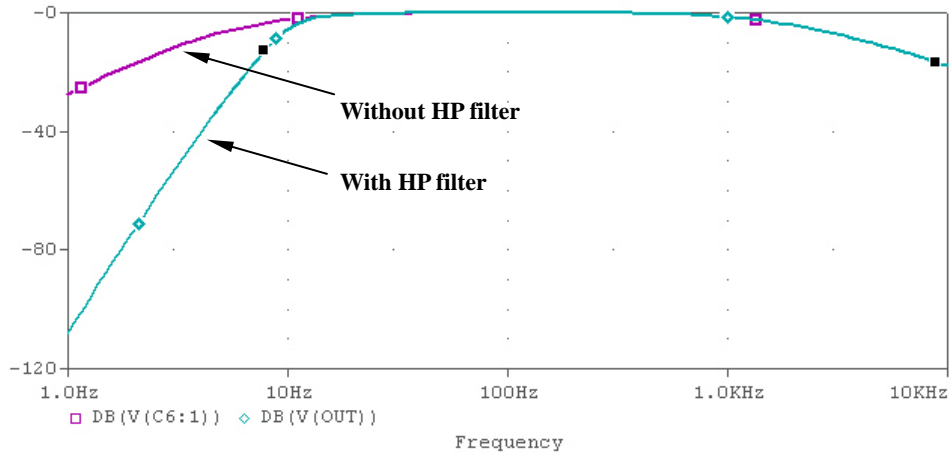
The Bode plots of the charge signal response, both before and after introducing the 4<sup>th</sup> Butterworth filter, are shown in Fig.5-10(a). We can see that the signal responses are almost the same in the frequency range of 10 Hz ~ 1kHz. However, the noise levels were not the same before and after introducing the 4<sup>th</sup> order Butterworth high-pass filter, as can be seen in noise level given in Fig.5-10(b).

We can then determine how the 4th order filter affected the SNR, as plotted in Fig.5-11. Clearly, we can see that the high order high pass filter improves the SNR of the charge measurement unit over the bandwidth of  $10 < f < 1\text{kHz}$ . This means the measurement unit will be able to better distinguish smaller signals from noise.

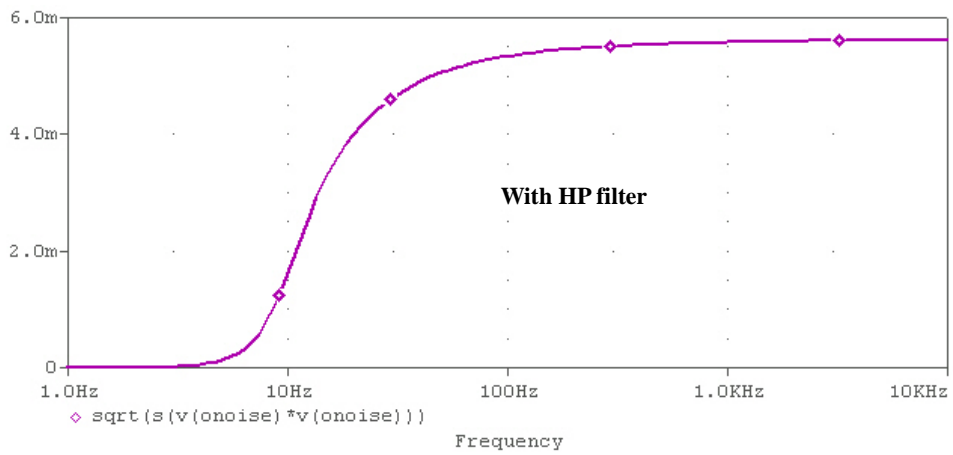
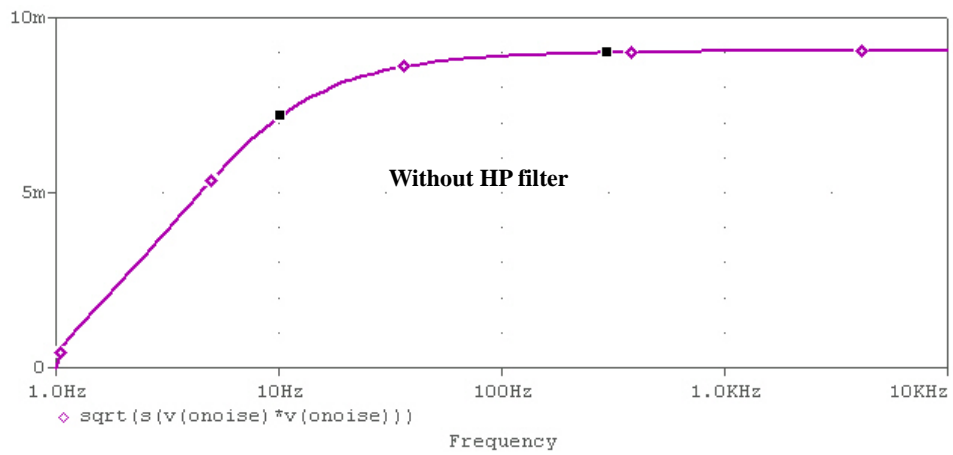
## 5.4 Summary

In this Chapter, I have investigated the fundamental charge scheme and proposed a new charge topology to increase the SNR. Pspice simulations confirmed the result. I summarize them as follows:

- (5) Values of the feedback components in the fundamental charge scheme will affect the detection sensitivity. Proper choice of the feedback component is very important. I have set up rules for this optimization, which require the component values to meet criteria (5.6) or (5.7) and (5.8). For the design, if the lowest required measurement frequency of the charge source is  $f_1$ , then it is not necessary to make the high corner frequency ( $f_p$ ) of the charge amplifier lower than  $f_1$ : as doing so will decrease the system's SNR.



(a)



(b)

**Fig.5-10.** (a) Signal response with and without the high pass filter; and (b) Output noise level with and without High pass (HP) filter.

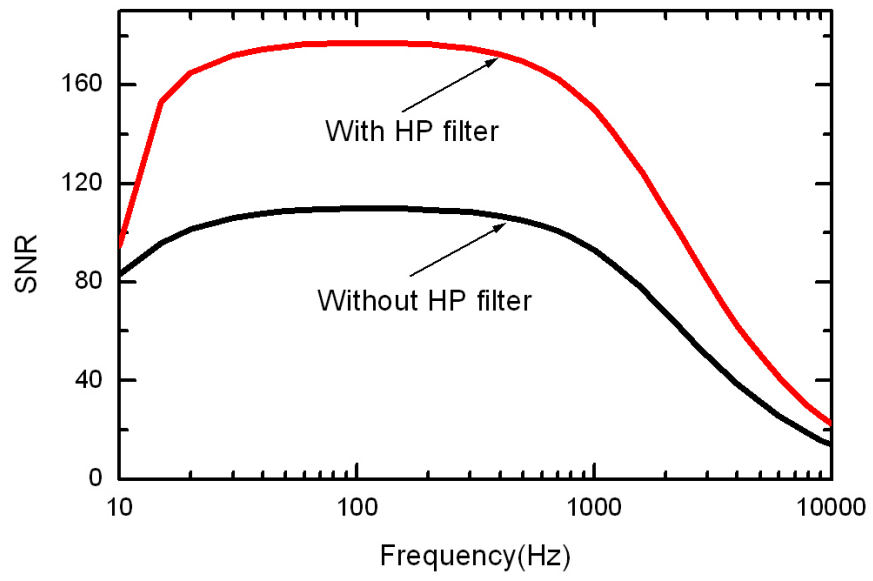


**Fig.5-11.** SNR comparison before and after add the HP filter.

- (6) A high-pass high-order filter, which was placed behind the fundamental charge amplifier, can reduce the output noise level, while keeping the signal almost unchanged in the bandwidth of interests. This means that the sensitivity of the charge measurement unit will be increased in this topology. Simulation in Pspice confirmed this prediction.

These findings provide guidance into how to design a highly sensitive charge measurement system for ME laminate sensors.

# CHAPTER 6

## ME UNIT SIMULATION

### 6.1 Introduction

Prediction of the performance of ME units is important, this is because we need to know the output signal in response to a specific one, and at the same time to know the intrinsic noise level. I need to ask myself “did the ME unit that I constructed reach its lowest detectable signal?” To answer this question, one can use a mathematic method to calculate the results from the ME and circuit models, however, this calculation is quite cumbersome and will take too much time; also the result is not intuitive.<sup>88</sup> Alternatively, Pspice is a very useful tool for electronic system simulations, not only in time domain, but also in the frequency one. In this section, I will present the following questions addressed by using this Pspice simulation tool:

- 1) How will the ME sensors perform to different input signals? To simulate the output result, a Pspice model for the ME sensor in the time domain needs to be set up. This was done and experimental results obtained to verify the simulation.
- 2) Did the ME unit that I constructed reach its theoretical detection limit? Each detection unit has an intrinsic noise level. This noise level determines the lowest detectable signal. To obtain the noise level, I experimentally acquired a noise spectrum for a ME sensor and created a spice noise model. Then I used this model to predict the output noise level in Pspice. If the output noise level of my prototype ME unit can achieve the predicted result, then I can say with some

confidence that the ME unit I constructed had reach its measurement limit.

## 6.2 ME sensor Simulation in Time domain

To simulate the ME sensor in the time domain with the tool “Pspice”, I need to develop a time domain ME sensor model. This model can be obtained from that introduced in Fig.3-2 of this thesis. The current source  $I(s)$  in Fig.3-2 can be then converted to a time domain one  $I(t)$  by an inverse Laplace transformation, as follows:

$$I(t) = L^{-1}(j\omega \cdot \alpha' \cdot H(j\omega)) = \frac{d}{dt}(\alpha' \cdot H(t)); \quad (6.1)$$

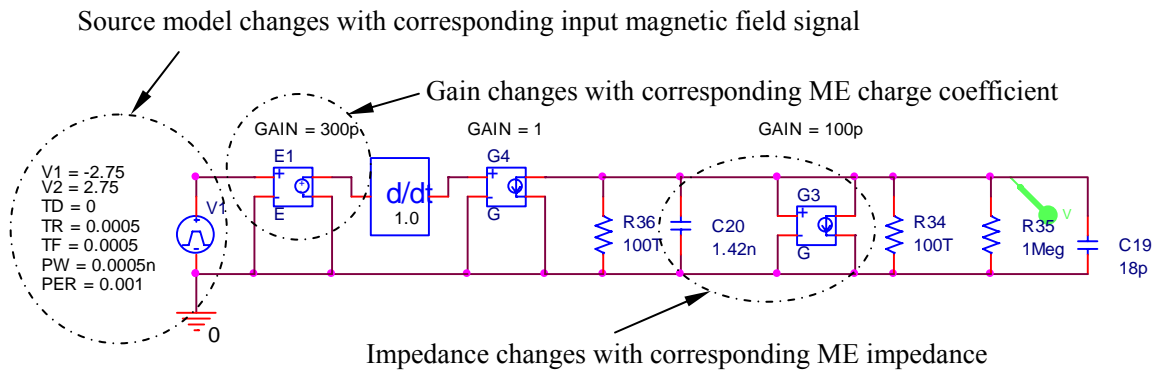
where  $t$  is the time in seconds,  $L^{-1}()$  the inverse Laplace operation,  $\omega$  the angular frequency in rad/s, and  $H$  the magnetic field. It is assumed that  $H_{t=0}=0$ .

In the low frequency range (<1k Hz), one can assume that  $\alpha'$  is a constant and that eq. (6.1) can be simplified to:

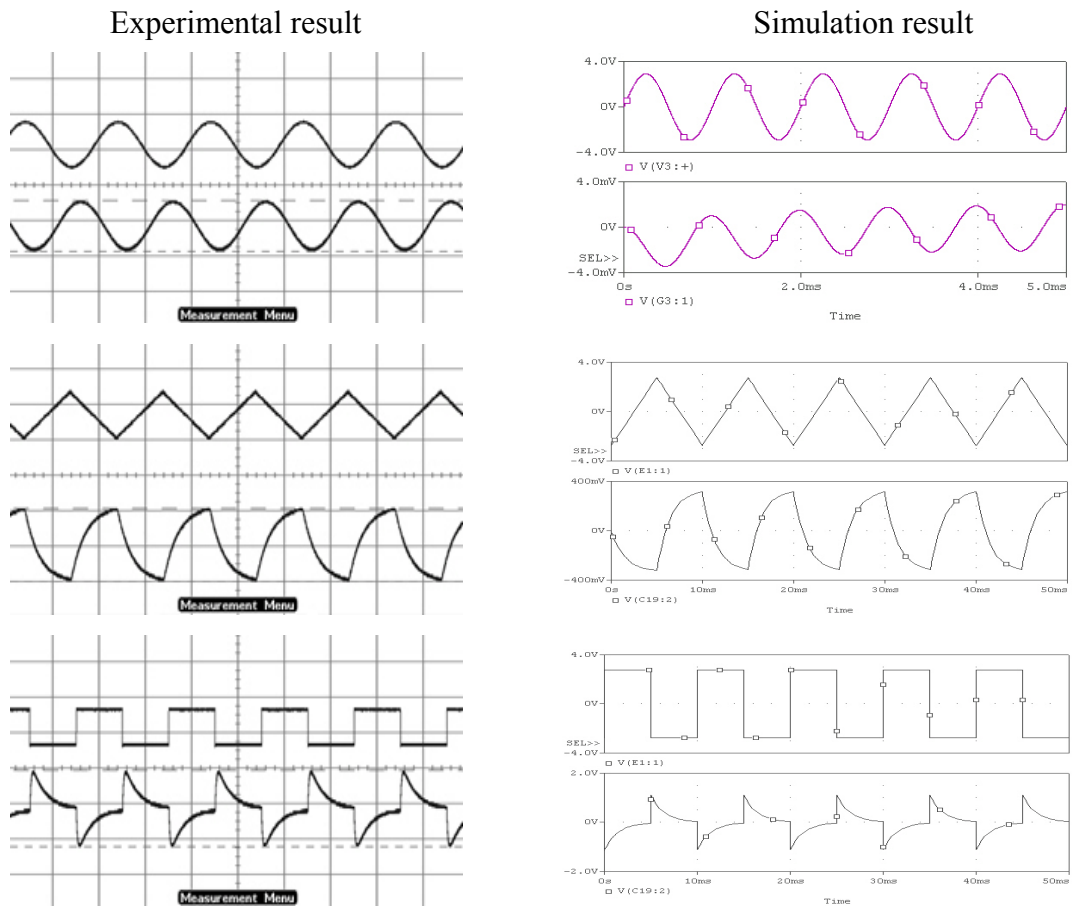
$$I(t) = \alpha' \cdot \frac{d}{dt}(H(t)); \quad (6.2)$$

This equation is quite a simple form that can be used as a ME current source in time domain. At low frequencies,  $R$  and  $C$  will be frequency independent. So, the values of  $R$  and  $C$  in the time domain will be the same as those in the frequency domain. One can then construct a ME laminate sensor time-domain model in Pspice from eq. (6.2), as illustrated in Fig.6-1(a).

To verify the Pspice model in Fig.6-1(a), experiments were performed with different input signals (sinodal, triangle and square wave) and the ME output voltages measured, see Fig.6-1(b). The simulation results from the model are also given in this figure. By comparing experimental result and prediction, we can see that the model of



(a)



(b)

**Fig.6-1.** (a) Pspice model in time domain for the ME laminate sensor; and (b) The comparison of experimental results and simulation results (Top of each figures: the input, bottom of each figures: the corresponding output).

Fig.6-1(a) can successfully predict the output signal from the input one.

### **6.3 ME Unit noise level simulation**

To acquire the ME unit output noise level, one needs to include all the noise sources within the devices (sensor, circuit) into Pspice. The circuit noise model was calculated by Pspice, so we only need to set up the noise model for the ME laminate sensor. To obtain the sensor's noise model, one needs to know the noise behavior, or more accurately, the noise spectrum of the ME laminate sensor. This requires experimental data.

A Longitudinal-Transverse (L-T) mode ME laminate sensor was used for the experiment. It was constructed from two pieces of Terfenol-D of size  $28 \times 6 \times 1.1 \text{mm}^3$  and one piece of PZT-5 of size  $30 \times 6 \times 0.5 \text{mm}^3$ . The sensor's output was connected to the input of a low noise current preamplifier (Keithley 428) with gains of  $10^{10} \text{V/A}$ . The output of the amplifier was then fed into a dynamic analyzer (SR785). The noise spectrum can then be read out from the analyzer. Care must be taken in construction and measurement: including excellent grounding and shielding techniques, low humidity, stable environment temperature, and vibration noise isolation.<sup>53, 89-91</sup>

Fig.6-2 illustrates the experimental noise spectrum. One can see that the white noise floor was about  $13 \text{fA}^2/\text{Hz}$  or  $3.6 \text{fA}/\sqrt{\text{Hz}}$ , and the  $1/f$  current noise corner frequency was about 5Hz. From these results, I can acquire the current noise spectrum of the ME sensor as follows:

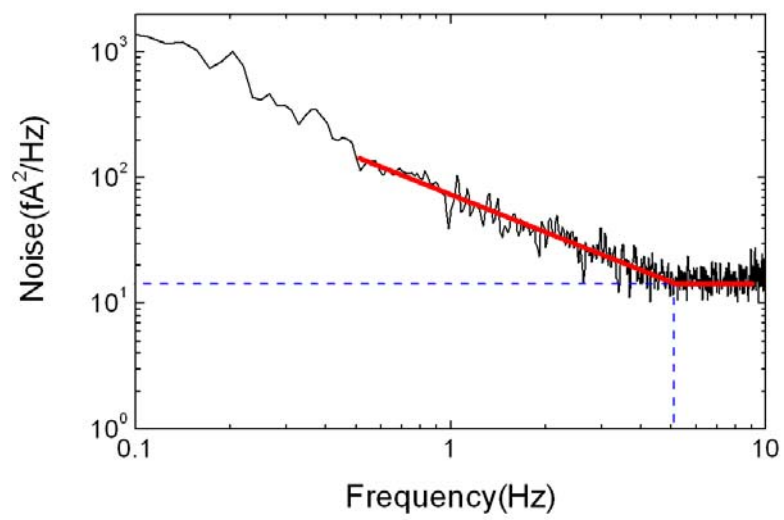


**Fig.6-2.** The noise spectrum of the ME laminate sensor.

$$i_c^2 = 1.3 \times 10^{-29} \left( \frac{5}{f} + 1 \right). \quad (6.3)$$

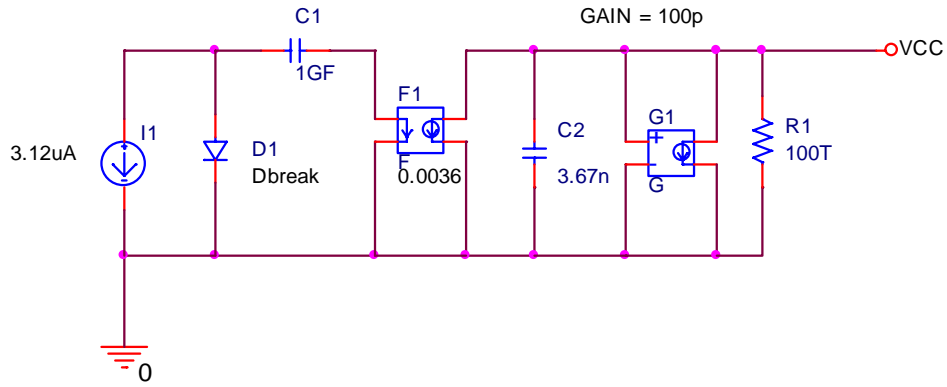
To set up a ME noise model in Pspice, we need to create a new model with regards to the spectra of Fig.6-2. If there is prior noise model with the same noise spectrum behavior, then we can make full use of it. Fortunately, there was such a prior device noise model \_ the diode. Pspice calculate the noise current of a diode as:<sup>49, 51</sup>

$$i_d^2 = \frac{KF \times I_D^{AF}}{f} + 2qI_D. \quad (6.4)$$

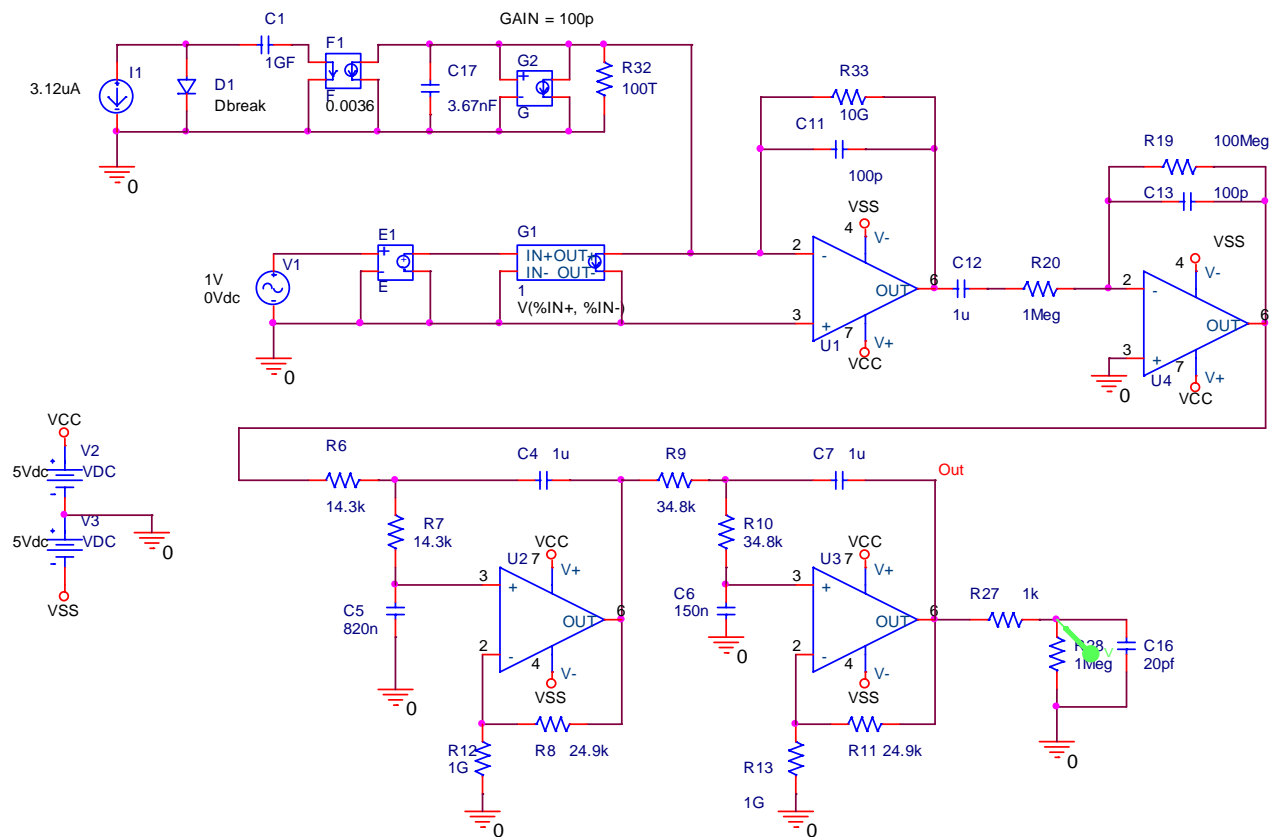
where KF is the flicker noise coefficient in amps, AF the flicker noise exponent,  $I_D$  the diode dc bias current,  $q$  the electron charge, and  $f$  the frequency in Hertz. AF and KF are the parameters that can be specified by users in Pspice. For simplification, I first created a noise current source with a noise floor of  $i_w=1\text{pA}/\text{sqrt}(\text{Hz})$  and corner frequency of  $f_c=5\text{Hz}$ , then I used a F-type (current-current) device to convert it to a current source with value of  $3.6\text{fA}/\text{sqrt}(\text{Hz})$ . To do this, I set  $AF=1$  and calculated KF as  $KF = 2qf_c = 2 \times 1.602 \times 10^{-19} \times 5 = 1.602 \times 10^{-18} \text{ A}$ . The dc bias current for the diode can be calculated as  $I_D=i_w^2/2q=3.12\text{uA}$ . However, these calculations only include the noise spectrum of the ME sensor: I still need to induce the ME impedance. The impedance is a simple R and C in parallel, as illustrated earlier in Fig.3-4. However, if we use the R model in Pspice, a Johnson noise will be induced. Accordingly, we need to construct the impedance without a noise contribution since we had the noise spectrum contribution included within the Diode model that was set up. Following this consideration, I chose a G-type (voltage to current) device in Pspice, and set the gain to  $1/R$ . This will bring a noiseless resistance. Using this approach, I can set the

ME noise model as illustrated in Fig.6-3(a), and the ME unit model as given in Fig.6-3(b).

The output noise level simulation result is given in Fig.6-4(a). As we can see, the predicted noise level from Pspice is about 5.06mV: this is a RMS value. For comparison, I then constructed a prototype ME unit as shown in Fig.6-4(b), and measured the output noise level using an oscilloscope as shown in Fig.6-4(c). The prototype ME unit had an output noise level of about 20mV (peak-peak). To relate the RMS and Peak-Peak value of the noise, a crest factor (CF) was used. For Gaussian noise, if we choose CF=2, then the probability of the peak-peak noise exceeding  $CF \times$  RMS is about 32%. If CF=3, then this probability drops to 13%; and for CF=4, it becomes 4.6%: further more, for CF = 5, 6, 7, 8, the probabilities are 1.2%, 0.27%, 0.046% and 0.0063% respectively.<sup>92</sup> My measurement results revealed for  $CF \approx 4$  that the output noise level of the prototype ME unit had essentially reached the predicted limit.

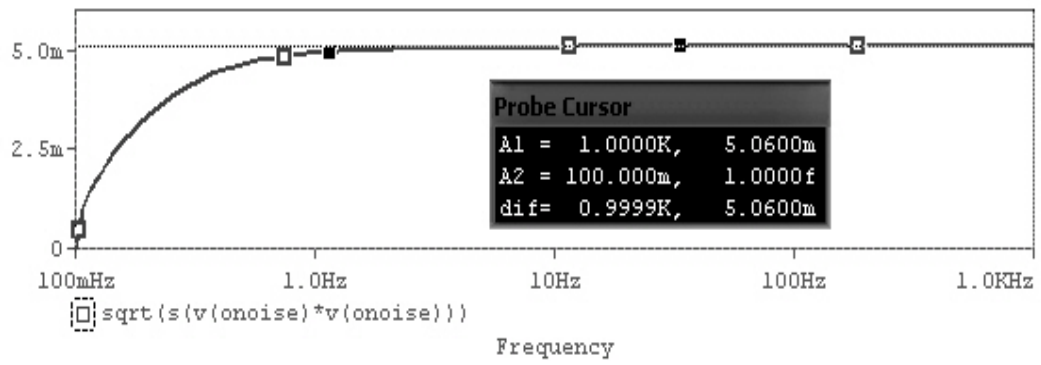


(a)

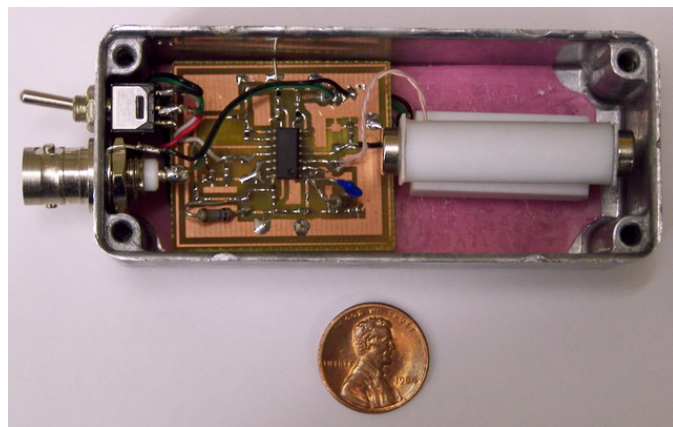


(b)

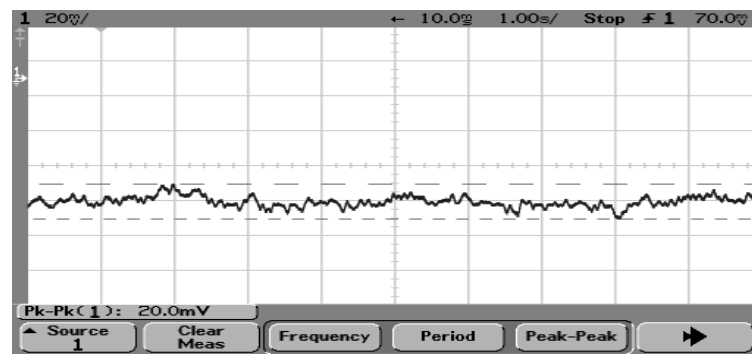
**Fig.6-3.** Noise model of (a) the ME laminate sensor; and (b) ME unit.



(a)



(b)



(c)

**Fig.6-4.** (a) Output noise simulation result of the ME Unit; (b) prototype of the ME unit; and (c) practical output noise measurement result of the ME prototype unit.

# **CHAPTER 7**

## **GIANT MAGNETOELECTRIC MECHANISM IN MAGNET/PIEZOELECTRIC DEVICE**

### **7.1 Introduction**

Previous research has shown that the giant ME effect can only appear in the composites by magnetostrictive and piezoelectric layers laminated together. Terfenol-D and Metglass are the most widely used materials for the magnetostrictive phase, due to their giant magnetostrictive properties. However, the rare earth alloy Terfenol-D, is too expensive for large scale applications; Metglass, although cheap, is too thin to drive thick piezoelectric layers.

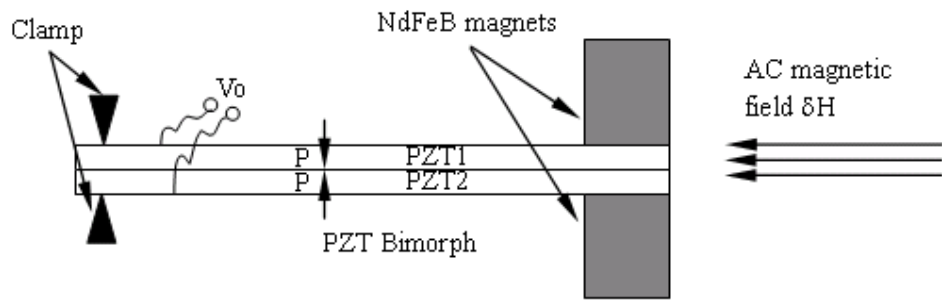
Developing new cheap materials with giant magnetostrictive properties is a good idea; however, it will be a long-term project. A logical, but time-save method, is to turn to considering of a new magnetoelectric mechanism. Here, I ask a question: will that be possible to develop a new giant magnetoelectric mechanism without using magnetostrictive materials? The answer is “yes”. In this chapter, I will introduce such a new giant ME mechanism. This new ME mechanism comes from the complex coupling resulted from magneto-magnetic, magneto-mechanical and electro-mechanical coupling. The ME Device constructed using this new mechanism does in fact exhibit a giant ME effect. Further more, the materials used to construct the device were quite cheap. This new ME device is also passive.

## 7.2 Working principle and Experiment

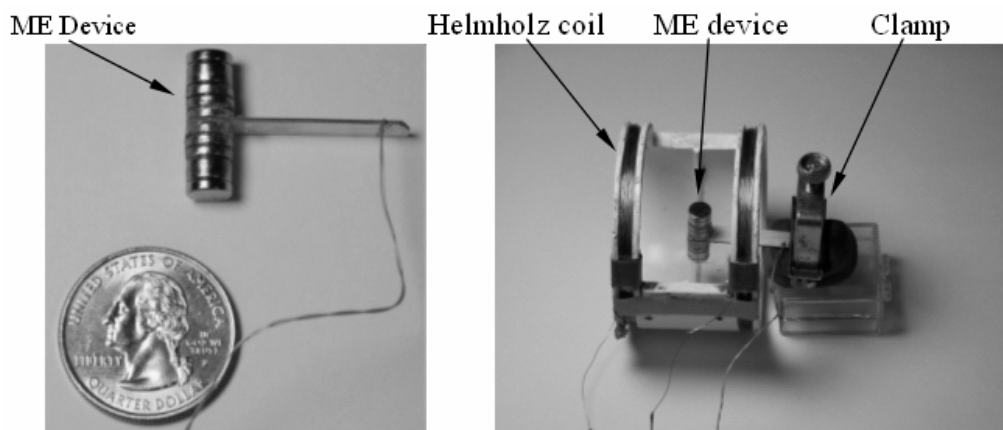
In this section, I will show that an apparent ME effect can be simply realized by attaching permanent magnets to a piezoelectric cantilever. In this case, magnetostrictive layers are not required to achieve giant ME coefficients. When an external ac magnetic field is applied to this device, it interacts with the static magnetic field provided by the permanent magnets. This interaction induces a magnetic force which is passed through the magnets to the piezoelectric cantilever; and the electro-mechanical coupling in the piezoelectric cantilever then induces a charge output. This ME effect is a complex interaction that results from magneto-magnetic, magneto-mechanical, and electro-mechanical couplings. Furthermore, the attached magnets also serve as a tip mass loading which further reduce the first bending resonant frequency, offering the potential of resonance-enhanced ME coefficients at extremely-low frequencies.<sup>93, 94</sup>

In Fig.7-1, I show (a) the structure of the PZT bimorph with attached NdFeB magnets, and (b) a photo of a prototype bimorph which when clamped at one end acts like a cantilever if acted upon by an external magnetic field. The PZT bimorph was constructed using two pieces of PZT-850 (each 28x6x0.3mm<sup>3</sup> in size), whose layers were poled in opposite thickness directions. The size of the NdFeB magnets was  $\Phi 6.35 \times 9.5$ mm, which were attached to the PZT bimorph by use of a high strength epoxy. For a clamped-free mode bar (i.e., a vibrating cantilever), the bending resonance frequency ( $f_n$ ) is given as<sup>42, 73</sup>

$$f_n = \frac{\pi \cdot d}{4\sqrt{3} \cdot l^2} \sqrt{\frac{1}{\rho \cdot s_{22}}} \beta_n^2; \quad (7.1)$$



(a)



(b)

**Fig.7-1.** (a) Structure of NdFeb/PZT-Bimorph/NdFeb; (b) photo of prototype device and testing.

where  $d$  is the thickness of the laminate,  $l$  its length,  $\bar{\rho}$  its average density, and  $\bar{s}_{22}$  its equivalent elastic compliance; and where  $\beta_1=0.597$ ,  $\beta_2=1.494$ , and  $\beta_n \approx (n-0.5)$  for  $n > 2$ , where  $n$  is the order of the bending mode. The first order bending mode resonance frequency can be estimated by (7.1) to be about 180Hz for the PZT-bimorph cantilever: where  $\rho=7.7\text{g/cm}^3$  and  $s=1.6 \times 10^{-11}\text{m}^2/\text{N}$  for PZT-850. Attached NdFeB magnets will then act as a tip mass loading, further lowering its resonance frequency.

An external magnetic field applied along the length of the bimorph will couple to the permanent magnets attached on the free end. This will then exert a magneto-elastic force on the PZT bimorph, inducing a bending moment as illustrated in Fig.7-2. Please note that there is a neutral surface between the PZT layers of the bimorph, where the stress statuses are opposite to each other: in this case, the induced charges across the PZT layers will also be opposite. In my experiments, the magnets attached to the bimorph cantilever were excited using a Helmholtz coil, and  $\alpha_{\text{ME}}$  was measured using a lock-in amplifier (SR850).

In Fig.7-3, I show the ME coefficient as a function of frequency for  $1 < f < 500\text{Hz}$ , performed using the prototype shown in Fig. 1(b). In this figure, it can be see that ME voltage coefficients as a high as  $\alpha_{\text{ME}}=16\text{V/cm-Oe}$  can be obtained at subresonant frequencies of  $f \leq 10\text{Hz}$ . Under EMR conditions, the ME voltage coefficient was enhanced to  $\sim 250\text{V/cm-Oe}$  at a first order bending mode frequency of  $\sim 60\text{Hz}$ . The corresponding ME charge coefficients were  $62\text{nC/cm-Oe}$  at  $10\text{Hz}$ , and  $960\text{nC/cm-Oe}$  at the 1<sup>st</sup> bending mode. These values are quite large approaching the highest value ever reported for a ME laminate: which was  $\alpha_{\text{ME}}=20\text{V/cm-Oe}$  for Metglas/PZT composites. The large values for the PZT-bimorph are due to the strength of the NdFeB permanent magnets placed on the free

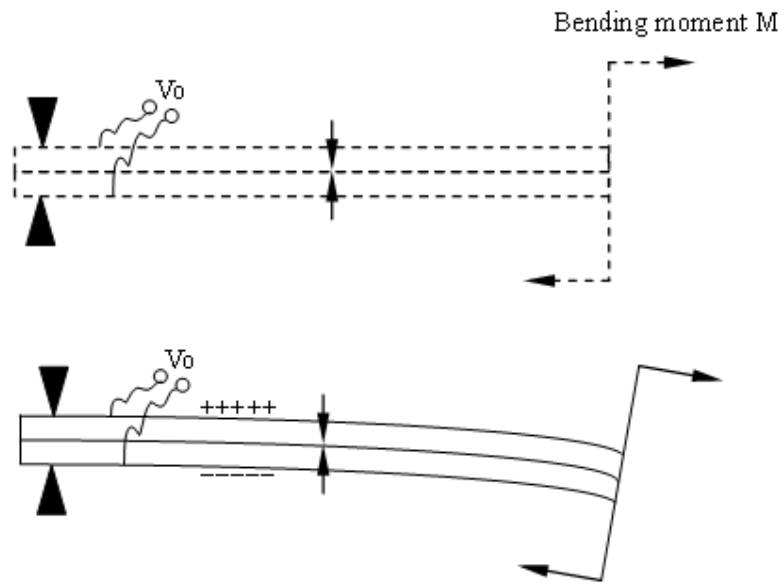


**Fig.7-2.** Illustration of the working principle.

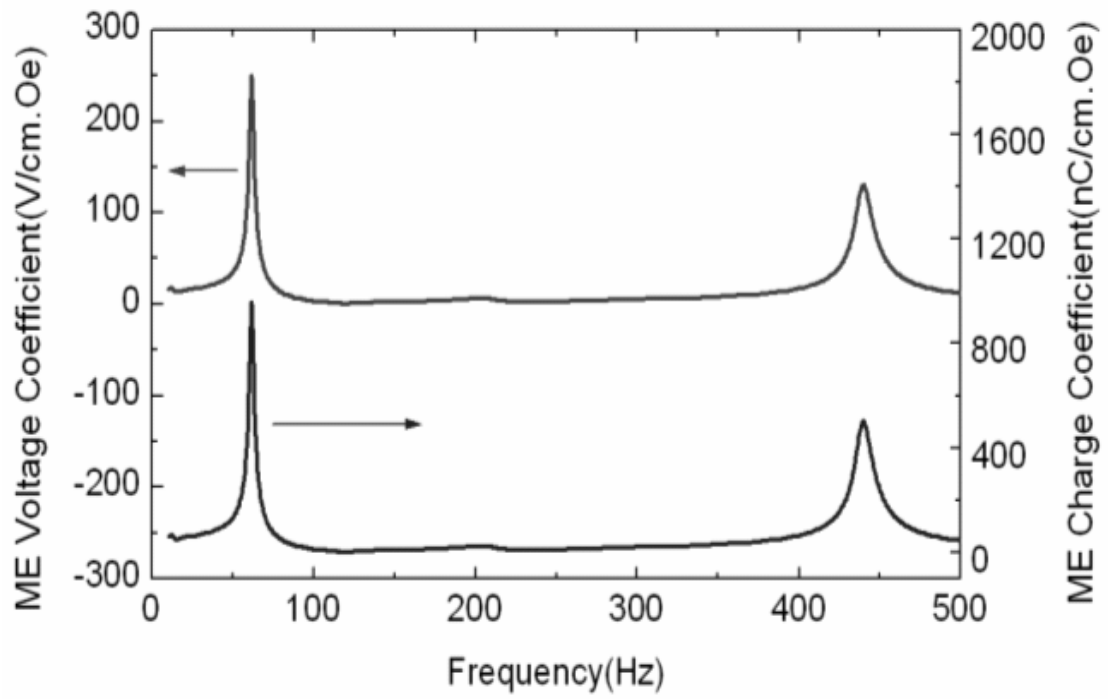


**Fig.7-3.** Frequency dependence of the ME voltage coefficient and charge coefficient.

end of the cantilever, which when acted upon by external magnetic fields will induce large mechanical forces. It must be noted that these large effects are not uniform along the length of the PZT-bimorph, but rather limited to the region closest to the clamped end of the cantilever.<sup>95</sup>

My findings show several simple insights into magnetoelectric effects in layered composites. First, magnetostrictive layers are not necessarily required to achieve giant ME coefficients. Rather, a simple vibrating piezoelectric cantilever with attached permanent magnets on the free end will induce large voltages (and charges) in response to external magnetic fields. Second, the resonance-enhancement of the ME effect can be dramatically shifted to lower frequencies by use of a clamped-free bending mode, which can be even further reduced by a tip mass loading method. This makes feasible dramatic enhancements of ME effects (over narrow bandwidths) at extremely low frequencies.

### **7.3 Summary**

I have found large apparent ME effects in simple PZT-bimorphs with attached NdFeB magnets. A tip mass loading method was used to further reduce the frequency of a resonant bending mode. My results show giant ME effects of  $\sim 16\text{V/cm-Oe}$  or  $62\text{nC/cm-Oe}$  at low subresonant frequencies ( $\sim 10\text{Hz}$ ), and  $\sim 250\text{V/cm-Oe}$  or  $960\text{nC/cm-Oe}$  at the 1<sup>st</sup> bending mode frequency ( $\sim 60\text{Hz}$ ).

*Parts of these chapter are reprinted from the reference<sup>96</sup>*

## Reference

1. M. Fiebig, *J. Phys. D-Appl. Phys.*, 38, R123 (2005).
2. M. I. Bichurin, V. M. Petrov and G. Srinivasan, *Phys. Rev. B*, 68, 054402 (2003).
3. P. Curie, *J. Physique*, 3, 393 (1894).
4. L. D. Landau and E. M. Lifshitz, *Electrodynamics of Continuous Media*, (Oxford, Pergamon, 1960).
5. I. E. Dzyaloshinskii, *Sov. Phys.*, 10, 628 (1959).
6. D. N. Astrov, *Sov. Phys.*, 11, 708 (1960).
7. D. N. Astrov, *Sov. Phys.*, 13, 729 (1961).
8. B. I. Al'Shin and D. N. Astrov, *Sov. Phys.*, 17, 809 (1963).
9. G. T. Rado, *Phys. Rev. Lett.*, 13, 335 (1964).
10. E. Ascher, H. Rieder, H. Schmid and H. Stossel, *J. Appl. Phys.*, 37, 1404 (1966).
11. R. P. Santoro, D. J. Segal and R. E. Newnham, *J. Phys.Chem. Solids*, 27, 1192 (1966).
12. T. Watanabe and K. Kohn, *Phys. Trans.*, 15, 57 (1989).
13. T. H. O'Dell, *Phil. Mag.*, 16, 487 (1967).
14. B. B. Krichevstov, V. V. Pavlov, R. V. Pisarev and A. G. Selitsky, *Ferroelectrics*, 161, 65 (1993).
15. G. A. Gehring, *Ferroelectrics*, 161, 275 (1994).
16. J. Wang, J. B. Neaton, H. Zheng, V. Nagarajan, S. B. Ogale, B. Liu, D. Viehland, V. Vaithyanathan, D. G. Schlom, U. V. Waghmare, N. A. Spaldin, K. M. Rabe, M.

- Wuttig and R. Ramesh, *Science*, 299, 1719 (2003).
17. H. Zheng, J. Wang, S. E. Lofland, Z. Ma, L. Mohaddes-Ardabili, T. Zhao, L. Salamanca-Riba, S. R. Shinde, S. B. Ogale, F. Bai, D. Viehland, Y. Jia, D. G. Schlom, M. Wuttig, A. Roytburd and R. Ramesh, *Science*, 303, 661 (2004).
  18. J. V. D. Boomgaard, D. R. Terrell, R. A. J. Born and H. F. J. I. Giller, *J. Mater. Sci.*, 9, 1705 (1974).
  19. Zhan Shi, C.-W. Nan, J.M. Liu, D. A. Filippov and M. I. Bichurin, *Phys. Rev. B*, 70, 134417 (2004).
  20. J. V. D. Boomgaard and R. A. J. Born, *J. Mater. Sci.*, 13, 1538 (1978).
  21. G. Srinivasan, E. T. Rasmussen, A. A. Bush, K. E. Kamentsev, V. F. Meshcheryakov and Y. K. Fetisov, *Appl. Phys. A-Mater. Sci. Process.*, 78, 721 (2004).
  22. N. Nersessian, S. W. Or and G. P. Carman, 9th Joint Magnetism and Magnetic Materials Conference/ International Magnetism Conference, 2646 (2004).
  23. K. K. Patankar, R. P. Nipankar, V. L. Mathe, R. P. Mahajan and S. A. Patil, *Ceram. Int.*, 27, 853 (2001).
  24. S. V. Suryanarayana, *Bull. Mater. Sci.*, 17, 1259 (1994).
  25. J. Ryu, A. V. Carazo, K. Uchino and H. E. Kim, *J. Electroceram.*, 7, 17 (2001).
  26. C. W. Nan, L. Liu, N. Cai, J. Zhai, Y. Ye, Y. H. Lin, L. J. Dong and C. X. Xiong, *Appl. Phys. Lett.*, 81, 3831 (2002).
  27. J. Ryu, A. V. Carazo, K. Uchino and H. E. Kim, *Jpn. J. Appl. Phys. Part 1 - Regul. Pap. Short Notes Rev. Pap.*, 40, 4948 (2001).
  28. G. Srinivasan, R. Hayes, C. P. DeVreugd, V. M. Laletsin and N. Paddubnaya,

- Appl. Phys. A-Mater. Sci. Process., 80, 891 (2005).
29. S. X. Dong, J. F. Li and D. Viehland, Appl. Phys. Lett., 83, 2265 (2003).
  30. U. Laetsin, N. Padubnaya, G. Srinivasan and C. P. Devreugd, Appl. Phys. A-Mater. Sci. Process., 78, 33 (2004).
  31. G. Harshe, J. P. Dougherty and R. E. Newnham, Mathematics in Smart Structures, 1919, 224 (1993).
  32. G. Srinivasan, E. T. Rasmussen, J. Gallegos, R. Srinivasan, Y. I. Bokhan and V. M. Laletin, Phys. Rev. B, 64, 214408 (2001).
  33. S. X. Dong, J. F. Li and D. Viehland, IEEE Trans. Ultrason. Ferroelectr. Freq. Control, 51, 793 (2004).
  34. S. X. Dong, J. Y. Zhai, N. G. Wang, F. M. Bai, J. F. Li, D. Viehland and T. A. Lograsso, Appl. Phys. Lett., 87, 3 (2005).
  35. J. Y. Zhai, S. X. Dong, Z. P. Xing, J. F. Li and D. Viehland, Appl. Phys. Lett., 89, 083507 (2006).
  36. S. X. Dong, J. Y. Zhai, J. F. Li and D. Viehland, Appl. Phys. Lett., 89, 252904 (2006).
  37. S. X. Dong, J. F. Li and D. Viehland, IEEE Trans. Ultrason. Ferroelectr. Freq. Control, 50, 1253 (2003).
  38. N. Cai, J. Zhai, C. W. Nan, Y. Lin and Z. Shi, Phys. Rev. B, 68, 224103 (2003).
  39. E. Quandt, S. Stein and M. Wuttig, International Magnetism Conference 2005, 3667 (2005).
  40. S. X. Dong, J. Y. Zhai, F. M. Bai, J. F. Li, D. Viehland and T. A. Lograsso, J.

- Appl. Phys., 97, 103902 (2005).
41. S. Dong, J. Zhai, F. Bai, J. F. Li and D. Viehland, Appl. Phys. Lett., 87, 062502 (2005).
  42. J. G. Wan, Z. Y. Li, Y. Wang, M. Zeng, G. H. Wang and J. M. Liu, Appl. Phys. Lett., 86, 202504 (2005).
  43. J. Y. Zhai, Z. P. Xing, S. X. Dong, J. F. Li and D. Viehland, Appl. Phys. Lett., 88, 3 (2006).
  44. S. X. Dong, J. F. Li and D. Viehland, Appl. Phys. Lett., 85, 2307 (2004).
  45. J. Vrba and S. E. Robinson, Methods, 25, 249 (2001).
  46. J. E. Lenz, Proc. IEEE, 78, 973 (1990).
  47. J. Lenz and A. S. Edelstein, IEEE Sens. J., 6, 631 (2006).
  48. P. Ripka, *Magnetic Sensors and Magnetometers*, (Artech House, Norwood, 2001).
  49. S. Franco, *Design with Operational Amplifiers and Analog Integrated Circuits*, (Tata McGraw-Hill, New Delhi, 2002).
  50. W. O. Henry, *Noise reduction Techniques in Electronic Systems*, (John Wiley & Sons, New York, 1988).
  51. C. D. Motchenbacher and J. A. Connelly, *Low Noise Electronic System Design*, (John Wiley & Sons, New York, 1993).
  52. M. I. Montrose, *Emc and the Printed Circuit Board: Design, Theory, and Layout Made Simple*, (Wiley-IEEE Press, New York, 1998).
  53. Keithley, *Low Level Measurement Handbook\_Precision DC current, Voltage*,

- and Resistance Measurements (6th Edition)*, (Keithley, Cleveland, 2004).
54. R. W. Whatmore, Rep. Prog. Phys., 49, 1335 (1986).
  55. W. Kester, *Practical Design Techniques for Sensor Signal Conditioning*, (Analog Devices, 1999).
  56. W. M. Leach, Proc. IEEE, 82, 1515 (1994).
  57. A. Ryan and T. Scranton, Analog Dialogue, 18, 151 (1984).
  58. M. S. Keshner, Proc. IEEE, 70, 212 (1982).
  59. P. R. Gray, P. J. Hurst, S. H. Lewis and R. G. Meyer, *Analysis and Design of Analog Integrated Circuits (4th Edition)*, (John Willey & Sons, New York, 2001).
  60. A. V. D. Ziel, Proc. IEEE, 58, 1178 (1970).
  61. J. B. Johnson, IEEE Spectr., 8, 42 (1971).
  62. D. Abbott, B. R. Davis, N. J. Phillips and K. Eshraghian, IEEE Trans. Educ., 39, 1 (1996).
  63. R. Mancini, *OP Amps For Everyone: Design Reference*, (Texas Instruments, Dallas, 2002).
  64. Z. P. Xing, J. F. Li and D. Viehland, Appl. Phys. Lett., 91, 3 (2007).
  65. D. R. Tilley and J. F. Scott, Phys. Rev. B, 25, 3251 (1982).
  66. M. I. Bichurin, D. A. Filippov, V. M. Petrov, V. M. Laletsin, N. Paddubnaya and G. Srinivasan, Phys. Rev. B, 68, 132408 (2003).
  67. N. Cai, C. W. Nan, J. Y. Zhai and Y. H. Lin, Appl. Phys. Lett., 84, 3516 (2004).
  68. E. H. Putley, *Semiconductors and Semimetals\_Infrared detectors*, (Academic press, New York, 1970).

69. S. G. Porter, *Ferroelectrics*, 33, 193 (1981).
70. A. Hossain and M. H. Rashid, *IEEE Trans. Ind. Appl.*, 27, 824 (1991).
71. S. E. Stokowski, *Appl. Phys. Lett.*, 29, 393 (1976).
72. J. Y. Zhai, Z. P. Xing, S. X. Dong, J. F. Li and D. Viehland, *Appl. Phys. Lett.*, 93, 072906 (2008).
73. F. Wang, Z. T. Jiang and R. D. Shi, *Piezoelectric Vibration (In Chinese)*, (Science, China, 1989).
74. S. X. Dong, J. F. Li and D. Viehland, *Journal of Materials Science*, 41, 97 (2006).
75. Z. P. Xing, J. F. Li and D. Viehland, *Appl. Phys. Lett.*, 91, 182902 (2007).
76. J. Z. Z.P. Xing, J. Gao, J. Li, and D. Viehland, *IEEE Electron Device Lett.*, (2009, Accepted).
77. C. Delaney, *Electronics for the Physics*, (Harmondsworth, Penguin, 1969).
78. V. I. Dukhanov, I. B. Mazurov, A. A. Mitin and A. A. Chesalov, *Instrum. Exp. Tech.*, 20, 1065 (1977).
79. G. Grainger and D. K. Bedford, *Electron. Lett.*, 14, 126 (1978).
80. P. Coops, C. W. E. Vaneijk and R. W. Hollander, *Nucl. Instrum. Methods Phys. Res. Sect. A-Accel. Spectrom. Dect. Assoc. Equip.*, 227, 283 (1984).
81. C. Bacci, S. Centro, M. Degiorgi and R. Martinelli, *Nucl. Instrum. Methods Phys. Res. Sect. A-Accel. Spectrom. Dect. Assoc. Equip.*, 273, 321 (1988).
82. M. R. Wolffenbuttel, R. F. Wolffenbuttel and P. P. L. Regtien, 5th Anniversary Meeting of Eurosensors, 101 (1991).

83. M. Saukoski, L. Aaltonen, K. Halonen, T. Salo and Ieee, IEEE International Symposium on Circuits and Systems (ISCAS), 5377 (2005).
84. G. Bertuccio and A. Pullia, 1994 Nuclear Science Symposium and Medical Imaging Conference (NSS/MIC), 740 (1994).
85. L. T. Wurtz and W. P. Wheless, IEEE Trans. Instrum. Meas., 42, 942 (1993).
86. A. Pullia, R. Bassini, C. Boiano and S. Brambilla, Annual Nuclear Science Symposium (NSS), 530 (2000).
87. P. Grybos, M. Idzik and A. Skoczen, International Conference on Mixed Design of Integrated Circuits and Systems (MIXDES 2005), 107 (2005).
88. Z. P. Xing, J. Y. Zhai, S. X. Dong, J. F. Li, D. Viehland and W. G. Odendaal, Measurement Science & Technology, 19, 9 (2008).
89. M. Sampietro, G. Accomando, L. G. Fasoli, G. Ferrari and E. C. Gatti, IEEE Trans. Instrum. Meas., 49, 820 (2000).
90. G. Ferrari and M. Sampietro, Rev. Sci. Instrum., 73, 2717 (2002).
91. H. Y. Jiang, W. R. Chen and H. Liu, IEEE Trans. Biomed. Eng., 49, 1270 (2002).
92. L. Smith and D. H. Sheingold, Noise and Operational Amplifier Circuits, Analog Devices, (1969).
93. M. Gurgoze, J. Sound Vibr., 190, 149 (1996).
94. M. Gurgoze, J. Sound Vibr., 105, 443 (1986).
95. J. M. Whitney, Compos. Sci. Technol., 23, 201 (1985).
96. Z. P. Xing, J. F. Li and D. Viehland, Appl. Phys. Lett., 93, 013505 (2008).